ATOMISTIC SIMULATIONS OF GE ON AMORPHOUS SILICA SUBSTRATES

Claire Yungchi Chuang

A DISSERTATION

in

Chemical and Biomolecular Engineering

Presented to the Faculties of the University of Pennsylvania

in

Partial Fulfillment of the Requirements for the

Degree of Doctor of Philosophy

2015

Supervisor of Dissertation

_____

Talid Sinno, Professor of Chemical and Biomolecular Engineering

Graduate Group Chairperson

_____

Raymond Gorte, Professor of Chemical and Biomolecular Engineering

Dissertation Committee:
Dr. Robert Riggleman, Assistant Professor of Chemical and Biomolecular Engineering
Dr. Kathleen J. Stebe, Professor of Chemical and Biomolecualr Engineering
Dr. Vaclav Vitek, Professor of Materials Science and Engineering

ABSTRACT

ATOMISTIC SIMULATIONS OF GE ON AMORPHOUS SILICA SUBSTRATES

Claire Y. Chuang

Prof. Talid Sinno

High-quality Ge substrates have numerous applications, including high-efficiency III-V multijunction solar cells and photodetectors. But the high cost of single-crystalline Ge makes the use of Ge-on-Si virtual substrates more practical for device fabrication. However, the lattice mismatch between Ge and Si leads to a highly strained Ge layer when grown directly on the Si lattice. The high mismatch strain unavoidably leads to defects, primarily dislocations, that degrade the Ge film quality. Several approaches for mitigating these defects have been proposed, including selective epitaxial growth (SEG), in which one employs an amorphous layer (most often SiO_2) as a mask to reduce the epitaxial contact between the Ge and Si lattices to lower the mismatch strain. SEG has been demonstrated to successfully produce high-quality Ge films on Si, although defects are not fully eliminated. Further improvements will require quantitative understanding of the underlying atomic-scale mechanisms.

In this work, we present a computational framework to atomistically model the components of the SEG system ($Si/SiO_2/Ge$). The model is validated by comparing predictions to experimental observations and *ab initio* calculations of various properties related to crystalline Si and Ge and amorphous SiO_2, as well as combinations of these materials. The framework is then applied to study in detail the deposition of Ge on amorphous SiO_2. It is shown that the simulations are able to access experimentally meaningful deposition conditions and reproduce several quantities related to the island size distribution. We then extend our simulation framework for deposition to include

coarse projective integration (CPI). CPI is a multiscale modeling technique well-suited for situations, like atomic deposition, in which a system exhibits fast, stochastic processes, superposed onto slowly-evolving dynamics. In particular, we demonstrate an approach for generating atomistic configurations from limited knowledge of an island size distribution, which represents one of the key challenges in applying CPI to atomistic deposition. The results generated here should be easily adaptable to other deposition systems.

TABLE OF CONTENTS

LIST OF TABLES

LIST OF FIGURES

Chapter 1. Introduction

1.1 Motivation and Thesis Overview

High-quality Ge films on Si substrates have many potential applications, including III-V multijunction solar cells [1-5] and photodetectors [6, 7], but the 4.2% lattice mismatch between Ge and Si leads to the formation of threading dislocations when the Ge film is directly grown on the Si wafers. Selective epitaxial growth (SEG) [8-13] is a technique that uses an amorphous layer (most often SiO_2) in between the Ge and Si layers to relieve the lattice mismatch strain in the Ge film. In SEG, the Si substrate is covered by a thin layer of amorphous SiO_2 (a-SiO_2) with nanoscale windows prior to Ge deposition. During deposition, the Si lattice exposed by the windows serves as seeding sites for the growth of Ge islands. The Ge islands grow and coalesce upon continued epitaxial deposition, forming a Ge film layer on top of the SiO_2-covered Si. The localized, nanoscale contact area between the Ge film and the underlying Si substrate greatly reduces the total mismatch. SEG has been shown to successfully produce Ge films with low dislocation density ($<10^6$ cm^{-2}) [13], but further improvements require better understanding of the formation of defects, namely stacking faults and dislocations.

This thesis focuses on the development of a computational framework to describe the SEG system that involves crystalline Si and Ge as well as a-SiO_2. The computational model is based on the Tersoff empirical interatomic potential for Si-Ge [14] and a recent parameterization for the Si-O systems [15], with a single fitting parameter to describe the Ge-O interaction strength. Using atomistic molecular dynamics (MD) simulations, the model is shown to reproduce a wide range of structural and energetic properties relevant to the SEG system, including structures of bulk a-SiO_2, interface energies for Si-SiO_2 and

Ge-SiO_2. Moreover, the adsorption of Ge on a-SiO_2 is successfully captured in the current model using grand-canonical Monte Carlo simulations (GCMC). The fidelity of the model is further tested by applying it to processes occurring in SEG using MD, namely the random nucleation of Ge islands on the a-SiO_2 surface. The model predictions are in good agreement with the experimental results, confirming its validity for the SEG system of Ge films on SiO_2-covered Si substrates.

The agreement with experimental measurements in the MD simulation of Ge island nucleation on a-SiO_2 occurs when the deposition rate is slow relative to other processes responsible for island rearrangement and growth, even though the deposition fluxes are still orders of magnitude higher than in experiments. Further reduction in the deposition flux is desired, but the fluxes used in our study are already at the timescale limit of MD. The timescale limitation is a well-established problem in the simulation of deposition systems. Many studies combined computational models at different scales to examine the deposition systems at extended length and timescales [16-20]. Here, we focus on a multiscale simulation technique, known as coarse projective integration (CPI) [21-24], that exploits the timescale separation in complex systems.

Coarse projective integration is a type of the equation-free analysis. The fundamental idea of the equation-free analysis is that many systems that are governed by fast, stochastic microprocesses also exhibit a slowly-evolving manifold characterized by some coarse variables. In the case of deposition systems, the coarse variables may contain moments of the island size distribution or average surface height. The closed-form equations governing the evolution of these variables are not known, but their values at any time can be computed directly from the full microscopic system configuration. Based upon this idea, in CPI the temporal gradients of the coarse variables are computed

by conducting short MD simulations at any points of time. These numerically-estimated gradients are then used to evolve the differential equations in the coarse variables over time intervals that are large relative to the microprocesses, but small relative to the coarse variable timescale.

The primary challenge for applying CPI to deposition of Ge on a-SiO_2 substrates is the reconstruction of microscopic configurations from coarse variable descriptions. The a-SiO_2 surface presents a highly heterogeneous binding environment to Ge atoms and clusters. Placing islands at locations that are energetically unfavorable or constructing island morphologies that are unrealistic with respect to their locations will tend to produce instability of the reconstructed system and inability to maintain consistency with the slow manifold. We address this issue by designing a lifting procedure that correctly reproduces the evolution of the slow manifold. Our results allow for future application of CPI to the deposition and islanding of Ge on an a-SiO_2 surface.

Additional considerations are given to examining the aggregation of self-interstitials in bulk Si using a recent parameterization of the Tersoff potential model for Si [25]. The small interstitial clusters, with sizes less than 150 interstitial atoms, are important to controlling the Si wafer quality during crystallization and subsequent processing steps. While many theories and macroscopic processing models require their morphological and energetic properties as input, they are difficult to study experimentally due to their small size and transient nature. With the use of both direct and accelerated MD, we study the formation thermodynamics and morphology of these small interstitial clusters as a function of size and temperature based on the concept of inherent structure landscape.

A unifying theme across the different topics covered in the dissertation is the use of atomistic simulations with empirical interatomic potentials. In the next section, a brief introduction to atomistic simulations is discussed. An organization of the thesis is given at the end of the chapter.

1.2 Atomistic Simulations with Empirical Interatomic Potentials

The main goal of our work is to study defect formation processes during SEG using computer simulations. Over the years, computational models at different resolutions have been developed to describe phenomena at various time and length scales [26]. It is important to choose a computational model that best represents the processes of interest.

The computational models with the finest resolution are the *ab initio* methods, in which the interaction between nuclei is computed using quantum mechanical models. *Ab initio* methods are widely used in systems where explicit knowledge of the electronic structures is required, for example chemical reactions [2, 27]. Due to the extensive computational load, *ab initio* calculations are often limited to the scale of picoseconds with hundreds to thousands of atoms.

Atomistic simulations extend the size and timescales of the *ab initio* methods by coarse graining out the electronic details of the system. Instead, the interactions between atoms are computed using mathematical models that are designed to reproduce the force field of the respective system. The decrease in computational demand allows atomistic simulations to reach microseconds and billions of atoms [28]. Large-scale atomistic simulations allow one to make direct comparison with experimental observations, for example in the simulation of the deformation of nanopillars [29].

When the motion of individual atoms is not relevant, coarse grained models lump groups of atoms together into single units to reduce the degrees of freedom in the system while retaining selective microscopic details. The coarse grained models are at mesoscopic level on the order of micrometers and micro- to milliseconds [26]. Examples of coarse grained models include the simulation of polymers [30, 31] and biomolecules [32-34].

Models with the lowest resolution are the continuum models that are on macroscopic length and time scales. In these models, the system is not viewed as an ensemble of particles but rather continuous fields that are described by a system of mathematical equations, often ordinary or partial differential equations (ODEs or PDEs). Examples of such models include crystal growth in binary systems [35] and strain fields in Ge quantum dots on SiO_2-covered Si substrates [36].

In our work, we choose atomistic MD simulations with the use of a well-characterized empirical interatomic potential model as the means to probe the SEG system due to its ability to make direct connections to the experiments. Over the years, various empirical potential models have been proposed for Si and/or Ge that are fitted to a set of material properties, such as cohesive energies and lattice constants (hence the name "empirical"). Some popular examples of these empirical potential models include the Stillinger-Weber [37], the Environment-Dependent Interatomic Potential [38], the modified embedded atom method [39], and the Tersoff models [14, 40, 41]. In this work, we choose the Tersoff empirical potential model for the Si-Ge binary system [14] and combine it with the recent parameterization for SiO_2 [15] to describe the Ge-Si-O ternary SEG system with a single fitting parameter controlling the Ge-O interaction strength.

In general, it is not possible to capture quantitatively all properties of interest with empirical potentials. For example, while the point defect formation energies in crystalline Si are successfully reproduced by the Tersoff empirical potential [41], it over-predicts the melting temperature by 150% [39]. In the following chapters, we address this issue by carefully validating the empirical model for various properties and processes relevant to the Ge-on-Si SEG system to find the best overall description.

1.3 Thesis Outline

The structure of the thesis is organized as follows. In Chapter 2 we propose a Tersoff-based empirical potential model for the Ge-Si-O ternary system with a single fitting parameter controlling the Ge-O interaction strength. The fidelity of the model is studied in detail by comparing its predictions to experimental measurements or electronic structure calculations. The properties tested include the structure of bulk amorphous SiO_2, the Si/SiO_2 and Ge/SiO_2 interface energies, and Ge binding on a-SiO_2 surfaces. In Chapter 3 we applied to model to study dynamical processes that take place during SEG. In particular, we focus on the random nucleation of Ge islands on a-SiO_2 surfaces. By the application of atomic nucleation theory, we draw quantitative comparisons to prior experimental measurements and further validate the potential framework for the simulations of selective epitaxial growth of Ge films on Si substrates. In Chapter 4, we use our knowledge of the Ge-SiO_2 deposition system as our basis to develop coarse projective integration, a multiscale modeling technique, for deposition systems. A procedure for reconstructing microscopic configurations of Ge islands on a-SiO_2 surfaces is proposed and validated against results from direct simulations. In Chapter 5, we turn to study the small self-interstitial clusters in crystalline Si. The formation free energies

and entropies as functions of size and temperature are computed using the inherent structure landscape framework. Finally, conclusions and outlook of this work are presented in Chapter 6.

Chapter 2. Computational Framework for the Ge-Si-O Ternary Atomic System

2.1 Introduction

High-quality, single-crystal Ge substrates are useful for fabricating various advanced devices, including high-efficiency multijunction solar cells [1, 3, 4] and light emitters [42]. The need for Ge arises from its lattice size compatibility with various III-V materials (e.g. $GaInP_2$ and GaAs). However, the high cost of bulk single-crystal Ge has driven efforts to find a replacement, namely thin Ge films grown epitaxially on Si wafers. In addition to the greatly reduced cost relative to bulk Ge, such substrates also offer the possibility for monolithic integration of optoelectronics with traditional Si-based CMOS technology [43].

A key challenge for epitaxial deposition of Ge on Si is the 4.2% lattice mismatch, which leads to large stresses and concomitant defect formation, primarily in the form of threading dislocations (TD) that terminate at the Ge surface [11]. Many approaches for solving this issue have been proposed in the literature. Among the most intensively studied approaches is the graded SiGe layer technique [44], in which $Si_{1-x}Ge_x$ with gradually increasing Ge content is grown on a Si substrate in order to distribute the mismatch stress across a thicker film. This approach has been used to lower the TD density to ~10^6 cm^{-2}. Other well-researched approaches include cyclical thermal annealing [45] and liquid-phase epitaxy (LPE) [46, 47]. In the latter, melted Ge is encapsulated in a micro-crucible with insulator walls, and Ge contacts underlying Si within a limited seeding area of approximately 1000 μm^2 through a dielectric window [48, 49].

A particularly promising approach for reducing the impact of lattice mismatch in Ge-on-Si heteroepitaxy is selective epitaxial growth (SEG) [9, 11, 50], in which a templated interlayer is used to significantly reduce the contact area and strain energy density at the mismatched heterojunction and/or to trap defects from propagating by "necking" [9]. In a typical SEG process, a thin interlayer (most commonly SiO_2) that provides separation between Ge and Si is deposited on a Si substrate and subsequently perforated using one of several possible approaches [11, 50]. The Si exposed by the perforations serves as seeding sites (or pads) for the growth of Ge islands. These islands grow and coalesce upon continued epitaxial deposition, forming a high-quality Ge film. Improvement over conventional heteroepitaxy is obtained because the localized contact between Ge islands and underlying Si substrate greatly reduces the total mismatch. This reduction is especially significant when the total contact area between Ge and Si decreases to nanoscale dimensions because the strain density near the heterojunction decreases over a characteristic length comparable to the Ge-Si junction size [51]. On the other hand, island-island coalescence unavoidably leads to defects (stacking-faults and twins) via a process that remains incompletely understood, despite recent progress [13, 52].

The interaction between deposited Ge atoms and the interlayer is a critical factor in establishing the success of the SEG approach for growing high-quality Ge films. First, nonspecific Ge island nucleation on the interlayer must be avoided as these islands are not organized by the underlying silicon lattice. Second, as Ge islands grow out of seeding pads and onto the interlayer surface, the stress distribution within them is likely to be influenced by their interaction with the interlayer. The morphology, as well as the mobility, of the islands relative to the interlayer surface, depend strongly on the

Ge/interlayer interaction [53], which in turn may play a significant role in coalescence defect formation.

In recognition of the importance of the Ge-SiO_2 interaction in selective epitaxial growth and defect formation, the primary aim of this work is to validate an empirical potential model for the Ge-Si-O atomic system for use in molecular simulations. The use of empirical potentials permits the consideration of relatively large numbers of atoms thereby allowing more direct connections to experimental measurements [54-60]. On the other hand, the quality of the predictions is entirely dictated by the fidelity of the potential model, which must be verified carefully against more accurate interaction models that include explicit quantum mechanics. While empirical potentials have been tested extensively for single component materials, e.g., Si or Ge, the uncertainty associated with their use in a complex system such Ge-SiO_2 is much less well established. Here, we employ the Tersoff interaction potential [14] for Si and Ge and its recent extension to SiO_2 [61]. The Tersoff interaction model has been tested extensively in simulations of crystalline and liquid Si and Ge and is one of several popular potentials for these materials, along with the Stillinger-Weber [37], the Environment-Dependent Interatomic Potential [38], and the modified embedded atom method [39] potential models. Using several different experimental measurements, we study a single parameter to assess whether such a simple potential model can be employed in meaningful simulations of the Ge-SiO_2 system.

In the following section, the salient details of the Tersoff model are presented and the fitting parameter is identified. In Section 2.3, the interaction potential is applied to study several different Si–O systems including bulk a-SiO_2, a-SiO_2 surfaces, and the Si-SiO_2 interface. We focus on the interactions between Ge and a-SiO_2 in Section 2.4 to

parametrize the interaction potential for the SEG system. The properties analyzed include Ge-SiO_2 interfaces, as well as desorption and diffusion of Ge on a-SiO_2. We show that the resulting potential is able to describe well various properties that have been measured experimentally or computed using more accurate quantum mechanical simulations based on electronic density functional theory (DFT). Finally, in Section 2.5 we provide conclusions and outlook for further work.

2.2 A Tersoff-Based Interaction Model for the Ge-Si-O System

The Tersoff potential framework has been applied to pure Si [14, 40, 41] and Ge [14], Si-Ge [14] and Si-C [14] alloys, and recently to the Si-O mixture [61]. In the latter case, the resulting potential was applied to both crystalline and amorphous SiO_2 systems, and was shown to give reasonable descriptions of various SiO_2 structural and dynamical properties, including lattice parameters, bond energies and radial distribution functions.

Multiple parameterizations of the Tersoff model have been published, particularly for Si; the values used here are listed in Table 2.1. Within the Tersoff model, the overall system energy is described by a pair-wise summation over all atoms that are within a specified cut-off distance. However, the attractive term in the pair-wise interaction depends on the local environment, rendering the Tersoff potential a many-body function, i.e.,

$$E = \frac{1}{2}\sum_{i \neq j} f_c\left(r_{ij}\right)\left[\, f_R\left(r_{ij}\right) + b_{ij}\, f_A\left(r_{ij}\right)\right] \tag{2.1}$$

where $f_R\left(r_{ij}\right) = A_{ij}\exp\left(-\lambda_{ij} r_{ij}\right)$ and $f_A\left(r_{ij}\right) = -B_{ij}\exp\left(-\mu_{ij} r_{ij}\right)$ represent pair repulsion and attraction functions, respectively, and $f_C(r_{ij})$ is a smooth cut-off function given by

$$f_C\left(r_{ij}\right)=\begin{cases}1, & r_{ij}<R_{ij}\\ \frac{1}{2}+\frac{1}{2}\cos\left[\pi\frac{\left(r_{ij}-R_{ij}\right)}{\left(S_{ij}-R_{ij}\right)}\right], & R_{ij}<r_{ij}<S_{ij}\\ 0, & r_{ij}>S_{ij}\end{cases}. \tag{2.2}$$

In the preceding equations, *i* and *j* are atom labels, and r_{ij} is the length of the *ij* bond. The various parameter values are assigned to a specific atom type; parameters that are denoted by double indices, which can correspond to both homo-atomic and hetero-atomic interactions, are obtained by set mixing rules. In the preceding equations, therefore, $A_{ij}=(A_iA_j)^{1/2}$, $B_{ij}=(B_iB_j)^{1/2}$, $R_{ij}=(R_iR_j)^{1/2}$, and $S_{ij}=(S_iS_j)^{1/2}$, while $\mu_{ij}=(\mu_i+\mu_j)/2$ and $\lambda_{ij}=(\lambda_i+\lambda_j)/2$.

The attraction term is modulated by the bond-order function

$$b_{ij}=\chi_{ij}\left(1+\beta_i^{n_i}\zeta_{ij}^{n_i}\right)^{-1/2n_i}, \tag{2.3}$$

which makes the strength of each pair-wise interaction depend on the local environment. The function ζ_{ij} includes angular contributions based on three-body terms, i.e.,

$$\zeta_{ij}=\sum_{k\neq i,j}f_C\left(r_{ik}\right)\omega_{ik}g\left(\theta_{ijk}\right), \tag{2.4}$$

where

$$g\left(\theta_{ijk}\right)=1+c_i^2/d_i^2-c_i^2\Big/\left[d_i^2+\left(h_i-\cos\theta_{ijk}\right)^2\right]. \tag{2.5}$$

All singly-subscripted parameters depend only on a single atom type. The parameter χ_{ij} controls the overall strength of the bond-order modulation, and it is assumed that all charge transfer between dissimilar atoms is accounted for implicitly by the values of the various χ_{ij}. For all homo-atomic interactions, $\chi_{ii}=1$. For hetero-

atomic interactions, it is assumed that $\chi_{ij} = \chi_{ji}$. Previous studies have established $\chi_{Si-Ge} = 1.00061$ [14] and $\chi_{Si-O} = 1.17945$ [61, 62], but no values are currently published for χ_{Ge-O}, which serves as the single fitting parameter in the present study.

Table 2.1 provides a complete summary of all Tersoff parameters for the three elements, Si, Ge, and O used in this work. The first two columns represent two different parameterizations for Si. The first corresponds to the original values specified by Tersoff for pure Si and Si-Ge alloy in ref. [14]. The second set of Si parameters corresponds to the Si-O potential fit in ref. [61], which only considered SiO_2 in the regression process. This version of the Si-O potential is henceforth referred to as the Munetoh-Tersoff model, or MT. Note that in the MT potential, the Si cut-off parameters, R_{Si} and S_{Si}, were modified in the regression process but all other Si parameters were unchanged (Column 2 in Table 2.1). In a subsequent study of Si-on-SiO_2 [62], the same group used the original values of R_{Si} and S_{Si} (Column 1 in Table 2.1); we refer to this version of the Si-O potential as the Lee-Tersoff model, or LT.

The primary reason for reverting to the original values for cut-off parameters in ref. [62] was the fact that the adjusted cut-off parameters in the MT potential degraded the description of pure Si, which was not considered in the original parameterization. For example, the influence of the two cut-off parameter sets on the thermal expansion behavior of pure crystalline Si is shown in Figure 2.1. Clearly, the MT potential leads to an unphysical negative thermal expansion coefficient at elevated temperatures. However, despite this issue, both the MT and LT potentials are used in the present study and detailed comparisons are made. We show that for a complex situation such as SEG on Si with a SiO_2 interlayer, the best parameterization is a compromise among several factors.

Table 2.1 Tersoff potential parameters for Si, Ge, and O used in the present study. The two columns for Si represent the original parameters (T-Si) [14] and refitted values from ref. [61] (M-Si).

	T-Si	**M-Si**	**Ge**	**O**
A (eV)	1.8308×10^{3}	1.8308×10^{3}	1.769×10^{3}	1.88255×10^{3}
B (eV)	4.7118×10^{2}	4.7118×10^{2}	4.1923×10^{2}	2.18787×10^{2}
λ ($Å^{-1}$)	2.4799	2.4799	2.4451	4.17108
μ ($Å^{-1}$)	1.7322	1.7322	1.7047	2.35692
β	1.1000×10^{-6}	1.1000×10^{-6}	9.0166×10^{-7}	1.1632×10^{-7}
n	7.8734×10^{-1}	7.8734×10^{-1}	7.5627×10^{-1}	1.04968
c	1.0039×10^{5}	1.0039×10^{5}	1.0643×10^{5}	6.46921 × 104
d	1.6217×10^{1}	1.6217×10^{1}	1.5652×10^{1}	4.11127
h	-5.9825×10^{-1}	-5.9825×10^{-1}	-4.3884×10^{-1}	-8.45922×10^{-1}
R (Å)	2.7	2.5	2.8	1.7
S (Å)	3	2.8	3.1	2

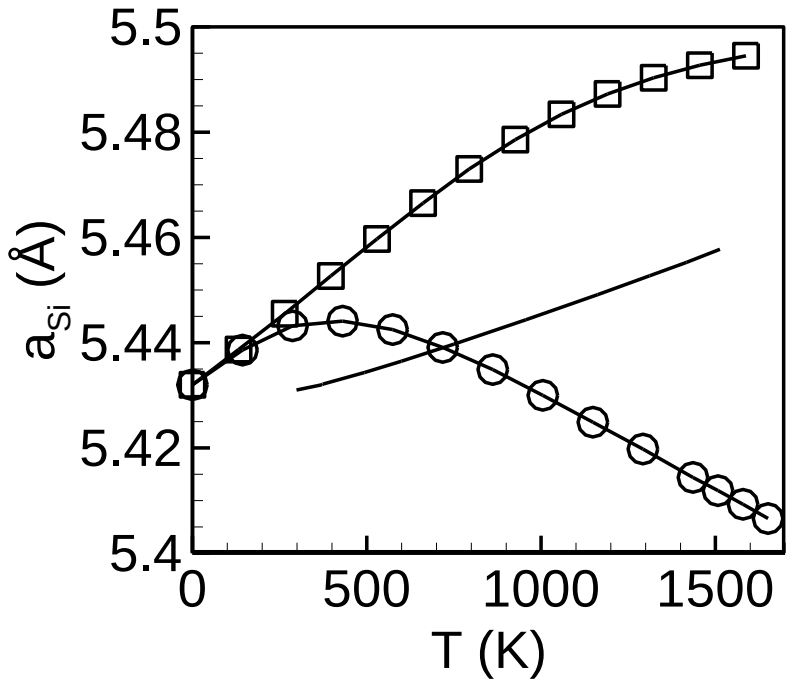

Figure 2.1. Crystalline silicon lattice parameter, a_{Si}, as a function of temperature using the MT (circles) and LT (squares) parameters. The two set of parameters for Si only differ in the specification of the cut-off function. Also shown are experimental values taken from ref. [63] (line).

2.3 Validating the Si –O Interactions

In Sections 2.3 and 2.4, we describe several situations that were used to evaluate the suitability of the Tersoff potential framework to quantitatively describe the Ge-Si-O atomic system. All molecular dynamics simulations were performed using the LAMMPS simulation package [64] with a Nose-Hoover thermostat and barostat [65] to control temperature and pressure, respectively. All simulations were performed in the NPT ensemble with a time step of 1 fs unless otherwise noted. Instantaneous quenches to zero temperature were performed using conjugate gradient energy minimization with a convergence criterion that the energy change between two minimization steps be less than 1×10^{-16} eV.

2.3.1 Bulk Amorphous SiO_2

Amorphous SiO_2 (a-SiO_2) glass was prepared using a multi-step melt-quench sequence. First, a β-cristobalite SiO_2 lattice was created in a cubic 5.82 nm × 5.82 nm × 5.82 nm simulation box with 4096 Si and 8192 O atoms. Periodic boundary conditions were applied in all three directions. The system was annealed at 5000K and zero pressure for 7.5 ns to equilibrate SiO_2 in the liquid state. The temperature was then reduced gradually to 0K at fixed zero pressure with constant cooling rates ranging from 1×10^{11} K/s to 1×10^{15} K/s. It is well known that the structure and energy of silica glass obtained using the MD melt-quench approach depends strongly on the cooling rate [66]. The enthalpy as a function of time for several different cooling rates is shown in Figure 2.2 for MT a-SiO_2 glasses; similar results were obtained with the LT potential. The two slowest cooling rates, 1×10^{11} K/s and 1×10^{12} K/s, result in zero temperature energies that differ by less than 0.3%. In order to balance the computational efficiency and accuracy, a cooling rate of 1×10^{12} K/s was chosen as the default cooling and heating rate in the remainder of this study. It should be noted that the idealized SiO_2 preparation procedure described here (and used throughout the following studies) is qualitatively expected to lead to glass structures that are more consistent with "thermal" oxide, as opposed to the "chemical" oxide grown in refs. [11, 53]. The latter generally is less dense and would contain a substantially higher density of hydroxyl groups. In general, the growth mechanism for the oxide will therefore impact both the chemical and thermophysical properties of the material and presents a source of uncertainty in the predictions and comparisons made throughout this study.

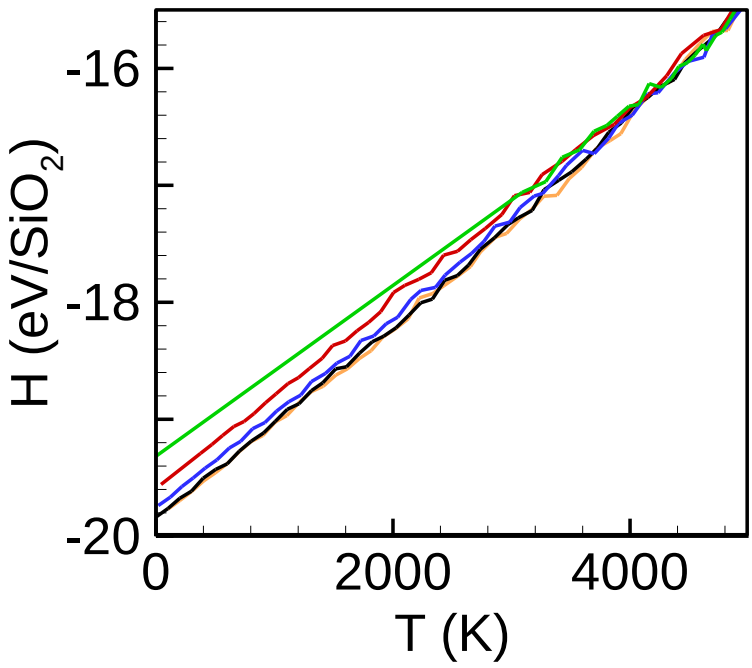

Figure 2.2. Enthalpy per SiO_2 unit as a function of temperature during constant-cooling rate NPT quenches for the MT potential. From top to bottom, the cooling rates are 1×10^{15} K/s (green), 1×10^{14} K/s (red), 1×10^{13} K/s (blue), 1×10^{12} K/s (black), and 1×10^{11} K/s (orange).

The final glass structures generated using the MT and LT potentials are structurally very similar. The densities of MT and LT glasses at 0K are 2.28 g/cm^3 and 2.22 g/cm^3 respectively, which are in excellent agreement with the experimental value (2.2 g/cm^3 [67]). The partial radial distribution functions (RDF) and bond angle distributions for MT and LT glasses generated by quenching at 1×10^{12} K/s to 300K are shown in Figure 2.3 and Figure 2.4, respectively. Also shown for comparison are literature results from DFT calculations [68]. The MT and LT SiO_2 glass RDFs are very similar. Despite the fact that the Si-Si partial RDFs predicted by MT and LT exhibit a peak that is shifted towards slightly larger Si-Si bond distance, both MT and LT a-SiO_2 RDFs are generally in good agreement with the DFT results.

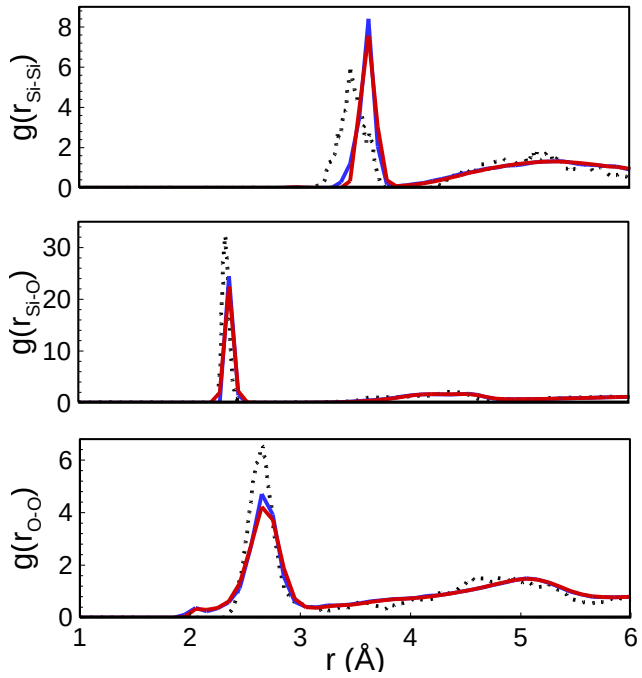

Figure 2.3. Partial radial distribution functions for bulk amorphous SiO_2 quenched to 300K from the liquid state at a constant cooling rate of 1×10^{12} K/s. MT potential – blue line; LT potential – red line; DFT [68] – dashed black line.

The calculated bond-angle distributions in Figure 2.4 again show the structural similarity between MT and LT glasses. Both potentials predict structures that are in good overall agreement with the DFT results, but a sizeable discrepancy in the peak for the Si-O-Si distribution is visible. Note, however, that the DFT results themselves are not in very good agreement with experimental measurements [69] and therefore it is difficult to draw concrete conclusions regarding this discrepancy. In general, the fidelity of DFT calculations can be limited by small system size and short relaxation times, the latter being significant for glassy materials such as a-SiO_2. In conclusion, both MT and LT potentials give similar descriptions for the bulk SiO_2 glass.

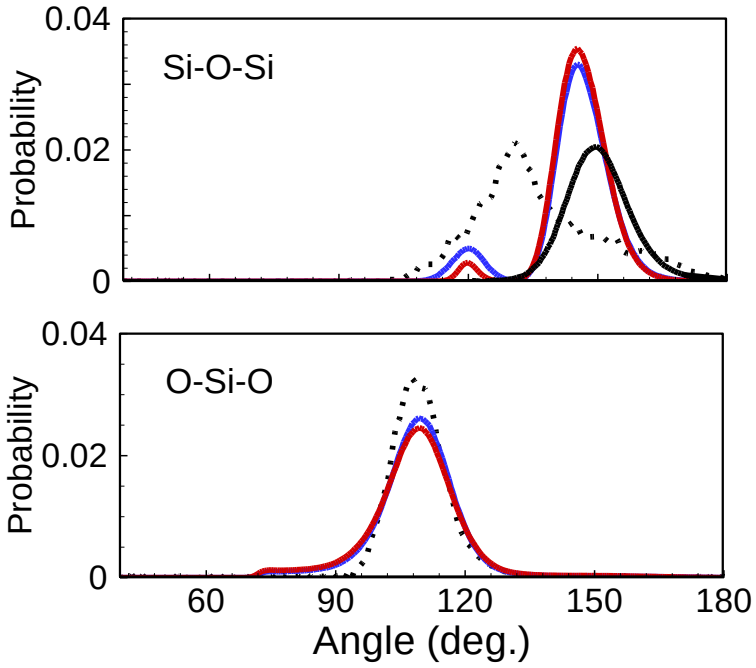

Figure 2.4. Bond-angle distributions for bulk amorphous SiO_2 quenched to 300K from the liquid state at a constant cooling rate of 1×10^{12} K/s. MT potential – blue line; LT potential – red line; DFT [68] – dashed line; experimental measurement [69] – black solid line (Si-O-Si only).

2.3.2 Amorphous SiO_2 Free surface

Amorphous SiO_2 surfaces were generated using the bulk glass structure obtained at the end of the melt-quench sequence outlined in the previous section and removing the periodic boundary conditions in the *z*-direction to create two free surfaces. Two buffer regions with height 10 Å were then inserted at the top and bottom of the simulation box. The system temperature was increased to 2000K at a rate of 1×10^{12} K/s and annealed at 2000K within the NPT ensemble until the internal energy reached a constant value. The a-SiO_2 surface energy was calculated using

$$\sigma_{surf} = \frac{1}{2}\left(E_{sys} - E_{ref}\frac{N_{sys}}{N_{ref}} \right), \tag{2.6}$$

where E_{sys} and N_{sys} represent the energy and number of SiO_2 molecules, respectively, in the system containing the surface. The prefactor accounts for the two surfaces at the top and bottom of the a-SiO_2 slab. The corresponding quantities with subscript "ref" refer to the reference system, which was prepared in an identical manner but with periodic boundary conditions maintained at all surfaces. In the present calculation, the system size was 1728 SiO_2 molecules for both the surface-containing and periodic reference simulation cells, corresponding to a simulation cell with dimensions 4.1 nm × 4.5 nm × 6.0 nm (including the buffer regions). For the system containing the free surfaces, this size corresponds to a total a-SiO_2 surface area of 2×10^{-17} m^2. The calculated surface energies for the MT and LT SiO_2 glasses are 0.42 ± 0.04 J/m^2 and 0.43 ± 0.07 J/m^2, respectively. By comparison, the experimental value [70] is 0.29 J/m^2, which is in reasonable agreement with the amorphous SiO_2 surface energies reproduced by the two potential models.

2.3.3 Si-SiO_2 Interface

The Si-SiO_2 interface energy was calculated using the approach described by Djurabekova and Nordlund [71]. First, bulk a-SiO_2 glass at 0K was created and equilibrated using the melt-quench sequence described in Section 2.3.1. In the present simulations, the cell dimensions at the end of the preparation step were approximately 5.5 nm × 5.6 nm × 5.9 nm. A spherical region with diameter 3.8 nm was then cut out from the center of the domain and a spherical Si nanocrystal with the same size as the cavity (approximately 1440 Si atoms) was inserted into the cavity. The nanocrystal was slightly compressed to leave a gap of 1.5 Å between the Si nanocrystal surface and the surrounding a-SiO_2 matrix to prevent atoms from overlapping. The temperature of the

system was then increased to 300K at a rate of 1×10^{12} K/s, and subsequently annealed at 300K for 5 ns (at zero pressure) to allow the system to equilibrate (Figure 2.5b). The procedure was repeated with different Si nanocrystal orientations to reduce statistical uncertainty.

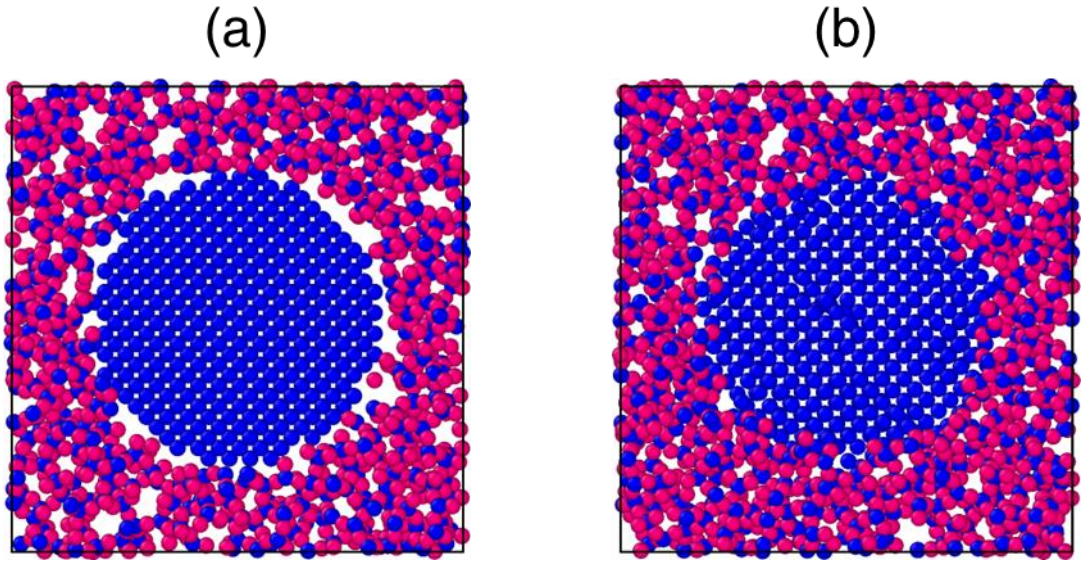

Figure 2.5. (a) Initial configuration of Si nanocrystal in amorphous SiO_2 matrix showing gap between nanocrystal and matrix. (b) Configuration snapshot following 5 ns of equilibration at 300K and zero pressure. Blue spheres are Si atoms; red spheres are O atoms.

The orientationally-averaged Si-SiO_2 interfacial energy, σ_{Si-SiO_2}, was calculated according to the expression

$$\sigma_{Si-SiO_2} = \frac{1}{A}\left[E_{sys} - \left(N_{Si}^{NC}\times E_{Si}^{C} + N_{Si}^{GL}\times E_{Si}^{GL} + N_{O}^{GL}\times E_{O}^{GL}\right)\right], \tag{2.7}$$

where A is the surface area of the nanocrystal, and E_{sys} is the energy of the overall Si/SiO_2 system at equilibrium. N_{Si}^{NC}, N_{Si}^{GL}, and N_{O}^{GL} refer to the number of Si atoms in the Si nanocrystal, Si atoms in the glass matrix, and O atoms in the glass matrix,

respectively. The energies, E_{Si}^{C}, E_{Si}^{GL}, E_{O}^{GL} are the per-atom energy values for Si atoms in the bulk crystal, Si atoms in the bulk glass, and O atoms in the bulk glass, respectively. All the bulk reference states are defined at the same temperature as the test system containing the embedded nanocrystal.

The numbers of Si atoms in the nanocrystal and the a-SiO_2 matrix were determined by locating the nanocrystal interface using a radially-averaged energy profile as shown in Figure 2.6a. The system was divided into shells with thickness 0.5 Å extending outwards from the center of the nanocrystal and the average energy of the atoms within one spherical shell computed. In Figure 2.6a, a decrease in average energy across a ~3 Å window is observed as the system transitions from the nanocrystal region to the glass matrix region. The location of the nanocrystal-glass interface is defined as the center of this window. Note that the energy increase at the particle center exhibited in the MT case (solid line in Figure 2.6a) corresponds to the point defect shown in Figure 2.5b – this was a random event and does not affect the interface energy calculations. The pressure distribution in the embedded nanocrystal and surrounding matrix also was calculated as a function of radial position using

$$P_{shell} = -\frac{1}{3}\sum_{i}^{N_{shell}} (\sigma_{xx}^{i} + \sigma_{yy}^{i} + \sigma_{zz}^{i}), \tag{2.8}$$

where P_{shell} and N_{shell} are the pressure and total number of atoms (regardless of type) of the given shell, and σ_{xx}^{i}, σ_{yy}^{i}, σ_{zz}^{i} are the normal components of the stress tensor of atom *i* in the given shell. The pressure distributions for both MT and LT potentials are plotted in Figure 2.6b.

The resulting Si-SiO_2 interface energies are 1.5 ± 0.03 J/m^2 (MT potential) and 1.1 ± 0.03 J/m^2 (LT potential), respectively; DFT calculations [72] predict a value of 1.5

J/m^2. The MT value is (perhaps somewhat fortuitously) in exact agreement with the DFT result, although both values are in generally good agreement. In summary, both the MT and LT parameterizations provide a reasonably good picture for the bulk a-SiO_2 glass and the Si-SiO_2 interface. While the MT potential predicts an unphysical negative thermal expansion coefficient for bulk Si, it does appear to be slightly better at predicting the Si-SiO_2 interface energy. In the following sections, we address the ability of both potentials to capture the interactions between Ge and a-SiO_2.

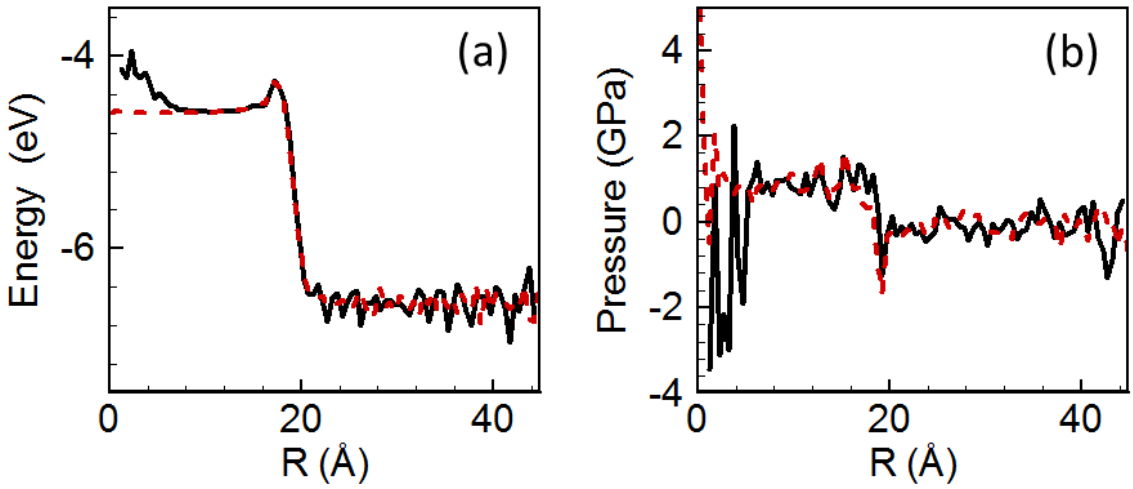

Figure 2.6. (a) Energy and (b) pressure profiles for the embedded nanocrystal-glass matrix systems. Both energy and pressure distributions were radially averaged over shells with thickness 0.5 Å. MT potential—black line; LT potential—red line.

2.4 Atomistic Analysis of Ge on Amorphous SiO_2

2.4.1 Ge-on-SiO_2 Adsorption/Desorption

As mentioned in Section 2.2, there is no published literature that extends the Tersoff potential model to include Ge-O interactions. Here, we mix the original Tersoff parameters for crystalline Ge [14] with the Munetoh *et al.* parameters for O [61] (see Table 2.1) in order to describe the interaction between Ge and O atoms. The parameter

mixing procedure follows the mixing rules specified in the Tersoff potential model [14], leaving one free parameter (χ_{Ge-O}) to control the Ge-O bond strength that we use to match simulation results to experimental measurements. Henceforth, we refer to a normalized Ge-O interaction strength, $\chi_{GS} \equiv \chi_{Ge-O} / \chi_{Si-O}$, to describe and interpret our results. Han *et al.* [11, 12] have measured a variety of properties related to the behavior of Ge atoms adsorbed on amorphous SiO_2, including the Ge desorption energy and the Ge surface diffusion activation barrier. Moreover, the Ge-SiO_2 interface energy and the equilibrium Ge island contact angle on a-SiO_2 also are available in the literature [73, 74]. We first use the Ge desorption energy reported by Han *et al.* to establish bounds on χ_{GS} for both the MT and LT potentials. We then use the fitted value of χ_{Ge-O} to predict the orientationally-averaged Ge-SiO_2 interface energy.

An equilibrated a-SiO_2 free surface was prepared as follows. A periodic cell with dimensions 5.4 × 6.4 ×5.8 nm was employed to equilibrate bulk SiO_2 (see Section 2.3.1), after which the topmost 2 nm was removed to create an exposed SiO_2 surface. Periodic boundary conditions were maintained in the *x* and *y* directions but removed in the *z* direction. The bottom 1 nm of the SiO_2 was held fixed in all subsequent steps. The system was then heated to 2100K within the NPT ensemble at a rate of 1×10^{12} K/s and held at constant temperature until equilibrated as measured by the total potential energy. During equilibration, the normal pressure components in the *x* and *y* directions were set to zero. The prepared surface was then used to characterize Ge adsorption behavior on a-SiO_2 using two different approaches; these are described below in Sections 2.4.1.1 and 2.4.1.2.

2.4.1.1 Grand-Canonical Monte Carlo Simulations

The a-SiO_2 slab prepared above was used to initialize a simulation cell according to the approach prescribed by Bakaev and Steele [75, 76]. The a-SiO_2 surface was divided into a square grid with spacing 0.45 Å in both *x* and *y* directions. At the center of each grid square, a Ge probe atom was placed at least 3 Å above the surface. The Ge atom was brought towards the surface by slowly decreasing its *z* coordinate while keeping the *x* and *y* positions fixed. The height at which the system energy reached a minimum was recorded. The simulation cell boundary in the +*z* direction for each grid square then was set to 8 Å above the respective minimum energy height. The resulting simulation box has a non-uniform boundary at the top *z*-surface as shown in Figure 2.7.

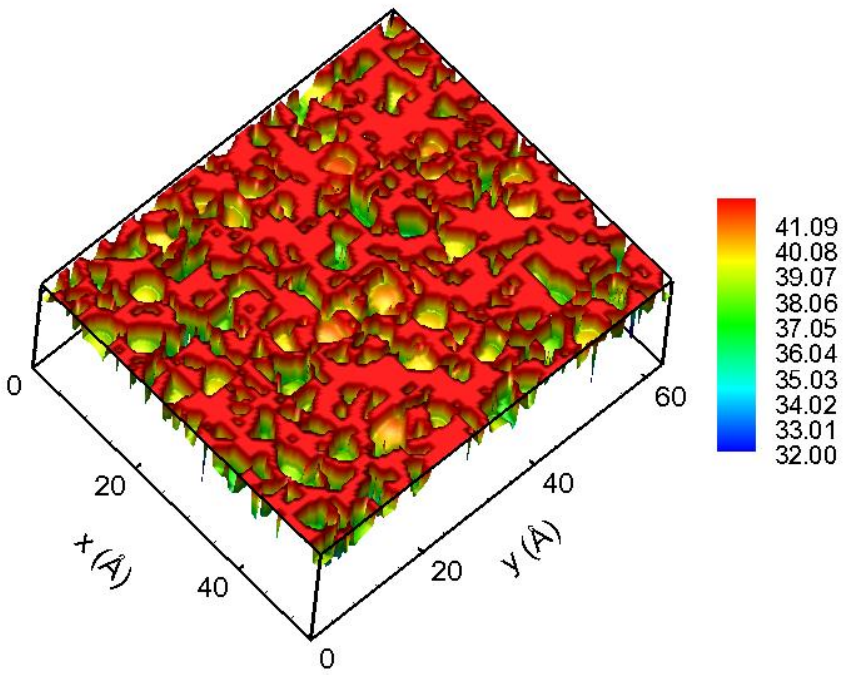

Figure 2.7. Height distribution (in Å) at top simulation cell boundary for GCMC.

Grand canonical Monte Carlo (GCMC) simulations were carried out [77], in which Ge atoms are inserted, deleted, or moved inside the cavity space above the a-SiO_2

surface. Each type of move was attempted with equal probability. The atoms in the a-SiO_2 slab were held fixed throughout the simulation; this assumption is discussed further below. Across the entire surface, the cavity space was defined to extend from 2 Å below the minimum energy height to the top of the system boundary. After equilibrating the system for 50,000 GCMC steps, each run was allowed to evolve for 200,000 GCMC steps. The adsorption data for a given simulation condition (defined by the temperature, the Ge-O bond strength, χ_{GS}, and the potential model (i.e., MT or LT)) was averaged over at least 3 runs in order to improve the statistics. In addition, the entire procedure was repeated using three different a-SiO_2 surfaces to ensure robustness of our results.

Adsorption isotherms were computed for several different values of χ_{GS} for both MT and LT potentials as shown in Figure 2.8 for T = 2100K. For both potentials, the adsorption isotherms converge as χ_{GS} decreases. However, the MT isotherms are more sensitive to changes in χ_{GS} than those obtained with the LT potential. One qualitative difference between the two potentials is apparent in the MT isotherm generated with χ_{GS} = 1.0, which appears to exhibit an inflection point at μ = -4.1 eV. A possible source for this behavior is a transition from dilute (sub-monolayer) adsorption to multi-layer adsorption [78]. Note that higher values of χ_{GS} correspond to increased binding between Ge and O atoms in the a-SiO_2 substrate.

Next, the isosteric heat of adsorption, q_{st}, was calculated from the isotherms in Figure 2.8 according to [75, 79]

$$q_{st} \equiv k_B T^2 \frac{\partial \ln P}{\partial T} = \frac{\partial \langle U \rangle}{\partial \langle N \rangle} + k_B T , \tag{2.9}$$

where N is the number of adsorbate molecules, and $U = U_{sys} - U_{ref}$ is the difference in the potential energy of the system relative to the isolated SiO_2 substrate. The second equality in eq. (2.9) is obtained via the grand canonical partition function and assuming that the vapor phase is ideal [75]. The quantity $\partial\langle U\rangle / \partial\langle N\rangle$ was calculated from the GCMC simulations at a given value of chemical potential using [75]

$$\frac{\partial\langle U\rangle}{\partial\langle N\rangle} = \frac{\langle UN\rangle - \langle U\rangle\langle N\rangle}{\langle N^2\rangle - \langle N\rangle^2}. \tag{2.10}$$

The isosteric heat of adsorption therefore is the enthalpy change in the system as the adsorbate molecules adsorb onto the surface—we take this value to correspond to the desorption energy measured experimentally in ref. [53].

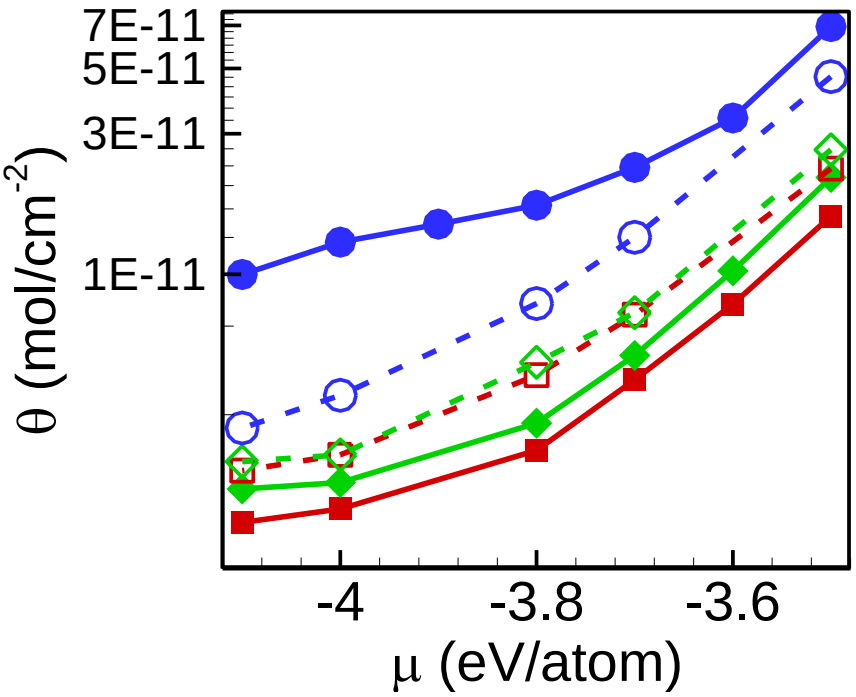

Figure 2.8. Sample Ge-on-SiO_2 adsorption isotherms for the MT and LT potentials at 2100K as a function of chemical potential, at several different values of χ_{GS}. θ is the surface coverage and μ represented the chemical potential. MT: solid lines with filled symbols. LT: dashed lines with open symbols. Blue circles: χ_{GS} = 1.0. Green diamonds: χ_{GS} = 0.8. Red squares: χ_{GS} = 0.6.

The calculated isosteric heats of adsorption at different values of χ_{GS} are shown in Figure 2.9 for the MT and LT potential models at 2100K; also shown is the experimental desorption energy (represented by the dashed line at -42 kJ/mol) from ref. [53]. The dependence of q_{st} on χ_{GS} predicted by the two potential models is qualitatively different, with the MT potential exhibiting a significantly stronger variation. Interestingly, the MT potential predicts a desorption energy that asymptotes at the experimental value as χ_{GS} decreases. The LT potential, on the other hand, predicts values that are much more weakly dependent on χ_{GS}, with an apparent minimum in desorption energy magnitude somewhere in the interval 0.6 < χ_{GS} < 0.8. However, all

the desorption energies obtained with the LT potential, though higher in magnitude, are in reasonable agreement with the experimental value.

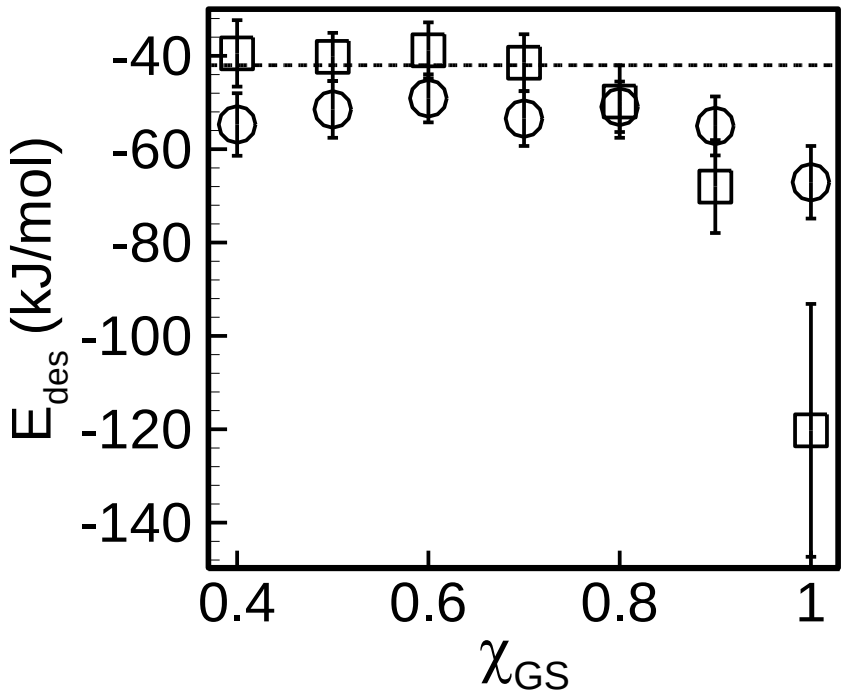

Figure 2.9. Surface-averaged desorption energies for Ge on a-SiO_2 as a function of χ_{GS} for MT and LT potentials. MT—squares; LT—circles.

The MT potential results in Figure 2.9 suggest that an upper bound on χ_{GS} may be estimated at about 0.8; beyond this point the desorption energy increases rapidly in magnitude. The LT results are less definitive but also suggest that χ_{GS}~0.6-0.8 is a reasonable window for capturing the experimentally measured desorption energy. Finally, the a-SiO_2 surface preparation procedure, GCMC simulations, and differential adsorption energy calculation were repeated for the MT potential at T = 1800K in order to probe any temperature dependence. To within the statistical uncertainty, no measurable temperature dependence was found (data not shown) and the results shown in

Figure 2.9 can be assumed to be essentially insensitive to temperature in the interval 1800-2100K.

2.4.1.2 Spatially-Resolved Surface Binding

In order to further investigate the origin of the dependence of the desorption energy on χ_{GS}, we mapped the binding sites on the a-SiO_2 surface using the following procedure. A single Ge atom first was placed 3 Å above the a-SiO_2 surface at a randomly chosen $\{x,y\}$ coordinate. The atom was then moved along the $-z$ direction until it just began to interact with the a-SiO_2 surface. The system configuration at this point was then used to initiate a molecular statics simulation, in which the energy of the system was minimized (with a conjugate gradient method) by allowing the Ge atom to move towards a local energy minimum while holding the SiO_2 atoms fixed. Once the energy minimization process was complete, the Ge atomic energy and position were recorded, and the Ge atom removed. This procedure was repeated $O(10^5)$ times to generate a map of the surface adsorption energy of Ge on SiO_2. The runs were repeated for different values of χ_{GS} for both MT and LT potentials.

Examples of the resulting surface desorption energy maps for several values of χ_{GS} are shown in Figure 2.10 for the MT potential; qualitatively similar results are obtained for the LT potential (not shown). In these maps, the SiO_2 surface was subdivided into a grid of 0.5 Å × 0.5 Å squares and multiple adsorption energy values collected at any point inside the same square were averaged. At low values of the Ge-O bond energy, χ_{GS}, the binding maps appear to show a surface that is largely non-binding, with evenly distributed, isolated pockets of binding. A few of these binding sites are

larger and more strongly binding than the rest. As the value of χ_{GS} increases from 0.6 to 1.0, the total binding area becomes larger and begins to percolate throughout the surface. Interestingly, there is also an increase in areas that exhibit overall repulsion (denoted by red shade in Figure 2.10). These sites represent mechanically stable locations at which the minimum energy was found to be higher than that of the a-SiO_2 substrate without Ge binding. They are likely to arise in response to the energy landscape becoming rougher as χ_{GS} increases, thereby trapping the Ge atom in mechanically stable, but unfavorable, locations during the energy minimization process. At the highest value of χ_{GS}, the binding sites are fully percolated and there exists a large number of "super-binding" sites (denoted by the dark blue shade). The presence of these sites has significant implications for Ge diffusion on the a-SiO_2 surface – this is discussed in more detail in Section 2.4.3.

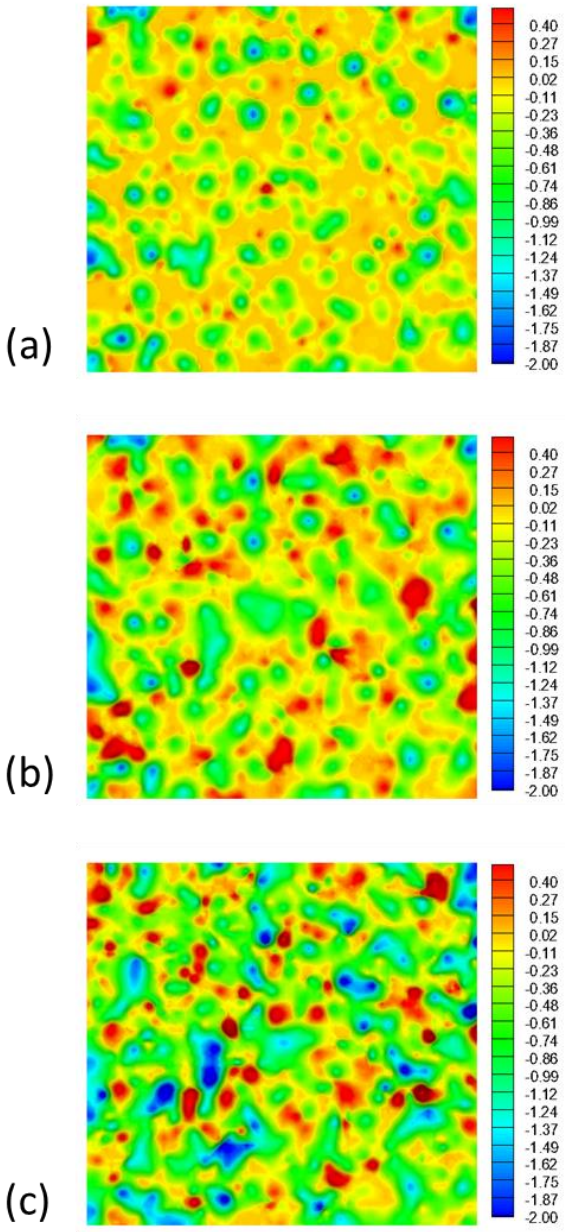

Figure 2.10. Surface binding energy maps for a Ge atom on a-SiO_2 surface (MT potential). From top to bottom, χ_{GS} = 0.60 (a), 0.85 (b), and 1.00 (c). Maps represent 54 Å in the *x*-direction and 64 Å in the *y*-direction. Legend values are in units of eV and are referenced to the a-SiO_2 surface without Ge binding.

The average of the binding energies shown in Figure 2.10, which can be interpreted as another measure of the overall adsorption energy, was calculated for each case by averaging over all binding energies; the results are summarized in Figure 2.11.

For all data points using the random sampling technique, the standard uncertainty is less than 0.2 kJ/mol. Both potentials show similar trends in which the random sampling desorption energy shows the best agreement with the GCMC results at intermediate χ_{GS} values (~0.7–0.8); interestingly, this is precisely where the agreement with the experimental value is also best.

Finally, the assumption that the a-SiO_2 surface is fixed in both the GCMC and random sampling calculations was analyzed. It should be noted that allowing the substrate atoms to evolve during GCMC or during the energy minimization greatly increases the computational costs of both calculations, particularly the former. However, several instances of random sampling were performed with and without relaxation of the substrate atoms and it was found that the differences in the energy was on average less than about 5%, which we believe is smaller than the uncertainty associated with the overall potential accuracy.

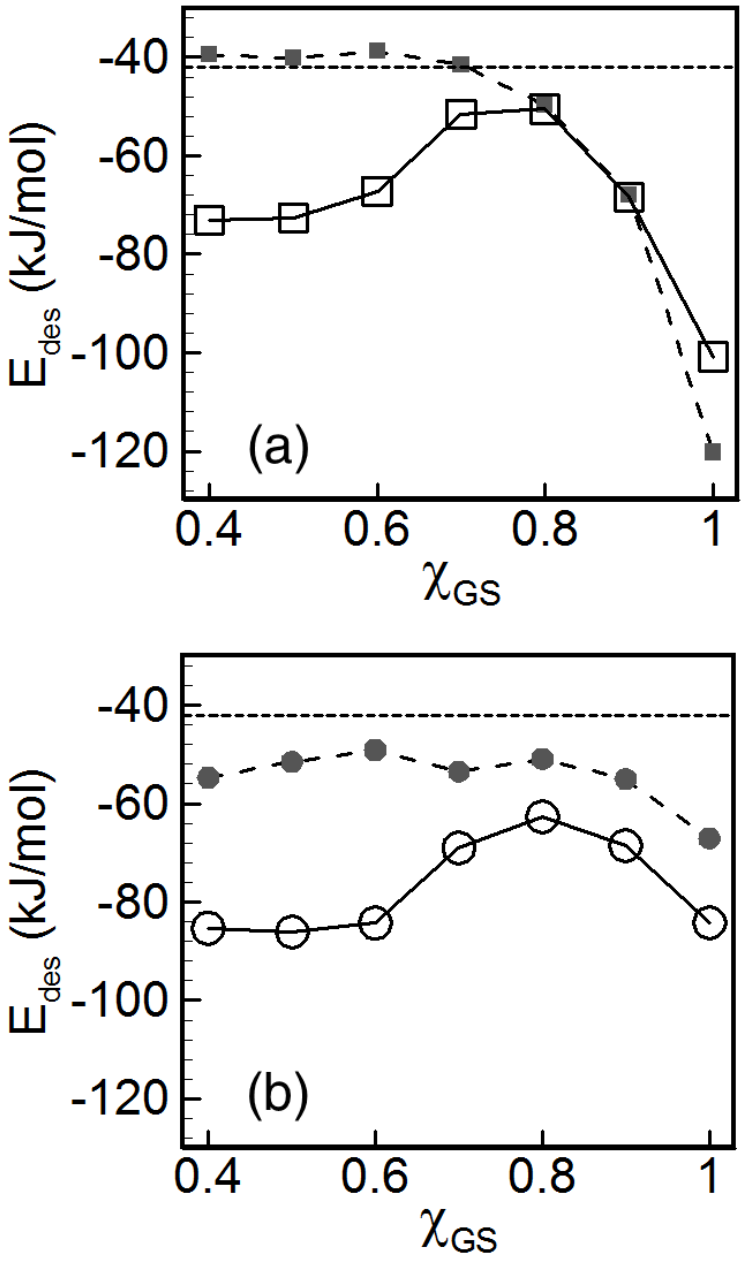

Figure 2.11. Desorption energies as a function of χ_{GS} from random sampling and GCMC simulations for MT potential (a) and LT potential (b). Random sampling – open symbols with solid line, GCMC – filled symbols with dashed line. Horizontal dashed line represents experimental value from ref. [53].

2.4.2 Ge-SiO_2 Interface Energy Calculation

The interaction between Ge and a-SiO_2 predicted by the MT and LT potentials was further examined by calculating the orientationally-averaged Ge-SiO_2 interface

energies with varying χ_{GS} values. The identical simulation setup described in Section 2.3.3 for the Si-SiO_2 interface energy was used here, except that a Ge nanocrystal was placed into the center of the a-SiO_2 matrix. The calculated Ge-SiO_2 interface energies for MT and LT potentials as a function of χ_{GS} are shown in Figure 2.12. Both potentials provide almost identical values across the entire range of χ_{GS} values sampled and the interface energy is found to decrease monotonically with increasing χ_{GS}. However, across the range of χ_{GS} studied here, all the calculated values are significantly higher than the DFT value obtained in ref. [73] (1.0 J/m^2). Considering both the present results and the results in the previous section, χ_{GS} ~0.8 appears to be a reasonable compromise for both MT and LT potentials. It may be worth noting here that the DFT results against which we compare our results may themselves be subject to uncertainties associated with relaxation of the Ge-SiO_2 interface, which is usually based on empirical potentials [73].

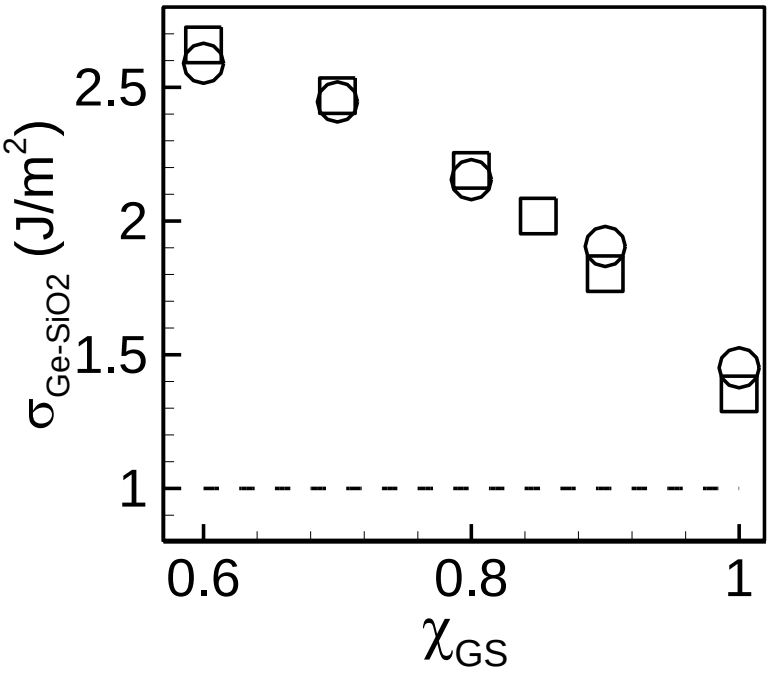

Figure 2.12. Orientationally-averaged Ge-SiO_2 interface energies for MT and LT potentials as a function of χ_{GS}. MT – squares. LT – circles. Dashed line – value from ref. [73]**.**

2.4.3 Additional Considerations

We conclude our analysis by considering two additional experimental observations on a qualitative basis. Leonhardt and Han [12] have estimated the surface diffusion barrier for Ge on a-SiO_2 to be about 0.24 eV using experimental measurements of the saturation Ge island density during MBE as a function of substrate temperature and Ge atom arrival flux. This value, along with the low desorption energy barrier discussed in the previous sections, was estimated to correspond to Ge atom diffusion lengths of 0.5-0.9 nm for substrate temperatures between 673 K and 973 K (with the higher temperature corresponding to the lower diffusion distance).

Unfortunately, simulations of Ge diffusion on an a-SiO_2 surface prepared according to the procedures used in the previous sections do not provide quantitative

measures of the diffusion barrier. Specifically, attempts to compute a statistically meaningful mean square displacement (MSD) for a Ge atom placed on an a-SiO_2 surface were hindered by the fact that Ge atoms tended to either desorb rapidly or to become trapped for long periods of time inside one of the "super-binding" sites shown in Figure 2.10. As expected, the relative probability of these two outcomes depended on the parameter χ_{GS}; larger values of χ_{GS} were associated with increased probability of Ge trapping in a strong binding site. Although we were unable to calculate a diffusion coefficient using the MSD, our qualitative observations are consistent with the short diffusion distances inferred by the experimental results.

Finally, we consider the annealing of Ge on a-SiO_2 substrates, which has been observed to form three-dimensional crystalline Ge islands at low annealing temperatures [80]. A series of MD simulations were performed in which an initially crystalline thin film of Ge with thickness two atomic layers was placed onto an equilibrated a-SiO_2 surface at 2100K with dimensions 5.8 nm × 5.5 nm × 3.0 nm. Keeping the bottom 1 nm of the SiO_2 substrate fixed, energy minimization first was performed to locally relax the system, followed by constant-temperature annealing at 2100K within the NVT ensemble for 10 ns. The film was annealed at several different values of the χ_{GS} parameter using both MT and LT potentials.

As shown in Figure 2.13, the value of χ_{GS} has a profound effect on the final state of the Ge atoms for the MT potential. Similar observations are made with the LT potential (result not shown). For $\chi_{GS} < 0.9$, the Ge layer de-wets the a-SiO_2 surface to produce roughly hemispherical islands that are similar to those observed in ref. [80]. When χ_{GS}~1, however, the Ge wets the a-SiO_2 surface, forming an amorphous film that

is inconsistent with experimental observations. The behavior can be explained by the increased strength of the Ge-O bonding at high χ_{GS}. Repetition of these simulations at lower temperatures showed that the above conclusions are not influenced by temperature, at least to temperatures as low as 1500K on the Tersoff scale. Lower temperatures cannot be readily accessed due to the very slow evolution dynamics.

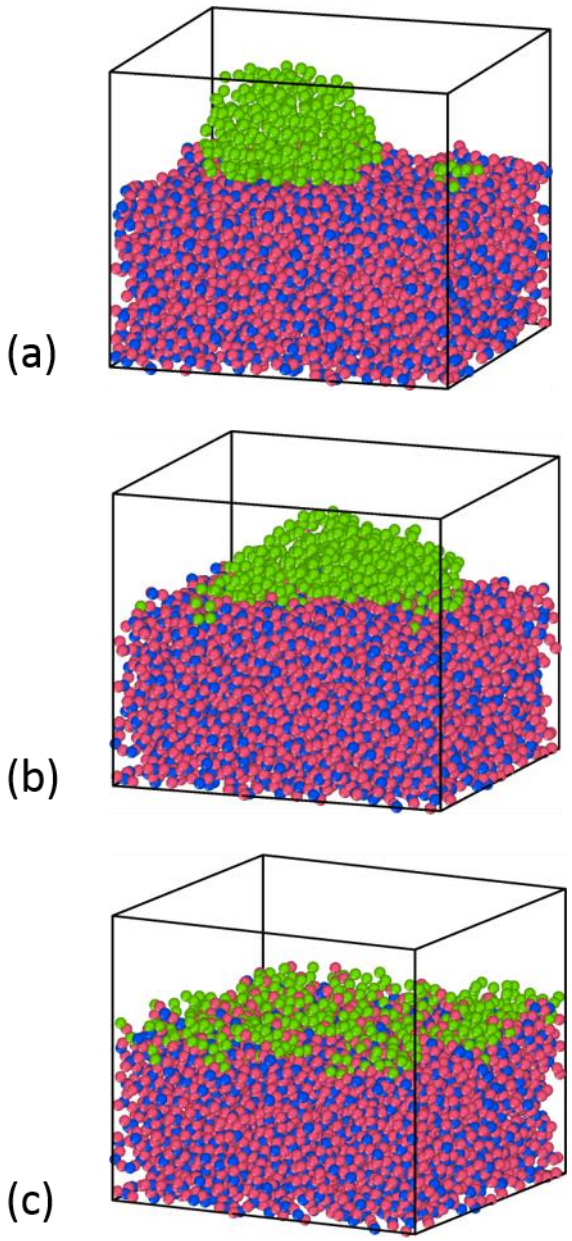

Figure 2.13. Equilibrium configurations of Ge on a-SiO_2 at 2100K using the MT potential. Values of χ_{GS} are (a) 0.8, (b) 0.9, and (c) 1.0. Green atoms are Ge, red atoms are O, and blue atoms are Si.

2.5 Conclusions

An empirical potential description for the Ge-Si-O system based on the Tersoff framework was studied in detail to determine its suitability for use in large-scale

atomistic simulations of selective epitaxial growth of Ge on Si. Two variants of the potential that differ only by the interaction cutoff function for Si atoms were compared using a single free parameter that specifies the strength of the Ge-O interaction. All other parameters were fixed at values that were previously specified in studies of the Si-Ge and Si-O binary systems. We find that both variants are able to describe, at least semi-quantitatively, a wide range of properties that are relevant to Ge-on-Si SEG. These properties include the structure of bulk a-SiO_2, the a-SiO_2 free surface energy, the Si-SiO_2 and Ge-SiO_2 interface energies, and the desorption energy of Ge on a-SiO_2. The best overall representation of these properties is achieved for both potentials when the single fitting parameter used in the present study, χ_{GS}, is about 0.8, or when the Ge-O interaction strength is about 80% of the Si-O interaction. It should be noted that this estimate is based on the assumption that the a-SiO_2 prepared in the present study is a reasonable model for the SiO_2 grown in the experiments. For example, it is well-established that the preparation method of SiO_2, e.g., whether it is chemically or thermally grown, has a significant impact on the Ge diffusion behavior [53].

Our study addresses a universal challenge associated with the use of empirical potentials – namely that it is generally not possible to capture quantitatively all properties of interest, particularly in complex, multicomponent systems. The application of the Tersoff framework to the Ge-Si-O ternary system must be especially carefully validated because of the omission of explicit charge modeling in the consideration of interactions with oxygen. That said, the large number of structural and thermodynamic properties considered in this work indicates that such a framework is sufficiently accurate for capturing many of the processes that are relevant to selective epitaxial growth of Ge on Si/SiO_2 substrates. These studies were pursued in detail in the following chapters. More

generally, the overall success of the Tersoff framework in describing the ternary system studied here can be taken as further empirical evidence for the flexibility of (classical) bond-order potentials to capture complex interatomic interactions.

Chapter 3. Random Nucleation of Ge Islands on Amorphous SiO_2 Surfaces

3.1 Introduction

The need for high-efficiency, yet cost-effective, advanced semiconductor devices has fueled interest in the production of high quality Ge films on Si wafers. The optical and electronic properties of Ge allow for many applications including photodetectors [6, 7] and transistors [81-84]. The lattice compatibility of Ge with the III-V materials also makes it an ideal substrate choice for high-efficiency III-V multijunction solar cells [1, 3-5], but the feasibility of Ge substrates is limited by the high cost of bulk Ge. High-quality Ge films on Si wafers, on the other hand, preserve the advantages of Ge substrates while reducing the cost significantly.

The primary challenge for heteroepitaxial growth of Ge on Si is the lattice mismatch strain between Ge and Si, which drives formation of misfit dislocations in the highly-strained Ge layer [85]. Many approaches have been proposed to overcome the lattice mismatch strain in epitaxial Ge films, including compositional grading [44], cyclic thermal annealing [45], and selective epitaxial growth [8-11]. In compositional grading, the mismatch strain is distributed throughout a thick $Si_{1-x}Ge_x$ layer with gradually increasing Ge content. Cyclic thermal annealing is used to reduce the threading dislocation density in Ge films directly grown on Si wafers by cycles of alternating high and low temperature anneals. Selective epitaxial growth (SEG) has been used to produce strain-free, high-quality Ge film on Si without the need for costly thermal treatments or thick, compositionally-graded Ge layers. In SEG, an amorphous masking material (usually SiO_2 or Si_3N_4) is applied on top of the Si wafer surface. Nanoscale cavities are then introduced in the mask layer, either by high-resolution lithography [9, 10] or by self-

limiting chemical reactions [11]. Subsequent Ge deposition leads to the formation of epitaxial Ge islands at the base of these cavities ("seeding pads") which then overgrow onto the amorphous masking layer. The epitaxially-adhered islands eventually grow and coalesce into a contiguous crystalline film on top of the amorphous mask. The key aspect of SEG is that the epitaxial contact area between Ge and Si layers is restricted to the nano-sized pads, which significantly lowers the mismatch strain in the Ge layer and suppresses the formation of misfit strain defects. Indeed, various studies have reported threading dislocation densities in SEG films as low as $O(10^6)$ cm^{-2}, making such films suitable substrates for the fabrication of III-V structures [13].

While the low defect densities in SEG films reported to date are promising, further improvements will require a more fundamental understanding of the defect formation processes that lead to stacking faults and threading dislocations. For example, one poorly understood phenomenon is the formation of stacking-faults upon island-island coalescence during SEG [13]. In this chapter, we study the secondary nucleation of Ge on a-SiO_2 with the Ge-Si-O potential framework presented previously in Chapter 2. While secondary nucleation of Ge, i.e., direct nucleation of (amorphous) Ge islands on the a-SiO_2 mask, is not a technical challenge in SEG, we focus on this process because it has been characterized experimentally in great detail [12]. By comparing our simulation predictions with experiment, we will use the process of secondary nucleation as a means to establish the quantitative validity and predictive capability of the simulations for studying important defect formation process in SEG.

Leonhardt et al. [12] have studied in detail the kinetics of Ge island nucleation on amorphous SiO_2 (a-SiO_2) using scanning electron microscopy. Overall, it was found that Ge islands grow on a-SiO_2 by direct impingement from the vapor, rather than by adatom

surface diffusion, principally because Ge adatoms tend to desorb before they diffuse an appreciable distance on the surface. As a result, the *condensation coefficient*, defined as the amount of adsorbate condensed on the surface versus the total amount deposited, was found to be small across all temperatures considered in ref. [12]. The small characteristic Ge surface diffusion distance on SiO_2 was corroborated by the absence of Ge adatom exclusion zones around the pads that typically arise as a consequence of diffusion-limited island growth [12].

Here, we use the experimental results in ref. [12] to (1) establish the overall quantitative reliability of the empirical potential-based atomistic simulation framework described in Chapter 2 and (2) determine the feasibility of meaningfully studying defect formation in SEG with fully-resolved atomistic simulations such as molecular dynamics (MD). The latter issue is a well-known one in the broader context of deposition processes. The difficulties are two-fold. First, experimental atomic deposition rates, typically $O(10^{13}\text{-}10^{14})$ atom/cm^{2}s, are many orders-of-magnitude too slow to be simulated directly with methods such as molecular dynamics, which are limited to timescales on the order of hundreds of nanoseconds. Second, sufficiently large substrate areas need to be considered to allow for the proper capture of island size and density distributions. Empirical potential MD simulations currently are limited to tens to hundreds of nanometers per spatial dimension, and increasing the number of atoms usually comes at a cost of a further reduction in the accessible timescale. Together, these restrictions make the direct MD simulation of deposition rather challenging, and constrain simulation conditions to unrealistic operating conditions, which may or may not meaningfully represent relevant experimental ones.

It should be noted that many alternatives to direct MD simulation exist for simulating atomic deposition processes. For example, a commonly employed simulation technique to overcome the timescale problem is kinetic Monte Carlo (KMC) [86-90]. In KMC, the system is evolved by selecting processes from a predefined event catalog in a way that is biased by their rates. Slow processes are picked less often but also correspond to larger increments in system time, in principle providing the KMC approach with an intrinsic ability to adapt to the timescale of the process being simulated. Moreover, the event catalog may be defined at any resolution so that very fast (and uninteresting) processes such as atomic vibration can be coarse-grained out of the simulation. In fact, lattice-based kinetic Monte Carlo, in which all particles are confined to a predefined, rigid grid, is an extremely popular and computationally efficient variant of KMC [88, 91-94] and has been widely applied to the simulation of atomic deposition on (usually low-temperature) crystalline substrates [88, 95-100].

The need for a predefined catalog, however, implies that KMC requires *a priori* knowledge of all possible events and their rates, so assumptions have to be made on choosing processes to be included in the model. The accuracy of any KMC simulation depends strongly on these assumptions and the amorphous nature of the a-SiO_2 substrate and Ge islands makes it very difficult (or even impossible) to specify a comprehensive event catalog [101]. The development of on-the-fly atomistic KMC methods [102-104] addresses this limitation by building dynamically the catalog of events during the simulation via searches over all energy saddles accessible from each current configuration. On-the-fly KMC is usually posed at full atomistic resolution and therefore naturally accounts for the complex energy landscapes associated with amorphous systems. However, these methods are much less computationally efficient than the static

catalog or lattice-based variants of KMC, and in fact not necessarily much faster than MD simulation.

A variety of techniques also have been proposed to accelerate MD simulations. These include temperature-accelerated dynamics (TAD) and hyperdynamics [105, 106]. Very briefly, these methods aim to speed up MD simulation by increasing the rate at which the system escapes from one energy basin to another. While they have been successfully applied to study island growth [107, 108], their application to the system of interest (Ge on a-SiO_2) is complicated by several elements. Firstly, because the system evolution slows down as temperature decreases, the deposition temperatures considered in our study are quite high (0.7—0.9 T_m) due to computational efficiency considerations. This limits gains from methods such as TAD. Moreover, the complex morphologies associated with amorphous islands on an amorphous substrate makes it difficult to clearly identify transition events to apply the other methods.

In this Chapter, we apply direct MD simulation to the study of Ge deposition on a-SiO_2 and make close connections to experimental results in ref. [12] using an analytical rate equation framework as a bridge [109, 110]. Reinforcing our previous conclusions [111], we demonstrate that the empirical potentials used to describe the interatomic interactions between Si, Ge, and O atoms appear to provide an excellent quantitative picture for Ge island deposition on a-SiO_2, matching the experimental data in several key aspects. We also demonstrate quantitatively that it is indeed possible to directly access experimentally relevant deposition regimes with MD simulation, even if the actual deposition rates are unrealistically rapid. The latter finding has important implications for the simulation of atomic deposition in a variety of systems.

The remainder of the Chapter is organized as follows. In Section 3.2, a brief summary is provided of the analytical rate equation approach developed by Venables and others [109, 110, 112-114]. As noted above, the rate equation theory is used to provide a quantitative framework for establishing a rigorous connection between simulation and experiment. The simulation methods and system initialization are discussed in Section 3.3. In Sections 3.4 to 3.6, results are provided for various deposition simulations, along with analysis based on rate equation theory and comparison to experimental data. Finally, conclusions are presented in Section 3.7.

3.2 Rate Equation Theory for Island Nucleation and Growth

Analytical descriptions based on rate equations provide a powerful framework for understanding various features of island evolution during deposition. Here, we briefly describe the framework originally proposed by Venables and others [109, 110, 115] that describes island growth in terms of low-order moments, namely the island density and coverage. More detailed descriptions also have been proposed to include more complete descriptions of island growth by higher-order moments such as island size and/or capture zone distributions [116-123], but these are not addressed here.

The rate equation approach proposed by Venables [109, 110, 114, 115] assumes that subcritical clusters dissociate quickly compared to other processes and therefore exist in a quasi-steady state relative to stable species, i.e.,

$$\frac{n_j}{N_0} = C_j \left(\frac{n_1}{N_0} \right)^j \exp(\beta E_j), \tag{3.1}$$

for all j less than or equal to the critical nucleus size, i [113]. In eq. (3.1), N_0 is the number of adsorption sites, n_1 and n_j are the concentrations of monomers and clusters

of size j, respectively. C_j is a statistical weight factor representing the orientation degeneracy for j-sized clusters, and E_j is the binding energy of j-sized clusters relative to j individual monomers adsorbed on the surface.

Ignoring the spatial variation of monomers on the surface due to capture by existing clusters and assuming only monomers are mobile, the mass balance for monomer concentration is

$$\frac{dn_1}{dt} = F - \frac{n_1}{\tau_a} - 2U_1 - \sum_{j>1}^{i} U_j - U_x , \tag{3.2}$$

where F is the deposition flux and τ_a is the adatom adsorption residence time, which is related to the monomer desorption rate as $\tau_a^{-1} \sim \exp(-\beta E_a)$, where E_a is the adsorption energy barrier. The term $2U_1$ in eq. (3.2) represents the rate of dimerization, U_j is the net rate of formation of size j clusters by monomer addition for ($j < i$), and U_x is the rate at which monomers join all stable clusters ($x = \{i+1, i+2, \cdots, \max\}$) via surface diffusion and direct impingement from the vapor,

$$U_x = \sigma_x D n_1 n_x + F a_x n_x . \tag{3.3}$$

Here, σ_x is the capture number for any stable islands and is assumed to be invariant with size, a_x is the average substrate surface area covered by stable clusters so that $a_x(t) n_x(t) \equiv Z(t)$ represents the total (time-dependent) surface coverage by stable clusters. Finally, D is the diffusivity of monomers and is given by

$$D \sim \exp(-\beta E_d) , \tag{3.4}$$

where E_d is the diffusion barrier for monomers on the surface.

The mass balance equations for the concentrations of metastable clusters, n_j, stable clusters, n_x, and the total number of monomers in all stable islands, N_x, are then given by

$$\frac{dn_j}{dt} = U_{j-1} - U_j, (1 < j \le i) = 0, \tag{3.5}$$

$$\frac{dn_x}{dt} = U_i - U_c - U_m, \tag{3.6}$$

$$\frac{dN_x}{dt} = \sigma_x D n_1 n_x + FZ(t). \tag{3.7}$$

where the quasi-steady state assumption for metastable clusters was applied in eq. (3.5). The terms U_i, U_c, and U_m in eq. (3.6) represent the net rates of stable cluster nucleation and stable cluster coalescence due to growth and surface diffusion, respectively. Because monomers are assumed to be the only mobile species on the surface, $U_m \sim 0$ in eq. (3.6) and the dominant mechanism for stable island nucleation at low surface coverage proceeds by monomer addition to critical-sized clusters, i.e.,

$$U_i = \sigma_i D n_1 n_i. \tag{3.8}$$

Further assuming that islands are three-dimensional hemispheres regardless of size, U_c may be approximated as

$$U_c \approx \frac{1}{2} \sum_k {n_x}^2 \frac{d}{dt} \left(\pi \left(2r_x \right)^2 \right), \tag{3.9}$$

where r_x is the average radius for stable clusters. The same assumption also allows N_x in eq. (3.7) to be expressed in terms of r_x and $Z(t)$, i.e.,

$$N_x = n_x \left(\frac{2\pi}{3\Omega} {r_x}^3 \right) = \frac{2}{3\Omega} \left(\pi n_x \right)^{-1/2} Z(t)^{3/2}. \tag{3.10}$$

During the early stages of deposition, n_1 is completely dictated by the deposition flux, i.e., $n_1 = Ft$. The duration of this initial transient, τ, is a combination of the adsorption and diffusion time scales and is defined by

$$\frac{1}{\tau} = \frac{1}{\tau_a} + \sigma_x D n_x . \tag{3.11}$$

Finally, expanding eqs. (3.2), (3.6), and (3.7) and rearranging gives a system of equations describing the rate of island nucleation:

$$\frac{dn_1}{dt} = F(1 - Z(t)) - \frac{n_1}{\tau}, \tag{3.12}$$

$$\frac{dn_x}{dt} = \sigma_i N_0^{1-i} D\left(F\tau\right)^{i+1} \exp(\beta E_i)\left(1 - Z(t)\right) - 2n_x \frac{dZ(t)}{dt}, \tag{3.13}$$

$$\frac{dZ(t)}{dt} = \Omega\left(\frac{\pi n_x}{Z(t)}\right)^{1/2} F\left[\sigma_x D n_x \tau\left(1 - Z(t)\right) + Z(t)\right]\left(1 - \frac{1}{3}\frac{d\left(\ln n_x\right)}{d\left(\ln Z(t)\right)}\right)^{-1}, \tag{3.14}$$

where Ω is the atomic volume of monomers in stable clusters. Equations (3.12) – (3.14) may be solved analytically by transforming the dependent variable from time, *t*, to surface coverage, *Z*(*t*) [109]. The maximum number of stable clusters, which is readily measured experimentally, may be obtained from eqs. (3.12) – (3.14) by setting eq. (3.13) to zero and rearranging to give [110, 114]

$$\left(\frac{n_{x,\max}}{N_0}\right)^{3/2}\left(1 + \sigma_x D\tau_a n_{x,\max}\right)^i \left(Z_0 + \sigma_x D\tau_a n_{x,\max}\right) \simeq \left(\frac{F}{N_0{}^2 D}\right)^i \exp\left(\beta E_i\right)\left(D\tau_a N_0\right)^{i+1}, \tag{3.15}$$

where Z_0 is the coverage at the occurrence of the maximum cluster density. The value of Z_0 is typically less than 0.2 [110]. Equation (3.15) may be simplified for different *condensation* regimes characterized by the dominant cluster growth mechanism. In the case that clusters grow solely by direct impingement from the vapor phase, the

condensation regime is said to be *extremely incomplete*. This situation occurs when the adatom adsorption timescale is short and the characteristic diffusion length of adatoms is much smaller than the inter-island distance. Conversely, the *complete condensation* regime refers to the situation when the characteristic diffusion length is larger than the inter-island distance and adatom desorption is negligible, so that islands grow by capturing diffusive adatoms. An intermediate regime, referred to as *initially incomplete condensation*, occurs when desorption is slow and the characteristic diffusion length is smaller than the inter-island distance. In this regime, adatoms are mobile but may desorb before being captured by existing islands, so the condensation is incomplete. However, in this case the condensation regime later becomes complete as islands grow and the inter-island distance decreases below the characteristic diffusion length. Since surface capture becomes the governing island growth mechanism at this stage, the system behaves identically as in the complete condensation regime [110].

As mentioned previously in the Introduction, the experimental study by Leonhardt et al. [12] suggested that Ge islands on a-SiO_2 grow via direct impingement from the vapor, i.e. the condensation is extremely incomplete. In this case, the monomer capture area in the vicinity of a stable cluster is much less than the substrate surface area occupied by the cluster, i.e. $\sigma_x D\tau_a n_x << Z$. This condition simplifies eq. (3.15), which becomes [114]

$$n_{x,\max} \sim (F)^{\frac{2i}{3}} \exp\left(\frac{E}{k_B T}\right), \tag{3.16}$$

where $E = \frac{2}{3}\left(E_i + (i+1)E_a - E_d\right)$. As mentioned above, the value of $n_{x,\max}$ can be straightforwardly measured in experiments. Therefore, eq. (3.15) and its solutions in the

three condensation regimes have been widely used to deduce the activation energies for adsorption and surface diffusion, as well as critical cluster binding energies in a variety of systems [124-127].

3.3 Ge Deposition Simulations on Amorphous SiO_2 surfaces

All simulations were performed using an empirical interatomic potential model for the ternary Ge-Si-O system based on the Tersoff framework [14]. In ref. [111], we combined the well-established Tersoff parameters for the binary Si-Ge system [14] with a recent parameterization for the Si-O binary system [61]. Using a single fitting parameter that represented the Ge-O interaction strength, the ternary potential model was found to reproduce well a wide range of structural and thermodynamic properties for bulk a-SiO_2, the Si-SiO_2 interface, and Ge adatom binding on a-SiO_2 surfaces. In this chapter, the MT variant of the potential model was used. All molecular dynamics simulations were performed using the LAMMPS software package [64]. The simulations were conducted in the NPT ensemble unless otherwise specified, and Nose-Hoover thermostats and barostats [65] were applied to control the temperature and pressure of the system, respectively. A time step of 1 fs was applied in all cases. Static relaxations were performed using the conjugate gradient algorithm in the LAMMPS software.

3.3.1 Preparation of a-SiO_2 Surfaces

Bulk a-SiO_2 was prepared using a melt-quench sequence; also see ref. [111]. First, a cubic β-cristobalite SiO_2 lattice consisting of 4096 SiO_2 units with dimensions 5.8×5.8×5.8 nm^3 was created with periodic boundary conditions applied on all sides of the system. The SiO_2 lattice was melted at 5000K for 5 ns, followed by rapid cooling to

0K at a linear cooling rate of 1×10^{12} K/s. The quality of the resulting a-SiO_2 has been discussed in detail in our previous study [111] and overall exhibits good agreement with bulk density, radial distribution function, and bond angle distributions predicted by *ab initio* calculations and experiments.

Following the formation of bulk a-SiO_2, periodic boundary conditions in the *z*-direction were removed and the slab sliced in two along the *xy*-plane to create an a-SiO_2 slab (that is still periodic in the *xy*-plane) with dimensions approximately $6\times6\times3$ nm^3. In all subsequent deposition simulations, the bottom 1 nm of the a-SiO_2 slab was fixed to emulate a bulk-like environment for the 2 nm-thick active layer above. In each case, before Ge deposition was initiated the temperature in the active layer was increased at a linear rate of 1×10^{12} K/s until the deposition temperature, which ranged from 1800K to 2300K. The temperature was then held constant until the system potential energy equilibrated; the equilibration period was typically 30 ns long. Following equilibration, the a-SiO_2 slab was replicated four times in the *x* and *y* directions, resulting in a slab with dimensions $24\times24\times3$ nm^3. The replicated surface finally was equilibrated at constant temperature for a further 0.2 ns. Note that for all deposition simulations, the top *z*-boundary of the simulation domain was placed at least 5 nm higher than the highest point of the a-SiO_2 surface to prevent any bias in the Ge deposition due to boundary effects.

3.3.2 Modeling Ge Deposition on Amorphous SiO_2

Simulations of Ge deposition on the a-SiO_2 surface were performed in the NVT ensemble. A schematic representation of the deposition simulation system is shown in Figure 3.1. Ge atoms were introduced into the region above the slab at a constant rate to simulate deposition at a prescribed flux ranging from 5×10^{21} to 6.9×10^{24} atoms/cm^2s.

The *x* and *y* coordinates of each inserted atom were chosen randomly, while the *z*-coordinate was set to be 5 Å above the maximum height of all atoms within a 5Å radius along the *xy*-plane. All inserted atoms were initialized with downward velocity corresponding to the deposition temperature.

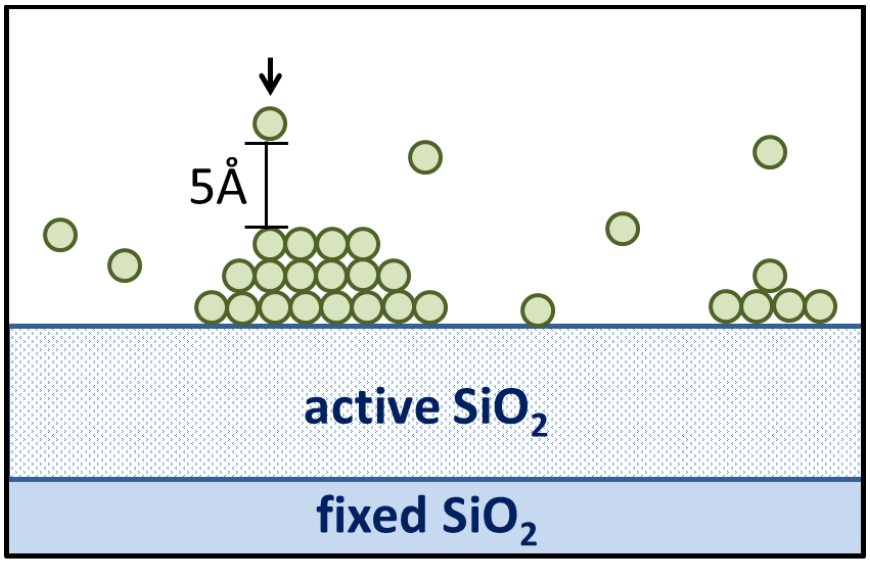

Figure 3.1. Schematic diagram of the Ge on a-SiO_2 deposition system. Ge atoms are represented by the green particles. The fixed and active SiO_2 layers (1 nm and 2 nm in thickness, respectively) are denoted in the figure. The arrow indicates a Ge atom that was newly added to the system, placed at 5Å above the highest atom within a 5Å radius along the *xy* plane. This atom is given a downward velocity moving towards the a-SiO_2 surface.

Following each atomic insertion, the system was evolved with MD until the addition of the next Ge atom. An island was defined as a group of interacting Ge particles consisting of two or more Ge monomers with inter-particle distances being less than the Ge-Ge potential cutoff distance (3.1 Å). A Ge particle was defined as adsorbed if its distance to the nearest Si or O atom is within the respective Ge-Si or Ge-O potential cutoff distances (2.9462 Å and 2.49 Å, respectively).

Ge atoms desorbing from the a-SiO_2 surface require special attention. Under some conditions, namely when the deposition rate is large, atoms rising from the surface may collide and bind with downward-moving atoms to form aggregates. These aggregates represent an artifact that may impact the effective deposition flux to the surface. In order to address this issue, checks were performed before every Ge atom addition to remove any desorbed Ge atoms from the system. Desorbed atoms were identified as Ge atoms with an upward-directed (+*z* direction) velocity component and zero potential energy.

3.4 Single Ge Adatoms on a-SiO_2

Measurements of Ge adatom residence time and displacement distributions on the a-SiO_2 surface were made by depositing a single Ge atom onto the surface and then tracking its trajectory. The displacement, X_a, of the Ge atom on the surface was defined as the distance between the positions at which the particle adsorbs (potential energy first becomes nonzero) and desorbs (potential energy becomes zero). The residence time, τ_a, correspondingly was defined as the duration of the adsorption time. For each sample, the simulation was terminated either when the Ge atom desorbed or when the simulation time exceeded 50 ps. The single-atom simulation described here was repeated at least O(10^4) times at both 1800K and 2300K to obtain converged distributions for X_a.

Our previous characterization of the a-SiO_2 surface [111] showed that the surface is highly heterogeneous in terms of Ge binding strength, and is comprised of favorable binding sites interspersed with non-binding, or even repulsive, patches. The presence of unfavorable binding regions in between the binding sites leads to extremely short adatom

residence time and surface displacement distributions. As shown in Figure 3.2, more than 90% of Ge adatoms leave the surface after diffusing less than 3 Å at both temperatures. The corresponding residence time for these displacements is less than 1 ps. In fact, the mean displacement before desorption for a Ge adatom on the surface is less than 1 Å, which is on the order of the atomic vibrational amplitude, further emphasizing that adatoms are essentially immobile under the simulations conditions considered here.

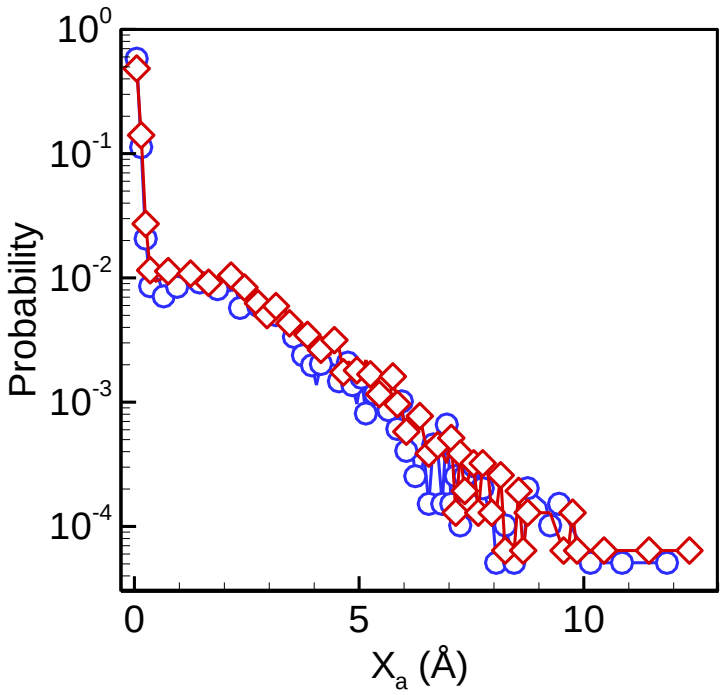

Figure 3.2. Ge atom displacement on amorphous SiO_2 surface at 1800K and 2300K. Blue circles: 1800K; red diamonds: 2300K.

3.5 Deposition and Island Nucleation

Ge deposition runs were carried out for deposition fluxes ranging from 5×10^{21} atoms/cm^{2}s to 6.9×10^{24} atoms/cm^{2}s at temperatures between 1800K and 2300K. Figure 3.3 shows four top-down snapshots of the a-SiO_2 surface, all taken when the number density of Ge atoms brought down to the surface, N_{add}, had reached 6.6×10^{14} atoms/cm^2;

the four snapshots correspond to different deposition fluxes and temperatures (see Figure 3.3 caption). While the formed Ge islands are always randomly distributed and amorphous in structure, their areal density and sizes are strongly impacted by the deposition rate and substrate temperature. Higher temperatures clearly destabilize islands and lead to lower densities of smaller islands, while increasing the deposition rate leads to a higher density of larger islands.

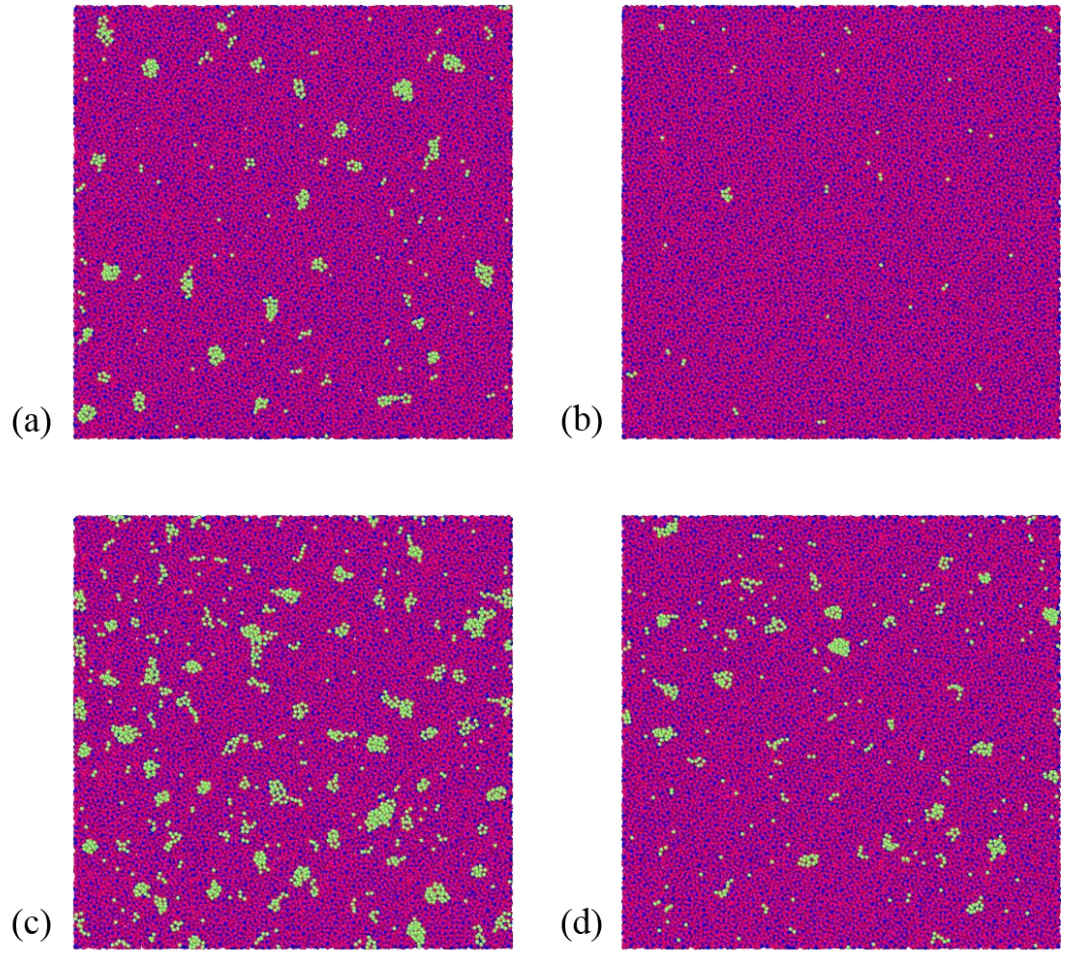

Figure 3.3. System configurations at N_{add} = 6.6×10^{14} atoms/cm^2 for different substrate temperatures and deposition fluxes: (a) 2000K, 2.76×10^{22} atoms/cm^{2}s, (b) 2200K, 2.76×10^{22} atoms/cm^{2}s, (c) 2000K, 1.38×10^{24} atoms/cm^{2}s, (d) 2200K, 1.38×10^{24} atoms/cm^{2}s. Red atoms: O. Blue atoms: Si. Green atoms: Ge. Rendering of the system was generated using the OVITO visualization tool [128].

The stable surface island density, n_x, is shown in Figure 3.4 as a function of substrate temperature at several deposition fluxes for $N_{add} = 3.47\times10^{14}$ atoms/cm^2. Here, and in all subsequent discussion, we assume that the critical island size, *i*, is less than 2 and all clusters are included in the evaluation of n_x. In Section 3.6, we self-consistently validate this assumption. At every flux, the island density decreases slowly as the temperature is increased from 1800K to about 2000K and then decreases more rapidly as the temperature is further increased. Over the entire flux range considered, and for all temperatures, higher fluxes generally correspond to higher island densities. These trends are in qualitative agreement with the experimental observations by Leonhardt et al. [12].

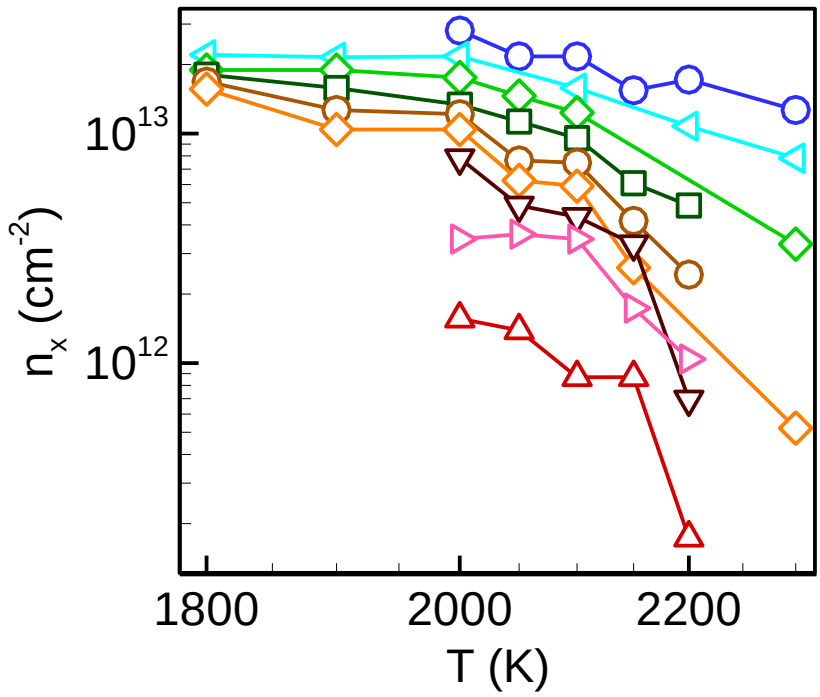

Figure 3.4. Surface island density, n_x, as a function of temperature at different deposition fluxes at N_{add} = 3.47×10^{14} atoms/cm^2. Blue circles: F = 4.14×10^{24} atoms/cm^{2}s. Cyan left triangles: F = 1.38×10^{24} atoms/cm^{2}s. Green diamonds: F = 6.9×10^{23} atoms/cm^{2}s. Dark green squares: F = 3.45×10^{23} atoms/cm^{2}s. Brown circles: F = 1.38×10^{23} atoms/cm^{2}s. Orange diamonds: F = 6.9×10^{22} atoms/cm^{2}s. Dark brown gradients: F = 2.76×10^{22} atoms/cm^{2}s. Pink right triangles: F = 1.38×10^{22} atoms/cm^{2}s. Red deltas: F = 5×10^{21} atoms/cm^{2}s.

The evolution of Ge monomer density, n_1, the total island density, n_x, and the total amount of Ge condensed on the surface, N_{cond}, as a function of N_{add} at 2100K are shown in Figure 3.5 for high (F = 4.14×10^{24} atoms/cm^{2}s), medium (F = 6.9×10^{23} atoms/cm^{2}s), and low (F = 2.76×10^{22} atoms/cm^{2}s) deposition fluxes. There are several processes dictating the evolution of n_1 and n_x, including (1) monomer formation on the surface by deposition, (2) monomer desorption from the surface, and (3) island nucleation and growth as Ge atoms from the deposition flux impinge onto monomers or islands already present on the surface. During the initial stages of deposition when the surface coverage is very low, n_1 evolves according to a balance between monomer deposition

and monomer desorption, and no islands are present at this point, i.e., $n_1 = N_{cond}$. As islands begin to nucleate by impingement of surface monomers with arriving Ge atoms, n_1 begins to deviate from N_{cond} and quickly reaches a peak value, at which the island nucleation rate becomes the same as the rate of n_1 growth by the balance between deposition and desorption. As the rate of island nucleation subsides and the island density, n_x, reaches saturation, n_1 evolves largely independently of n_x, a consequence of the fact that island growth proceeds by direct impingement from the vapor, rather than by surface diffusion of monomers to the islands. In other words, n_1 depends only on the relative arrival and desorption rates and the fraction of the surface area that is not occupied by islands. Finally, for all fluxes considered here, the island density reaches a saturation value at which point no new islands are formed and existing islands are growing (and therefore increasing N_{cond}).

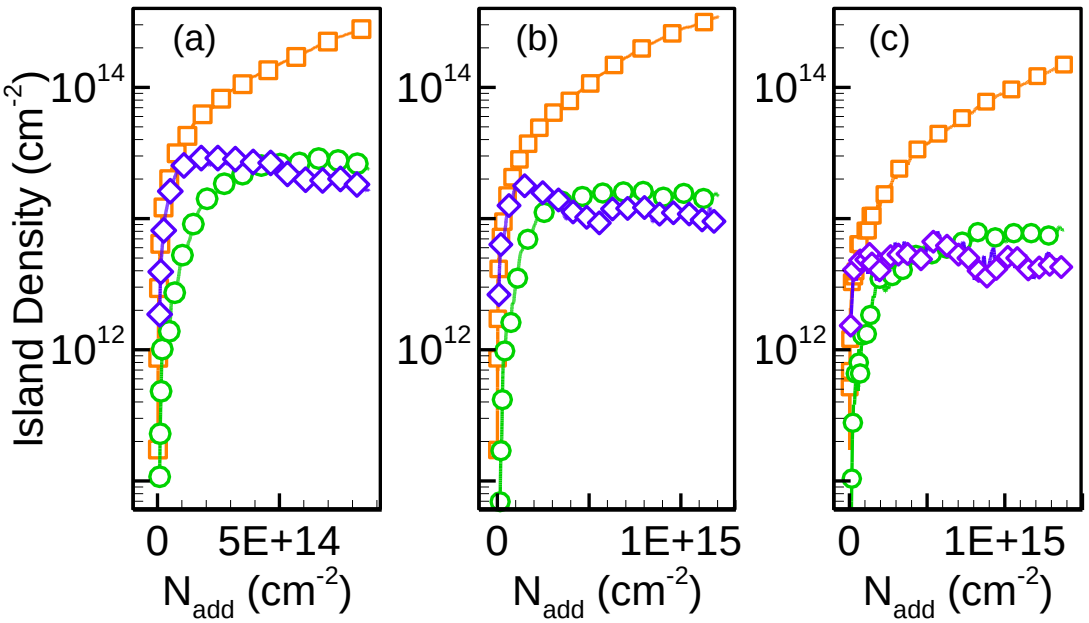

Figure 3.5. Island distribution evolution as a function of time during deposition at 2100K at deposition fluxes of (a) $F = 4.14\times10^{24}$ atoms/cm^{2}s, (b) $F = 6.9\times10^{23}$ atoms/cm^{2}s, and (c) $F = 2.76\times10^{22}$ atoms/cm^{2}s. Data shown includes the total density of Ge condensed on the surface (N_{cond} - orange squares), the density of surface monomers (n_1 - purple diamonds) and the total density of stable clusters (n_x - green circles).

Shown in Figure 3.6 is the evolution of the *integral condensation coefficient*, $\alpha \equiv N_{cond}/N_{add}$, as a function of the number of deposited atoms per unit area at 2200K and various deposition fluxes [129, 130]. Note that the number of deposited atoms is linearly related to deposition time but by a different factor at each flux. For times shorter than the desorption timescale, the integral condensation coefficient is expected to be roughly constant at a value that is dictated by the fraction of surface that is binding. For larger times, desorption from binding sites acts to lower α as seen in Figure 3.6. Finally, as the island coverage fraction increases, α reaches a minimum and eventually begins to rise because adsorbed Ge islands always represent favorable binding environments for incoming Ge atoms. The impact of deposition flux is strong across all

three regimes. Higher fluxes lead to higher initial α and a stronger impact by island coverage at later times.

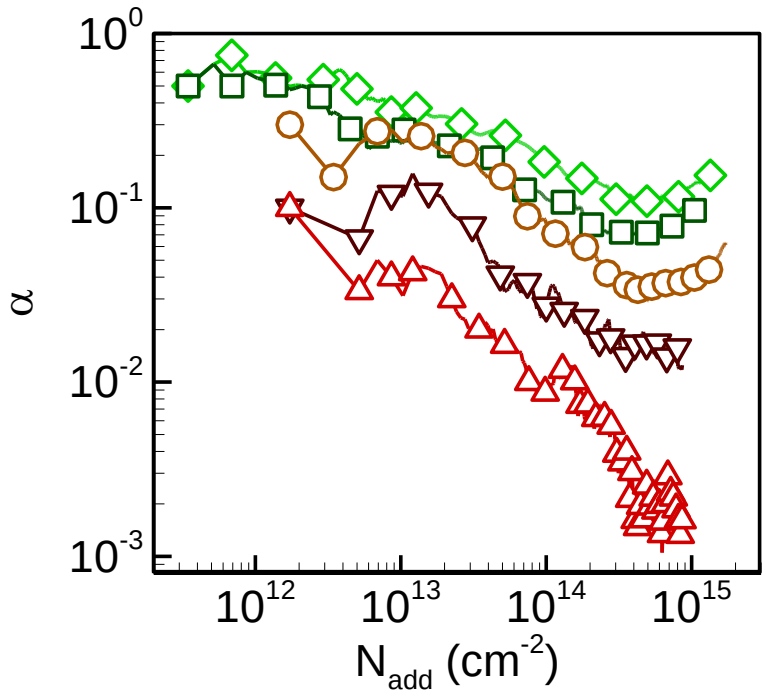

Figure 3.6. Integral condensation coefficient, α, as a function of the number of Ge added to the system per unit area, N_{add}, at 2200K and different fluxes. Green diamonds: $F = 6.9\times10^{23}$ atoms/cm^{2}s, dark green squares: $F = 3.45\times10^{23}$ atoms/cm^{2}s, brown circles: $F = 1.38\times10^{23}$ atoms/cm^{2}s, dark brown gradients: $F = 2.76\times10^{22}$ atoms/cm^{2}s, red deltas: $F = 5\times10^{21}$ atoms/cm^{2}s.

The integral condensation coefficient provides information about the deposition regime; complete condensation corresponds to $\alpha = 1$, while extremely incomplete condensation implies that $\alpha << 1$. Leonhardt et al. [12] concluded that Ge deposition on a-SiO_2 occurs in the extremely incomplete condensation regime. While the growth of islands independently of n_1 in Figure 3.5 suggests that the condensation is extremely incomplete in our simulations, the values of α in Figure 3.6, particularly at early time

and high flux, are as high as 0.4, which is not necessarily indicative of extremely incomplete condensation.

To further characterize the deposition regime in the simulations, we compared the distribution of inter-island distances, X_{island}, with the adatom diffusion distance, X_a, at different deposition fluxes. Inter-island distances were computed on the basis of island centers-of-mass. Islands were approximated to be circular in the *xy*-plane projection and the radius of each island circle was taken to be the distance between the center-of-mass and the furthest atom in the island. The distance between two islands was then calculated as the *xy*-projected distance between the edges of the two circles. Islands were defined as "neighbors" if the line connecting their centers did not cross any areas projected by other islands. Since many Ge islands on the surface deviate strongly from circularity, the circular approximation represents an upper-bound for island radius and the approximated inter-island distances represent lower-bounds.

Shown in Figure 3.7(a) is the mean inter-island distance, $\bar{X}_{island}$, as a function of N_{add} for the same three deposition fluxes considered in Figure 3.5. The value of $\bar{X}_{island}$ decreases as islands nucleate on the surface, then levels off when n_x reaches saturation density. The distance between islands decreases with deposition flux due to the increasing island density, with the lowest value on the order of 10 Å. Taking into account the adatom displacement distribution shown in Figure 3.2 and the probability distributions of X_{island} at the saturation island density found for each deposition flux (Figure 3.7Figure 3.7(b)), the probability of island growth due to adatom migration on the surface is below 1% at high deposition flux, and less than 0.1% for the medium and low flux cases. Because the inter-island distances used here represent lower-bound estimates

for the actual island separations on the surface, these probabilities represent upper-bounds for the actual probability of island growth by surface adatom capture. The low probability of island growth due to surface capture confirms that the system is in the extremely incomplete condensation regime at all deposition fluxes considered in our simulations. Moreover, since adatom displacement does not change significantly with temperature (at least over the range considered here), the condensation regime remains extremely incomplete at all temperatures sampled in this work.

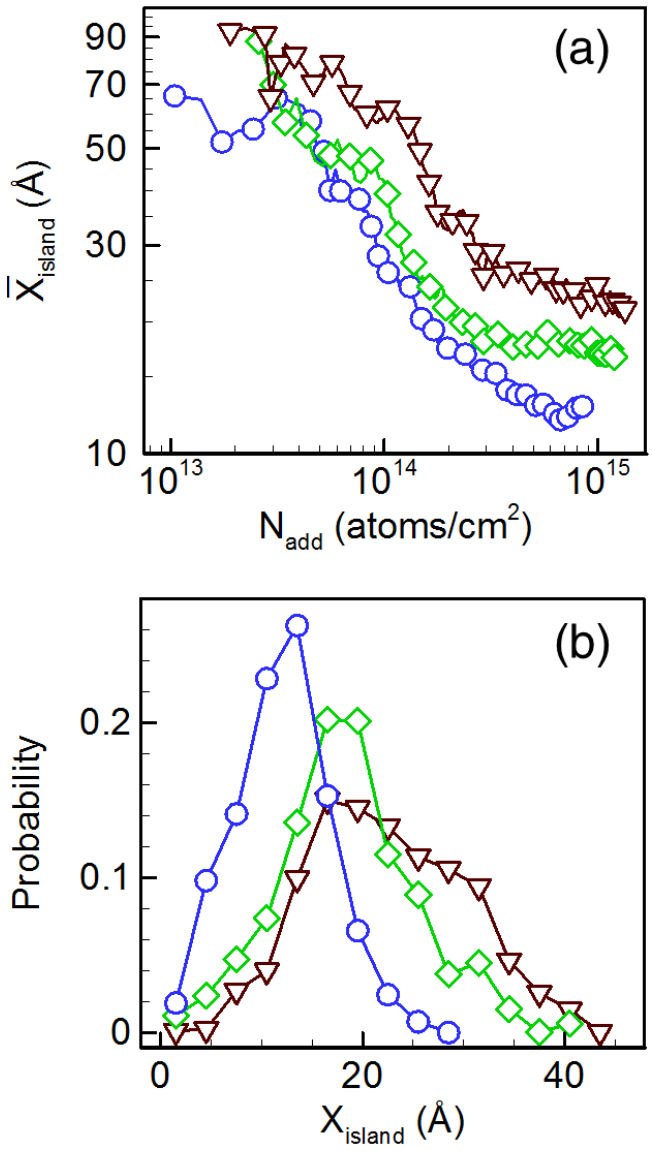

Figure 3.7. (a) Mean inter-island distance as a function of Ge atoms brought down to the surface per unit area at different deposition fluxes and 2100K. Dark brown gradients: F = 2.76×10^{22} atoms/cm^{2}s, green diamonds: F = 6.9×10^{23} atoms/cm^{2}s, blue circles: F = 4.14×10^{24} atoms/cm^{2}s. (b) Probability distributions of the inter-island distance when n_x reaches the saturation island density for the three cases shown in (a). Dark brown gradients: F = 2.76×10^{22} atoms/cm^{2}s at N_{add} = 9×10^{14} atoms/cm^2, green diamonds: F = 6.9×10^{23} atoms/cm^{2}s at N_{add} = 6×10^{14} atoms/cm^2, blue circles: F = 4.14×10^{24} atoms/cm^{2}s at N_{add} = 7×10^{14} atoms/cm^2.

3.6 Scaling Analysis and Quantitative Comparison with Experimental Measurements

While the experimentally-observed condensation regime is qualitatively reproduced in simulations, quantitative measures of the deposition system are needed to make meaningful connections between the computational model and the experiments. As mentioned previously in Section 3.2, the saturation island density, $n_{x,\max}$, can be directly measured in experiments. Recall that in eq. (3.16), $n_{x,\max}$ was found to scale with temperature and the deposition flux according to

$$n_{x,\max} \sim (F)^{\frac{2i}{3}} \exp\left(\frac{E}{k_B T}\right),$$

and $E = \frac{2}{3}\left(E_i + (i+1)E_a - E_d\right)$ in the extremely incomplete condensation regime. Thus, by measuring the saturation island density as a function of temperature, the slope, E/k_B, may be used to deduce the energy barriers relevant for island nucleation. For example, in Ref. [12], saturation island density measurements were used to compute the diffusion activation energy for Ge on a-SiO_2.

Shown in Figure 3.8 are Arrhenius plots of saturation island density versus temperature at several different fluxes ranging from 5×10^{21} atoms/cm^{2}s to 6.9×10^{24} atoms/cm^{2}s. The slope, E/k_B, changes abruptly at 2000K for the three deposition fluxes at which a wide range of temperatures were considered (see Figure 3.8). The change of slope separating the saturation island density into "high" and "low" temperature regimes is in excellent qualitative agreement with similar experimental observations reported by Leonhardt et al. [12]. Establishing a quantitative connection between the simulation and experimental temperature scales is, however, somewhat challenging. It is well-known

that the Tersoff potential significantly overestimates the melting temperature of Si (T_m ~ 2550K) and the usual approach is to introduce a scaling factor, e.g., $T_{m,sim}/T_{m,exp}$, when comparing simulation and experimental results. However, in the present case it is not clear whether the melting temperature of Si or Ge, or the glass transition temperature of a-SiO_2 should be used to establish a scaling factor for the temperature. Given these ambiguities, we refrain from making a direct comparison to the experimental transition temperature reported in ref. [12], which was around 773 K.

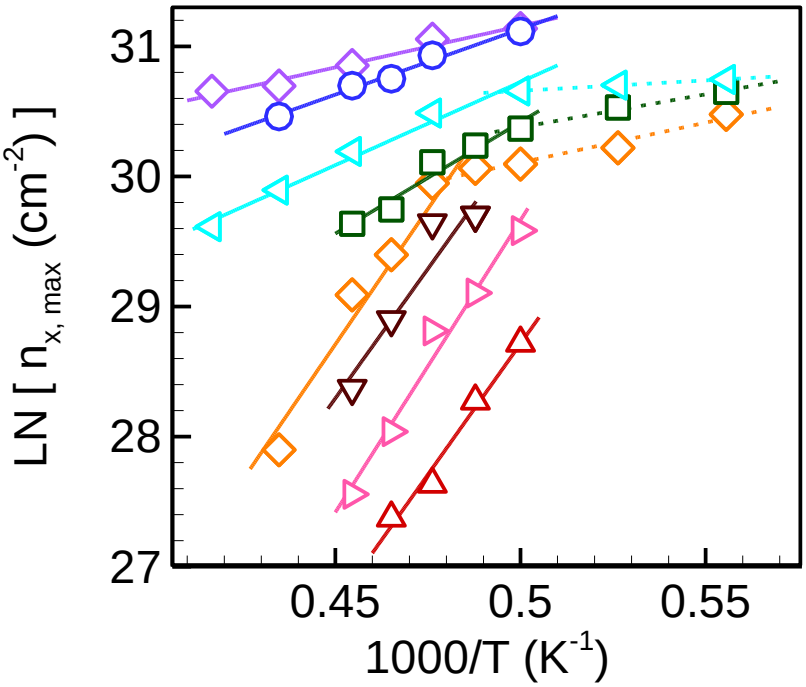

Figure 3.8. Saturation island density as a function of inverse temperature. Purple diamonds: $F = 6.90\times10^{24}$ atoms/cm^{2}s. Blue circles: $F = 4.14\times10^{24}$ atoms/cm^{2}s. Cyan left triangles: $F = 1.38\times10^{24}$ atoms/cm^{2}s. Dark green squares: $F = 3.45\times10^{23}$ atoms/cm^{2}s. Orange diamonds: $F = 6.9\times10^{22}$ atoms/cm^{2}s. Dark brown gradients: $F = 2.76\times10^{22}$ atoms/cm^{2}s. Pink right triangles: $F = 1.38\times10^{22}$ atoms/cm^{2}s. Red deltas: $F = 5\times10^{21}$ atoms/cm^{2}s. Solid lines are linear regression fits in the high temperature regime; dashed lines are linear regression fits in the low temperature regime.

Although the relationship between the Tersoff and experimental temperature scales is unclear, the temperature *dependence* of the saturation island density may be

analyzed more directly. It is immediately obvious that the slopes extracted from both the high and low temperature regimes in Figure 3.8 are strong functions of deposition flux. In the low temperature regime, E/k_B increases from 1600±60K at 1.38×10^{24} atoms/cm^{2}s to 6100±890K at 6.9×10^{22} atom/cm^{2}s, while at high temperature E/k_B rises from 12800±940K at 1.38×10^{24} atoms/cm^{2}s to 34000±5900K at 6.9×10^{22} atom/cm^{2}s. On the other hand, the analysis in ref. [12] suggests that these values are independent of the deposition flux, and are about 5030K and 40400K in the low and high temperature regimes, respectively.

In the following, we focus principally on the high temperature regime ($T \geq$ 2000K) for which we have data over a much larger range of fluxes. Shown in Figure 3.9 is a plot of E/k_B as a function of flux for the high temperature regime. E/k_B rises monotonically as the deposition flux decreases, eventually plateauing at a value that is tantalizingly close to the experimentally reported value (horizontal line); the onset of the plateau appears around a deposition flux of 7×10^{22} atoms/cm^{2}s. While further decreases in deposition flux would have been useful to consider, the slowest deposition run corresponded to introducing one Ge atom every 34.5 ps, and required an MD simulation of 173 ns for a system containing 10^5 atoms, corresponding approximately to 48,000 CPU hours on a modern supercomputer.

The existence of a plateau in E/k_B for $F \leq$ O(10^{22}) atoms/cm^{2}s, along with the excellent prediction of the final value, strongly indicates that for these fluxes, the system has reached a "slow deposition" regime that extends all the way to experimentally realistic fluxes. In other words, for fluxes below O(10^{22}) atoms/cm^{2}s, the deposition timescale is slower than other important timescales that govern island rearrangement (for

example) or desorption. Recall that surface diffusion does not appear to be relevant for this system due to the presence of extremely incomplete condensation conditions and therefore the timescales associated with inter-island diffusion are not likely to be important.

Bearing the above considerations in mind, and assuming that monomer equilibration on the surface is the rate limiting process that competes with the deposition rate, we may then estimate the maximum flux at which the system is still in the "slow deposition" regime. Recalling that the average residence time (between adsorption and desorption) for single Ge monomers was found to be on the order of 10 ps, and requiring that the deposition rate to be lower than the desorption rate, the maximum desorption flux is $O(10^{22})$ atoms/cm^{2}s for the 24 nm by 24 nm a-SiO_2 surface used in this study. This is in excellent agreement with the flux at which the plateau is observed in Figure 3.9!

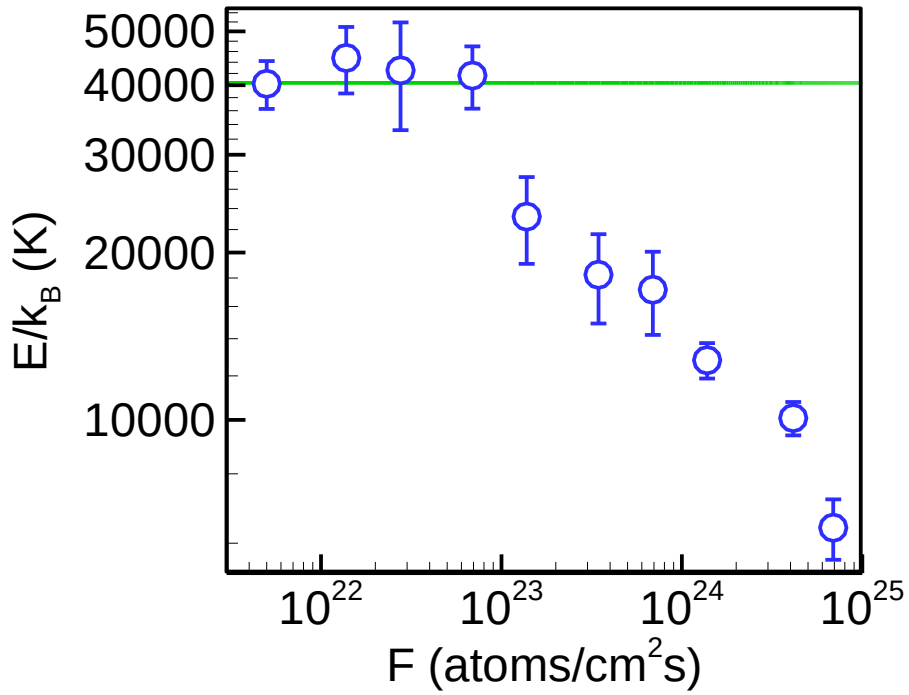

Figure 3.9. Arrhenius slope for saturation island density in the high temperature regime as a function of deposition flux. The solid line represents the value obtained in experiments by Leonhardt et al. [12].

Finally, we return to the issue of critical island size, which has been assumed to be smaller than 2 throughout the preceding analysis, i.e., all islands, including dimers, have been included in the evaluation of n_x. According to eq. (3.16), which applies when the deposition is in the extremely incomplete condensation regime, the saturation island density is related to the deposition flux as $n_x \sim F^{2i/3}$. Shown in Figure 3.10 are log-log plots of the saturation island density as a function of deposition flux at several different temperatures – the slopes of these curves therefore correspond to the quantity $2i/3$. As expected, the slopes, and therefore the critical sizes, are not constant across the entire flux range. However, we do expect that the slope for each temperature reaches a constant value once the slow deposition regime is attained over the last 3 or 4 data points – although this is difficult to ascertain given the scatter in the data and the minimum flux

that can be accessed. Nonetheless, the slope across the 3 – 4 points that correspond to the slowest deposition fluxes at each temperature gives critical sizes in the range of 1 – 2. Importantly, for higher deposition fluxes or at lower temperatures, the critical size estimate is even lower. Collectively, these results self-consistently validate the assumption that the critical size is less than 2. The critical size was also estimated in the experimental analysis in ref. [12] and found to be in the range 2 – 3 in the "high" temperature regime (and 1 – 2 in the "low" temperature regime), again in excellent agreement with the present simulation results.

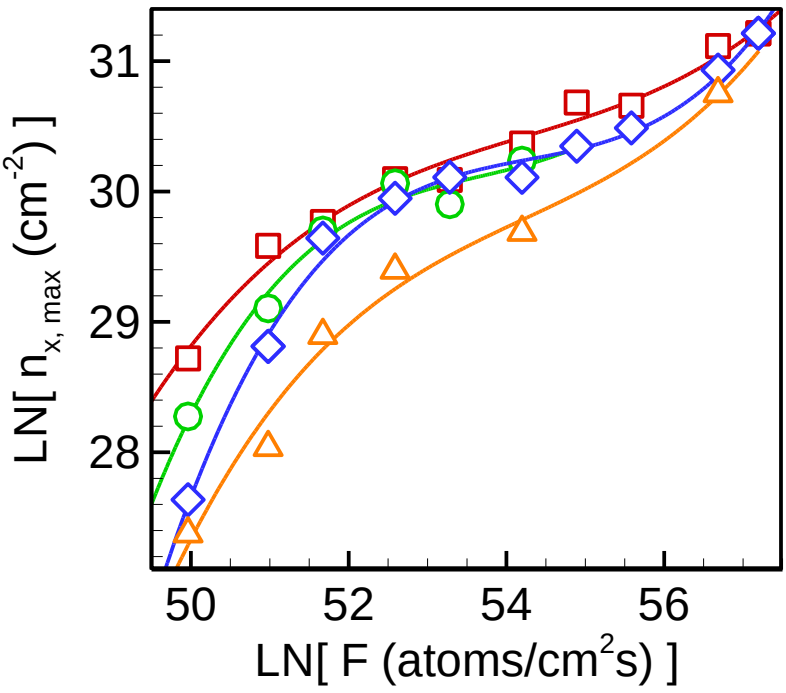

Figure 3.10. Log-log plot of saturation island density versus deposition flux at different temperatures. Lines represent third-order polynomial regression fit. Red squares: 2000K. Green circles: 2050K. Blue diamonds: 2100K. Orange deltas: 2150K.

3.7 Conclusions

The nucleation of Ge islands on amorphous SiO_2 during Ge deposition was investigated with direct MD simulations based on a Tersoff-type empirical interatomic potential model parameterized for the ternary Ge-Si-O system. In accord with prior experimental analysis, the deposition physics, which we probed across a wide range of fluxes and temperatures, were found to be described well by the so-called extremely incomplete condensation regime whereby island growth proceeds by direct impingement from the vapor phase rather than diffusional transport on the surface. These conditions exist because of the nature of the a-SiO_2 surface, which we have previously shown [111] to present a spatially heterogeneous binding energy distribution to Ge atoms. More specifically, the surface exhibits localized binding sites of varying strengths isolated from each other by regions of unfavorable binding, thereby leading very limited Ge monomer mobility on the a-SiO_2 surface and a rather low average barrier for desorption.

Two major conclusions may be drawn from our study. First, and perhaps most importantly, we provide evidence that it is possible to simulate atomic deposition, using straightforward, direct MD simulations, at experimentally meaningful conditions. The timescale restrictions associated with MD simulations of atomic deposition are well-established in the literature and typically require that deposition rates be many orders-of-magnitude higher than experimentally realistic rates. However, by sampling deposition fluxes over a wide enough range (nearly 3 orders-of-magnitude), we found that it is possible to (just) reach a regime where key measures of the deposition process no longer depend on the flux, enabling us to make detailed, quantitative comparisons to experimental measurements. Of course, this may not always be possible in all materials systems, but it does provide strong evidence that realistic deposition rates do not

necessarily have to be achieved in atomistic simulations in order to make quantitative predictions.

Second, and somewhat surprisingly given the complexity of the ternary Ge-Si-O system, we find that predictions of various measures, namely the critical island size and the quantitative temperature dependence, are in excellent agreement with values obtained from experiments. The connection between the simulations and experimental observations of much larger islands formed under much slower deposition conditions was established using a rate equation-based scaling analysis. The rate equation framework first was used to identify the deposition regime under which the experiments were performed, and then to systematically steer the simulations towards it by altering the temperature and deposition flux. Once this was established, the rate equation framework was used to identify quantities that could be compared quantitatively – even though the simulation length, time, and temperature scales are all different than the experimental ones. Collectively, our findings confirm that the empirical potential model for the Ge-Si-O system used here and in our previous study is well-suited for the atomistic study of SEG.

Chapter 4. Coarse Projective Integration for Deposition and Islanding of Ge on Amorphous SiO_2 Surfaces

4.1 Introduction

Atomic deposition, via techniques such as molecular beam epitaxy (MBE) or metal-organic vapor phase epitaxy (MOVPE) of semiconductor species is a critical component of microelectronic [16, 131, 132] and optoelectronic [90, 133-137] device fabrication. It is commonly employed to produce high-quality epitaxial thin films [135, 138-149], and a variety of advanced structures such as quantum wells [150-153], wires [138, 154-156], and dots [132, 138-142, 147].

An atomic deposition process consists of multiple sub-processes that occur over a very wide range of length and time scales spanning orders-of-magnitude. These include atomic diffusion of adsorbate molecules, nucleation, growth and morphological evolution of multi-atom islands, and multilayer-thick film growth. These processes are all intimately coupled so that macroscopic properties of the resulting structure are dictated by the microscopic events [157]. Consequently, improvement of existing processes and development of new ones both require a comprehensive understanding of the various processes that occur and interact during deposition across all time and length scales.

The wide range of relevant length and time scales, however, pose significant computational challenges; a single model that accounts for all macroscopic and microscopic details of the deposition process is generally not feasible [26]. Instead, one often has to make a choice regarding the time and length scales at which the system is resolved, and focus on the processes that are within the selected spatiotemporal domain [99, 131, 157-160]. At the highest resolution are quantum mechanical methods that are primarily used to compute thermodynamic and transport properties, such as binding

energies and diffusion rates for specific events [2, 161]; these are then used as input into coarser methods [2, 162, 163]. Next, are empirical potential molecular dynamics (MD) and Monte Carlo simulations, which are limited to the nano-to-micro regime in both time (s) and length (m) scales [164, 165]. These types of simulation methods may be applied to dynamically study deposition processes, but not at experimentally realistic deposition rates. Several methods to accelerate MD simulation of rare events have been proposed, e.g., hyperdynamics [106, 108] and temperature-accelerated dynamics [105-108], but these methods are somewhat less useful at high temperatures and also require the robust identification of transition events which can be difficult.

A widely-used simulation technique to overcome the timescale limitation in MD is the kinetic Monte Carlo (KMC) method [86-88]. In the most common variant of KMC, a predefined catalog of events is determined and the associated rates are computed. The simulation proceeds by selecting events in a manner that is biased by their rates. The pre-determined event catalog enables KMC to adapt to the timescale of the active processes, although the method can become inefficient when the event database includes a very wide range of rates [166]. This problem may be alleviated by coarse-graining out very fast processes such as atomic vibrations, which are not of direct interest. This coarse-graining is accomplished by reducing the spatial resolution of the model, e.g., by constraining the system to a rigid grid. The on-lattice variant of KMC (or lattice KMC), in which all species are confined to a grid, has been widely used in the simulations of atomic deposition on crystalline substrates [98-100, 166-168].

Finally, we briefly mention continuum models, which have been applied extensively to deposition processes. The most common variants of this approach include rate equations, with and without spatial resolution [159, 160, 169], phase field models

[35, 157, 170], and even hybrid, semi-discrete models that are coarse-grained in the lateral directions and atomistically-resolved in the growth direction [158, 171, 172].

One powerful approach to circumvent the inherent limitations of each of the above techniques is to combine models at different resolutions, either hierarchically or concurrently to generate a multiscale approach [26, 131]. In hierarchical approaches, a finer-scale model, e.g., a quantum calculation, is used to determine certain properties, such as diffusion rates or binding energies. The properties are then used as input parameters to a coarser model such as KMC or a continuum model [16, 19, 173, 174]. In concurrent approaches, the microscopic and macroscopic models are executed simultaneously, exchanging information on the fly. One realization of the concurrent approach is to partition the simulation domain into separate regions that are described by models at different scales [17-20, 175, 176]. This was used in the simulation of epitaxial island growth by Sun et al. [19], in which the evolution of the island is described by a continuum model, and island boundary regions are simulated using a finer-scale lattice KMC model.

Another type of concurrent multiscale simulation approach, known as *coarse projective integration*, or CPI, has recently been suggested by Kevrekidis and coworkers under the general umbrella of 'equation-free' methods [21, 23, 24, 177-180]. The fundamental idea behind equation-free analysis is that many systems that are governed by fast, often stochastic, microprocesses, also exhibit a slowly-evolving manifold defined by some coarse variables. In the case of deposition, such variables may include moments of the island size distribution, or an average surface height. While the values of these variables may be computed at any time from the full (microscopic) system configuration, the closed-form equations that govern their evolution are not known. Thus, short MD

simulations would be used to compute temporal gradients of the coarse variables at given points in time. These numerically-estimated gradients would then be used to evolve differential equations in the coarse variables over time intervals that are large relative to the microprocesses of deposition and adatom diffusion, but small relative to the coarse variable timescales. In other words, CPI is a type of 'equation-free' simulation in which the macroscopic simulator is a numerical time integration scheme [22, 91, 178, 181, 182]; the CPI approach is described in more detail in Section 4.2.

In Ref. [183], Varshney et al. applied the idea of equation-free analysis to examine thin film growth. Using a simplified 1D lattice model, they identified two coarse variables as the variance of the height distribution and the surface roughness. They reconstructed the microscopic system using the island height distribution as well as spatial pair-correlation functions that accounted for lateral interactions among the islands. The reconstructed systems exhibited similar coarse evolution as the direct simulation case [183]. Although generalizing the 1D lattice model to describe 3D island growth requires large numbers of pair-correlation functions, likely making the approach unrealistic, their study demonstrates the applicability of CPI to deposition systems.

Here, we investigate the application of coarse projective integration to the deposition and islanding of Ge on an amorphous SiO_2 (a-SiO_2) surface. We have studied the Ge-on-SiO_2 system previously using direct MD simulation (Chapter 3). There, we found that it was indeed possible to access experimentally relevant deposition conditions [12], but only indirectly via a scaling analysis. Even so, the MD simulations required a large amount of computing resources and the success achieved for this particular system is by no means guaranteed in general. For example, Ge deposition on a-SiO_2 is governed by so-called extremely incomplete condensation, in which surface monomer diffusion is

unimportant and islands grow/shrink by direct impingement/emission rather than (slow) monomer exchange via surface diffusion. In this chapter, we focus on the issue of reconstructing an atomistic configuration only from knowledge of coarse variables such as the island size distribution. We show that this element represents the major challenge in applying CPI to deposition in morphologically complex situations.

The chapter is organized as follows. In Section 4.2 we describe coarse projective integration in detail and present a protocol to reconstruct full microscopic configurations from coarse variable descriptions. The validity of the reconstructed systems based on the island size distributions is analyzed in Section 4.3. A reduced representation of the island size distribution from the coarse variables is discussed in Section 4.4. Finally conclusions are presented in Section 4.5.

4.2 Applying Coarse Projective Integration to the Ge Deposition System

4.2.1 Direct MD Simulation of Ge Deposition

All simulations were based on the Tersoff-based interaction potential we described in Ref. [111], which combined well-established Tersoff parameters for the binary Si-Ge system [14], with a recent parameterization of the binary Si-O system [61] to describe the Ge-Si-O ternary system. As described previously in ref. [111], the ternary potential model, with a single additional fitting parameter for the Ge-O interaction strength, was found to reproduce well a wide range of structural and thermodynamic properties for bulk a-SiO_2, the Si-SiO_2 interface, and Ge adatom binding on a-SiO_2 surfaces. Moreover, direct MD simulations of Ge deposition and islanding were shown to provide quantitative agreement with experimental measurements of various quantities

including the Ge island critical size and the scaling of the saturation island density with temperature (Chapter 3).

All MD simulations were performed using the LAMMPS software package [64]. The temperature and pressure of the system were controlled using the Nose-Hoover thermostat and barostat, respectively [65]. The timestep size was fixed throughout at 1 fs. When necessary, static relaxations (energy minimizations) were performed using the conjugate gradient algorithm in the LAMMPS software. A minimization was considered converged when the change in system potential energy became less than 1×10^{-8} eV, or when the 2-norm of the global force vector of the system was below 0.01 eV/Å.

The a-SiO_2 surfaces used in the analysis were created using a melt-quench procedure to construct bulk a-SiO_2, followed by cleaving the system to produce a free surface, and then extensive thermal annealing to relax it; details of the procedure are provided in Section 3.3.1. Throughout the study, we employed an a-SiO_2 block that is 24 nm × 24 nm in area and 3 nm thick. Periodic boundary conditions were applied in the *x* and *y* directions to simulate an infinite slab in the *xy* plane, while the bottom 1-nm layer of the slab was held fixed throughout the simulation to provide a bulk-like environment. A Ge atom was defined to be an adatom on the a-SiO_2 surface if the distance between the atom and the nearest surface atom (either Si or O) was within the respective interaction cutoff distances, 2.9462 Å for Ge-Si, and 2.49 Å for Ge-O. Ge islands were identified using the Stillinger criterion with a threshold distance equal to the Ge-Ge potential cutoff (3.1 Å) [184].

MD simulations of deposition were performed according to the method described in Section 3.3.2. Briefly, Ge atoms were added to the system at a constant rate that corresponds to a desired deposition flux. For each Ge atom addition, a random position

in the *xy*-plane was generated and the *z*-coordinate was set to be 5 Å above the highest existing atom within 5 Å radius in the *xy*-plane. The Ge particle was assigned a downward velocity corresponding to the system temperature. The system was evolved in the NVT ensemble until the addition of the next Ge particle. Before each Ge addition, checks were performed to remove any desorbed Ge particles from the system in order to prevent the formation of Ge aggregates in the region above the a-SiO_2 substrate.

4.2.2 Coarse Projective Integration

The primary elements of an example coarse projective integration framework are shown in Figure 4.1. Consider a system for which the physics of the fast, microscopic dynamics (top row) are known (e.g., an interaction potential energy model for MD), and which exhibits slowly evolving dynamics on a 'slow manifold' comprised of a set of one or more coarse variables (bottom row). However, the physics governing the dynamics of the coarse variables are either difficult to write down or are unknown.

In the following discussion, we will denote the microscopic description by *x* and the macroscopic description by *X*. We first define an appropriate *lifting* operator, μ, which maps the macroscopic description *X* to a consistent microscopic description *x*. Obviously, this mapping is not uniquely defined because there exist many microscopic configurations that correspond to a given macroscopic state. Conversely, we also define a *restriction* operator, *M*, that maps a microscopic state to a macroscopic description. The CPI algorithm then proceeds as follows: (1) for some initial macroscopic configuration, $X(t_0)$, lift to generate a consistent micro-configuration, $x(t_0)$, (2) evolve the microscopic simulator to obtain $x(t_0 + \Delta t)$ at a later time, (3) restrict to map the microscopic state at the later time to the corresponding macroscopic descriptions. The

preceding 3 steps constitute a coarse time stepper for the macroscopic variables [21, 94]. The next step could be to compute time derivatives of the coarse variables and use them to perform projective integration in time. Clearly, the execution time of the microscopic simulator (Δt) has to be short enough to be computationally practical, yet long enough to enable meaningful gradient evaluation for the coarse variables. Finally, given a new macroscopic initial condition at the end of the projective step, repeat steps 1 to 3.

Note that in Figure 4.1, the initial trajectory of the coarse evolution in the lifted system is shown to be different from the 'correct' trajectory. Such transient deviations are expected to arise from lifting errors, in which details of the micro-configuration that are not captured by coarse variables undergo a 'healing' period. The healing period represents the relaxation of fast processes (that are associated with the omitted micro-configurational details) to the slow manifold described by the coarse variables [23]. Because the system evolution during healing deviates from the correct trajectory, the healing period must not be used to collect gradient evaluation.

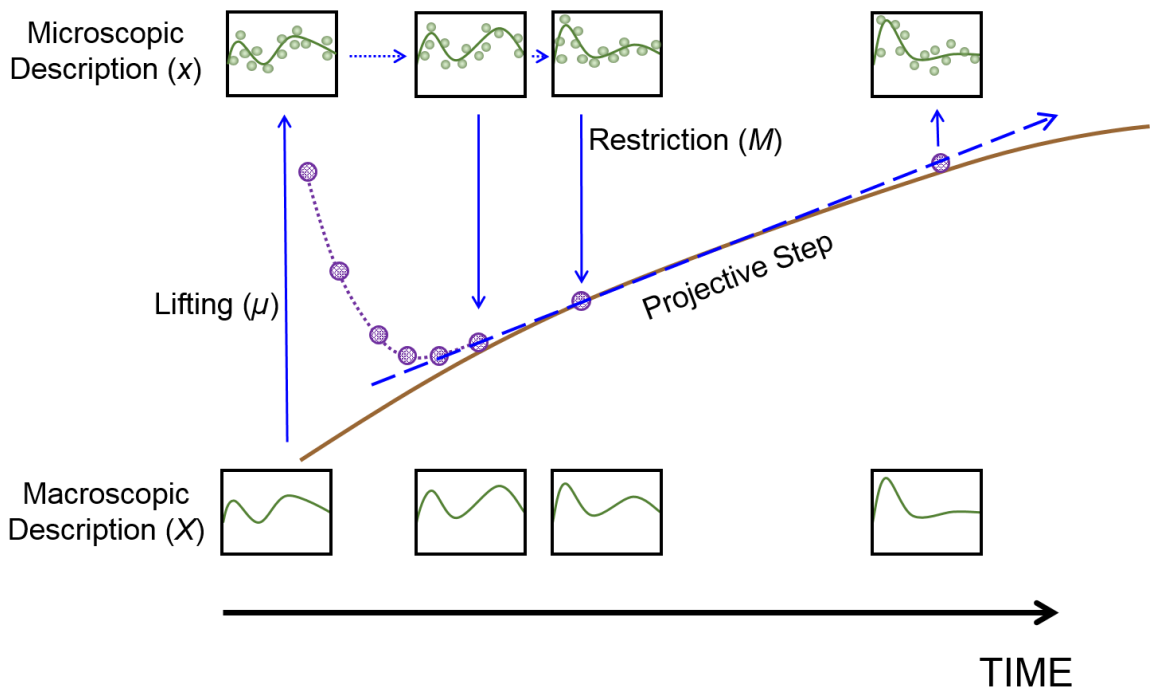

Figure 4.1. A schematic diagram of the coarse projective integration scheme adapted from Ref. [21]. Starting from a given macroscopic representation of the system (X), the corresponding microscopic system (x) is constructed through lifting (μ) and evolved using a microscopic simulator. The results are then mapped to the macroscopic states (M) and projected forward in time using numerical integration. The projected macroscopic system then is lifted again and the process continues.

The success of coarse projective integration is dependent on several important factors related to the identification of appropriate coarse variables. First, coarse variables have to be of sufficiently high fidelity to allow for suitable lifting to consistent micro-configurations. For example, in the case of deposition, the mean height of the surface alone may be inadequate information to lift to a realistic micro-configuration. Simultaneously, the coarse variables must evolve sufficiently rapidly in the microscopic simulator to enable gradient estimation. Generally, variables that include more finely-resolved information, are easier to lift from, but are also subject to more statistical noise making gradient evaluation more difficult. While approaches have been proposed to automatically deduce appropriate coarse variables, including diffusion mapping [93] and

a transfer operator-based numerical scheme [92], there is not yet a systematic way to construct the lifting operator for a wide variety of systems. In fact, as we demonstrate in the remainder of this chapter, the definition of an appropriate lifting operator is the primary challenge for applying CPI to deposition on amorphous substrates.

4.2.3 A Lifting Strategy for Ge-on-aSiO_2 Deposition Simulations

The difficulty in creating a realistic microscopic configuration from a few coarse observables is strongly dependent on the nature of the system under consideration. By definition, the problem is under-determined; the key is to lift to a micro-configuration in which, at most, only the 'unimportant' (fast-relaxing) aspects of the configuration are incorrect.

In addition to these generic issues, the evolution of amorphous Ge islands on an amorphous SiO_2 substrate poses unique challenges. To illustrate these challenges, consider a situation in which the macroscopic observable at some time t, $X(t)$, is the complete island size distribution (ISD), i.e., the number of islands at every size. On one hand, this is a detailed collection of coarse observables, and in fact, it would be quite difficult to estimate derivatives in time for the number of each of the island sizes from microscopic simulations because of stochasticity in these quantities. On the other hand, this information, in many respects, is still insufficient for lifting because of the amorphous nature of the system. First, the morphology of each island at each size is not known, and placing configurationally unrealistic islands on the surface would underestimate their stability. Second, we have shown previously [111] that the a-SiO_2 surface presents a highly heterogeneous binding environment to Ge atoms and clusters.

Again, placing islands at locations that are not energetically favorable will tend to produce unstable islands and an inability to maintain consistency with the slow manifold.

Next, we present a protocol to lift a macroscopic configuration, defined by a given ISD, to an atomistic one. As noted above, a crucial aspect of the lifting procedure for the present situation is the ability to construct realistic amorphous Ge islands. Samples of islands from direct MD simulations of deposition exhibit a rather wide range of island shapes, which alter the island capture zones and may therefore be important in the evolution of the system. To address this, we implemented a database approach in which a library of Ge island configurations was compiled from the direct MD deposition simulations reported in Chapter 3. The MD deposition simulations used to construct the library of Ge island configurations were performed at deposition fluxes of 4.14×10^{24} atoms/cm^{2}s, 1.38×10^{23} atoms/cm^{2}s, 2.76×10^{22} atoms/cm^{2}s, and at temperatures ranging from 2000K to 2200K. At each deposition condition, about 250 snapshots of the system were used to inform the library of island configurations. The procedure was as follows. First, individual Ge islands were identified in a given system snapshot using the Stillinger criterion. For each island, the particle with the lowest *z*-coordinate was set as the origin, and the positions of all other particles were adjusted accordingly to maintain their relative positions. The particle coordinates after adjustment, along with the island size, were recorded in the library of cluster configurations. Overall, the island morphology library contains $O(10^5)$ configurations with island sizes ranging from 2 to 153. Some example configurations taken from the configuration library are shown in Figure 4.2. The islands exhibit a wide range of morphologies, particularly at smaller sizes, and include both compact clusters and long, extended structures. The shapes tend to become more hemi-spherical at larger sizes.

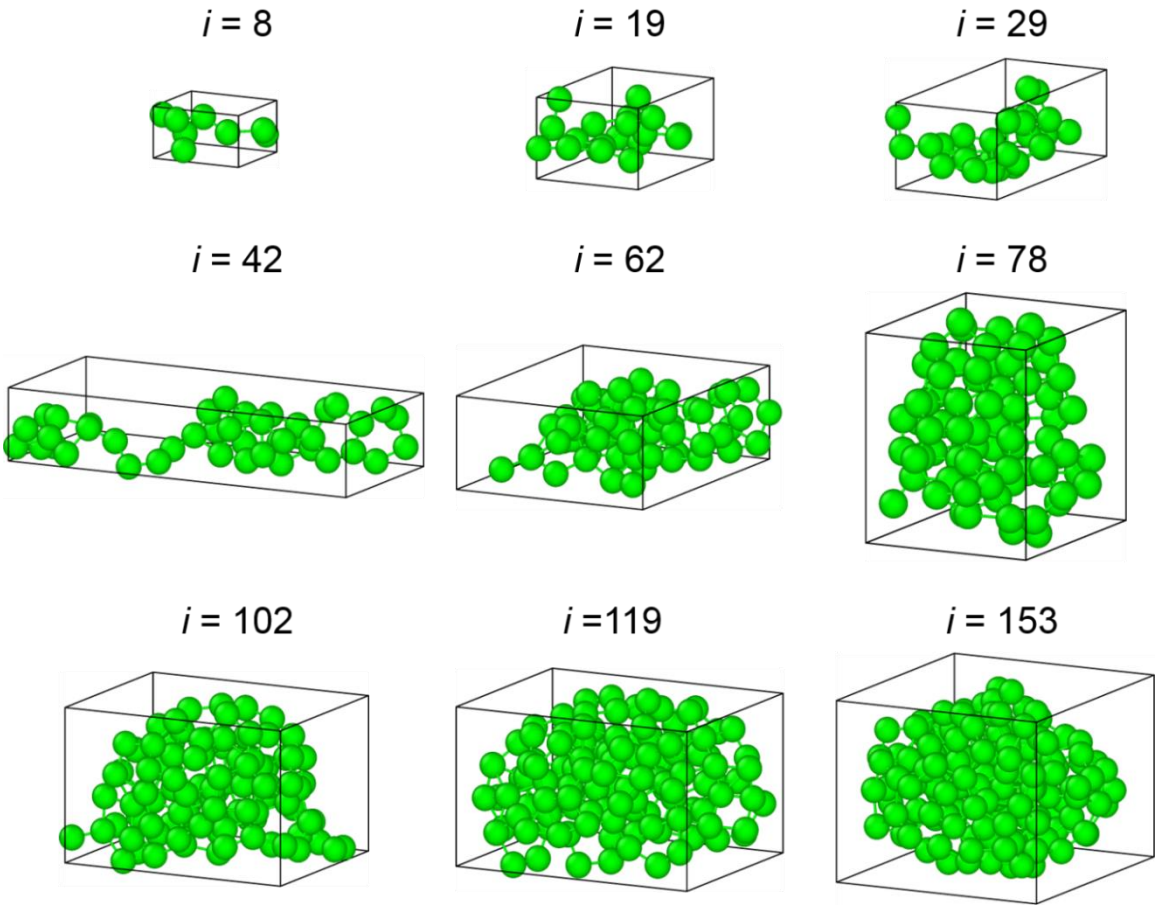

Figure 4.2. Example Ge island morphologies from the library of Ge island configurations collected from direct simulations of Ge deposition on a-SiO_2. Particle rendering (here and in the remainder of this document) performed using the OVITO visualization package [128].

Given a 'target' ISD, the lifting procedure was executed by first randomly selecting Ge island configurations from the library of configurations according to the sizes required by the ISD. For every selected island configuration, the particle with the lowest *z*-coordinate was placed at a randomly generated *xy*-position, (x_i, y_i) over the a-SiO_2 surface. The island size was characterized by computing its maximum lengths along the *x*- and *y*-directions, L_x and L_y, respectively. A rectangular region with area $(L_x+10)\times(L_y+10)$ Å^2 was then centered at the island center-of-mass. The *z*-coordinate

of the lowest atom in the island then was initialized to be 5 Å above the maximum height of the existing atoms inside this rectangular region. The atoms in the island were then assigned a downward velocity corresponding to the system temperature.

The island initialization procedure was repeated for all islands needed to fulfill the target ISD. Island overlapping was prevented by first defining a circular area around each island with diameter equal to the maximum distance between any two atoms in the island. Inter-island spacing was enforced by requiring that each of circular domains be at least 6Å away from any other circular domain. As each island was created sequentially, any conflict with existing islands resulted in a destruction of the island and a resample of the ISD to generate a new one.

The system was subsequently evolved with MD in the NVT ensemble for 0.3 ps, allowing the islands to establish interactions with atoms on the surface. During this procedure, all surface atoms (Si and O particles) remained fixed. Once all islands had made contact with the surface, all surface atoms (except for the ones in the bottom 1 nm layer of the a-SiO_2 substrate) were released. The system then was further relaxed with energy minimization. Finally, the system was subjected to an NVT-MD anneal at the deposition temperature for an additional 2 ps to stabilize the islands on the surface. Due to the strongly heterogeneous binding environment of the a-SiO_2 surface [111], some Ge islands were found to quickly desorb from the surface, moving the ISD away from the target value. If this was the case, additional islands were introduced to replace any islands that desorbed. In this procedure, the newly introduced islands were brought down to the surface using another 0.3 ps-long NVT anneal. Here, only atoms in the new candidate islands were free to move while all other atoms, including those in existing (stable) islands, were kept fixed. The energy minimization and finite temperature

annealing procedure described above was then reapplied to the entire system. The entire process was repeated until no islands desorbed during the relaxation protocol and the ISD matched the target distribution.

4.3 Lifting from the Full Island Size Distribution

The lifting strategy described in the previous section was tested using a reference deposition simulation performed with direct MD. The reference simulation was evolved for 1.75 ns at 2100K at a deposition flux of 6.9×10^{23} atoms/cm^{2}s. The ISDs at 0.375 ns and 0.625 ns were used to lift the system. The configurations from the direct MD simulation at these two time points are shown in Figure 4.3(a) and Figure 4.3(c) respectively. The corresponding lifted configurations, generated using the procedure outlined in the previous section, are shown in Figure 4.3(b) and Figure 4.3(d). The configurations are qualitatively similar. Moreover, the inter-island separation distributions are also quite similar.

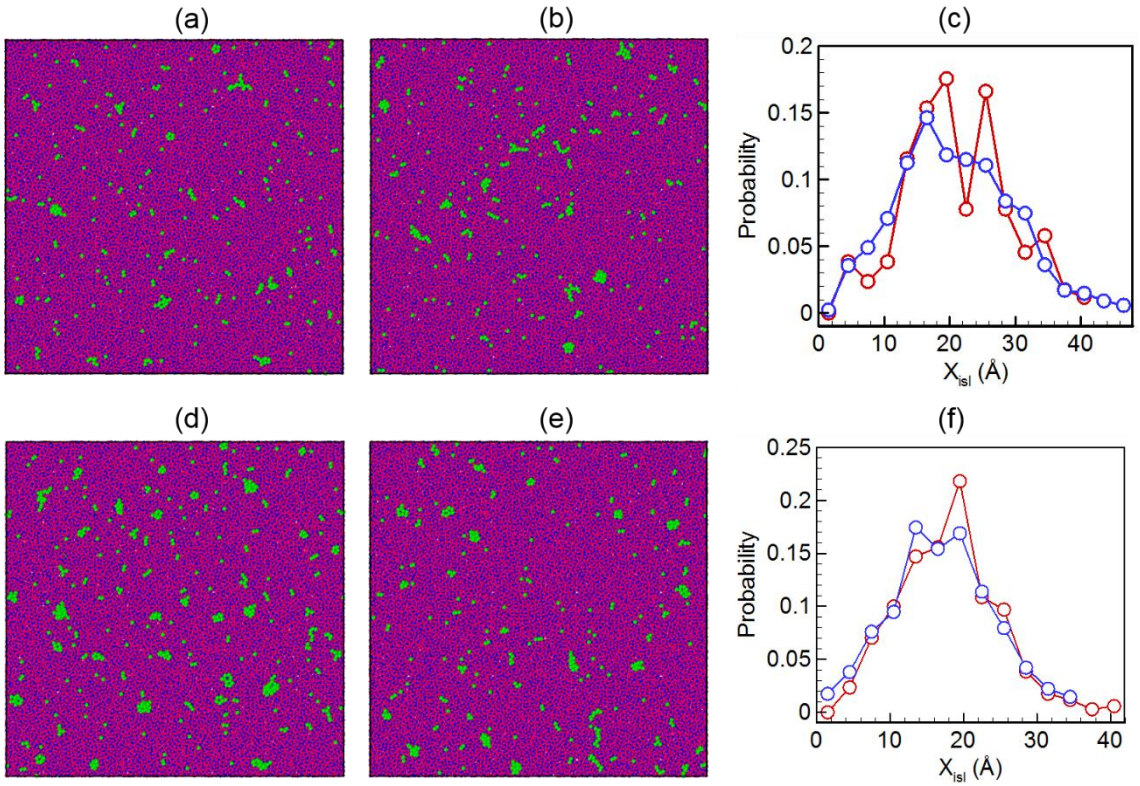

Figure 4.3**.** System configurations from direct MD [a,d], and from lifting using the full island size distribution as the coarse observable [b,e]. The distributions of inter-island separation, X_{isl}, are also computed for the direct MD (red) and lifted (blue) configurations. (a) Direct MD configuration at 0.375 ns, (b) lifted configuration using the island size distribution from (a), (c) inter-island separation distribution for direct MD and lifted configurations at 0.375 ns. (d) direct MD configuration at 0.625 ns, (e) lifted configuration using the island size distribution from (d), (f) inter-island separation distributions for direct MD and lifted configurations at 0.625 ns. In all configurations, red atoms are O, blue atoms are Si, and green atoms are Ge.

Next, we studied how well the MD simulations initialized with the lifted configurations did in comparison to the reference direct MD trajectory. The evolution trajectories in the reference and the test simulation were compared on the basis of moments of the island size distribution. The *k*-th order moment of the ISD, M_k, is defined as

$$M_k = \sum_{i=2}^{i_{max}} i^k n_i \tag{4.1}$$

where i is the cluster size, which ranges from 2 to i_{max}, and n_i is the number density of islands of size i. The moment definition in eq. (4.1) gives the 0^{th}-order moment (M_0) as the total island number density, and the 1^{st}-order moment (M_1) as the total number of monomers contained in all existing islands on the surface. Higher-order moments become progressively more weighted towards larger islands; this point is addressed further below.

The evolution of various ISD moments for the reference and lifted simulations are plotted in Figure 4.4. Each simulation was performed three times with different random number seeds and the trajectories averaged to reduce statistical variations. Overall, the moment trajectories from the lifted systems are in very good agreement with the corresponding reference trajectories. It is noticeable that the trajectories of the lower-order moments (M_0 and to a lesser extent, M_1) exhibit large deviations from the respective reference trajectories shortly after initialization but then eventually recover to join the apparent slow manifold. Note that the low-order moments are more sensitive to small (and fast evolving) species such as dimers and trimers, and therefore also exhibit more noise. The initial healing behavior exhibited by the low-order moment trajectories in the lifted simulations confirms the presence of timescale separation in the system, and justifies the use of CPI for Ge island nucleation and growth on a-SiO_2. The deviations that do exist in the higher-order moment trajectories may be attributed to inadequate coarse observables, e.g., the lack of information regarding inter-island spacing. Moreover we also note that larger islands are present in lower numbers and this may lead to trajectory deviations that require longer times to relax away. In summary, the overall good agreement between the lifted and direct simulation results following the healing phase also suggests that the lifting scheme proposed in Section 4.2.3 was successful.

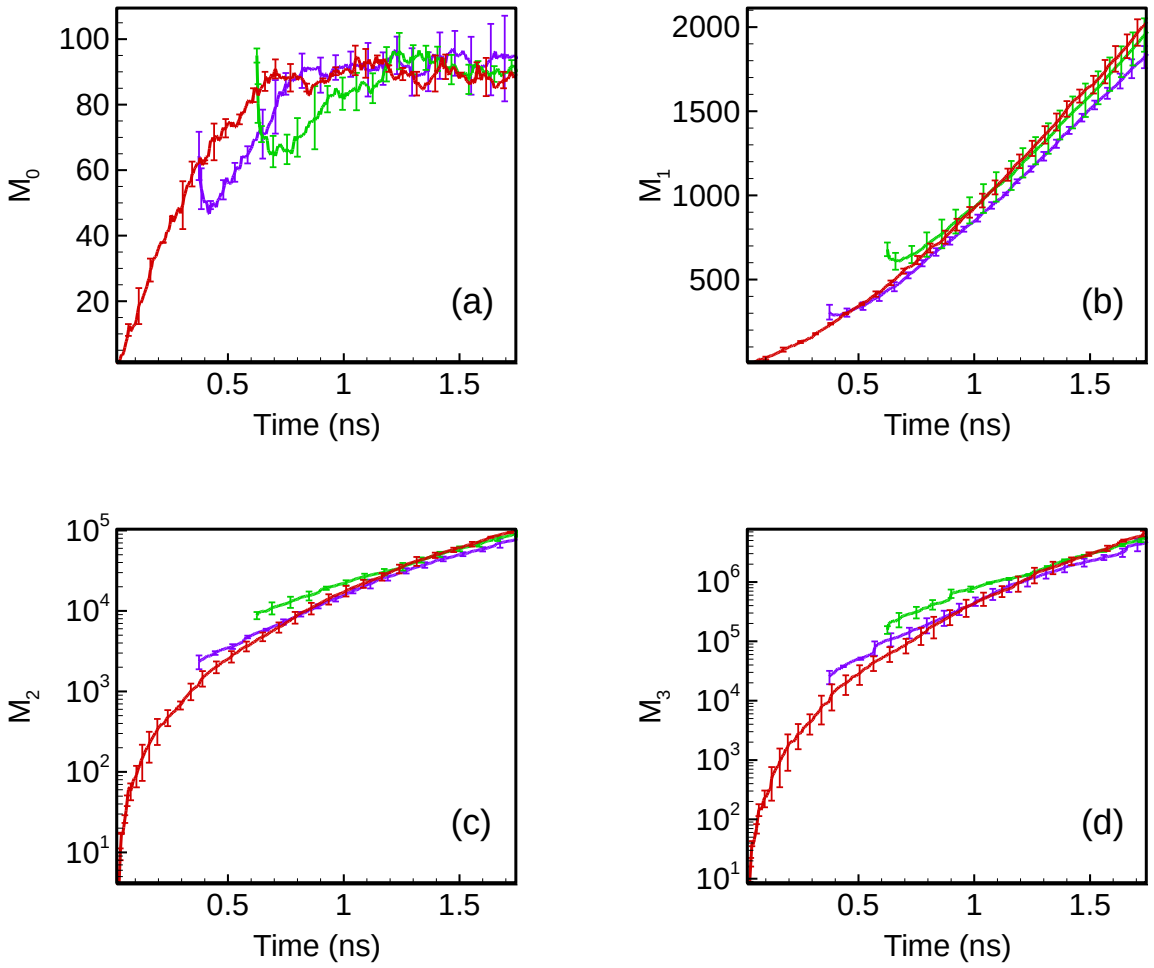

Figure 4.4. (a) – (d) 0^{th} to 3^{rd}-order moments of the island size distributions as a function of simulation time for reference MD (red) and lifted systems at 2100K and a deposition flux of 6.9×10^{23} atoms/cm^{2}s. Purple – system lifted at 0.375 ns; green – system lifted at 0.625 ns.

Although monomers were not included in the moment calculations, it is also interesting to see how the monomer number density, n_1, in the lifted systems evolves as compared to the reference MD simulation. The number density of monomers is obviously linked to the fast processes of adatom adsorption and desorption, and island nucleation. In our previous study of the Ge island nucleation on a-SiO_2 [Chapter 3], n_1

exhibits a peak in the early stages of deposition due to the aforementioned processes. Its long term evolution (prior to island coalescence) is independent of the overall cluster density, a characteristic of the so-called 'extremely-incomplete' condensation regime, whereby island growth does not depend on monomer surface diffusion.

The temporal evolution of n_1 as a function of time for both reference and lifted simulations is plotted in Figure 4.5 for the same simulation systems reported previously in Figure 4.4. In both lifted systems, n_1 initially reaches a peak during healing, then closely follows the results from direct simulation as the fast processes reach steady state. The healing period for n_1 is ~0.5 ns, similar to that for the moments in Figure 4.4, suggesting that the rates for the 'fast processes' responsible for the short-term evolution of n_1 and the low-order moments are faster than $\sim 1\times10^{9}$ s^{-1}. This is of the same order as the rate at which atoms arrive over a region that is comparable to the island length scale (nm).

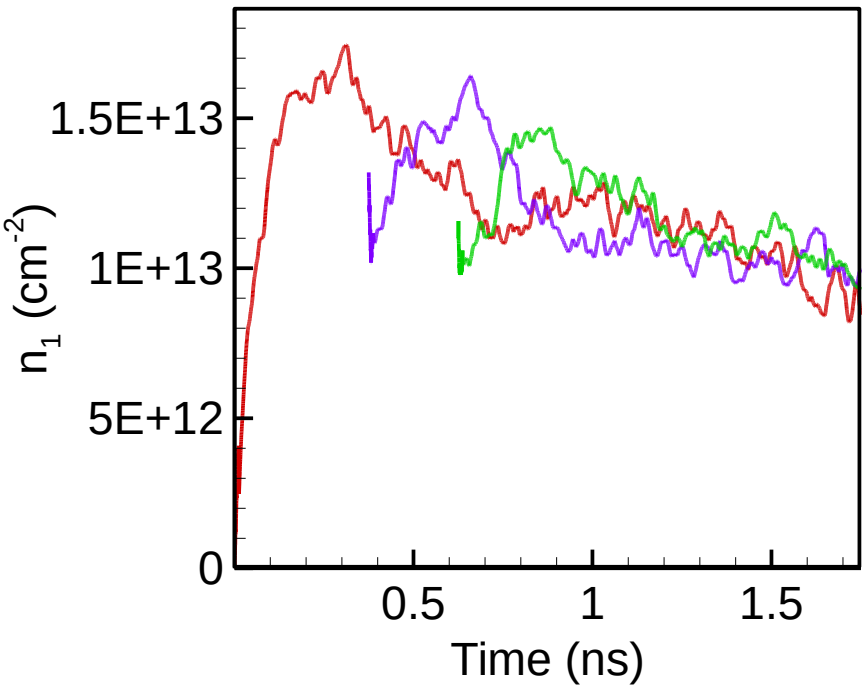

Figure 4.5. Monomer number density (n_1) as a function of time for the direct simulation (red) and lifted systems. Purple – system lifted at 0.375 ns; green – system lifted at 0.625 ns.

The maximum island size, i_{max}, provides yet another measure for island evolution. In contrast to n_1, i_{max} is dictated by the slow, large island processes. The maximum island size, i_{max}, is plotted as a function of time in Figure 4.6 for both the lifted simulations and the direct simulation case. Note that in Chapter 3 we identified the major growth mechanism for Ge islands on a-SiO_2 was the direct impingement of Ge atoms from the vapor, the stochastic nature of the impingement process leads to the large error bars for i_{max} in Figure 4.6. As expected, relaxation of lifting errors in slow processes takes longer than in fast processes: the healing period for i_{max} is more than 1 ns, compared to <0.5 ns for n_1. Moreover, sudden jumps in the values of i_{max} are observed for the lifted systems but are absent in the direct simulations. The sudden increases in i_{max} for these cases was found to be a consequence of coalescence of two nearby islands. Since Ge islands grow mostly by (non-competitive) direct impingement from the vapor instead of surface

monomer capture, the distance distribution between islands is less important, and occasionally placing islands close to each other should not alter the overall evolution of the system. However, as discussed earlier, some improvements can be made to the lifting procedure to reduce the occurrence of the jumps in i_{max}, such as incorporating the average inter-island spacing from the given system configuration instead of the 6 Å minimum inter-island spacing constraint in the current scheme. Overall, the lifted systems, constructed using the procedure outlined in Section 4.2.3 and the full island size distribution, have the same coarse evolution as direct MD simulations in terms of low order moments of the ISD, n_1, and i_{max}.

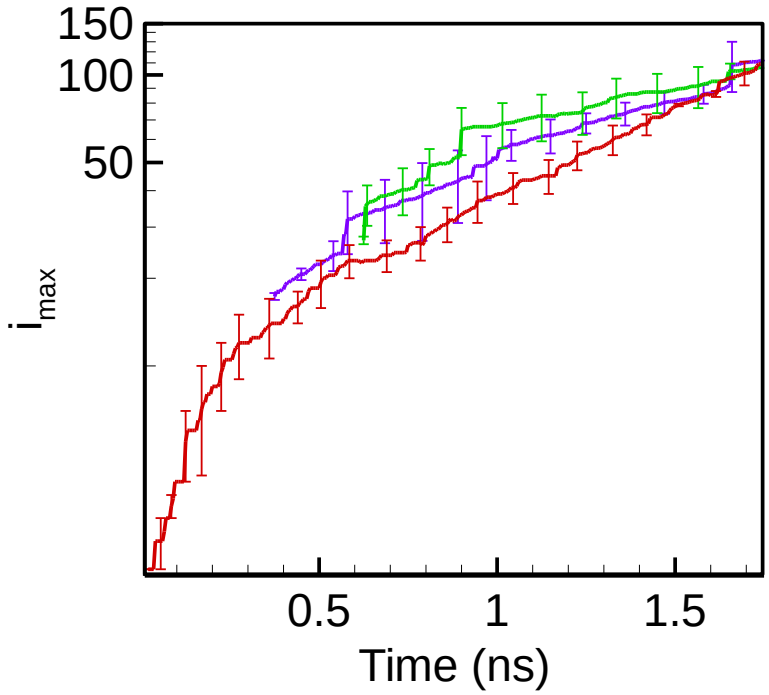

Figure 4.6. Maximum island size, i_{max}, as a function of time for the lifted and direct simulation systems. Red: direct simulations. Purple: system lifted using the ISD at 0.375 ns. Green: lifted system lifted using the ISD at 0.625 ns.

4.4 Lifting from Reduced Representations of the Island Size Distribution

While successful lifting is achieved with the full island size distribution from direct MD simulations, it is an impractical choice for the coarse observable because the number density of each individual size represents a large number of highly stochastic variables. On the other hand, low order moments of the ISD, such as the total number of monomers in islands or the average island size (see Figure 4.4) vary smoothly in time, making them more suitable coarse variable candidates. Here, we extend our original lifting scheme to use only $M_0 - M_3$, n_1, and i_{max} as the input by proposing a procedure to compute a reduced representation of the ISD that resembles the full ISD from direct MD simulations. Some example full ISDs taken at different time points from a direct simulation run are shown in Figure 4.7. In all ISDs, the island number density is high for small sizes and decreases rapidly with the island size, forming a long tail that extends to larger sizes as the system evolves. The majority of the islands are small—more than 50% of the islands are still of sizes less than 15 monomers even at 1.74 ns.

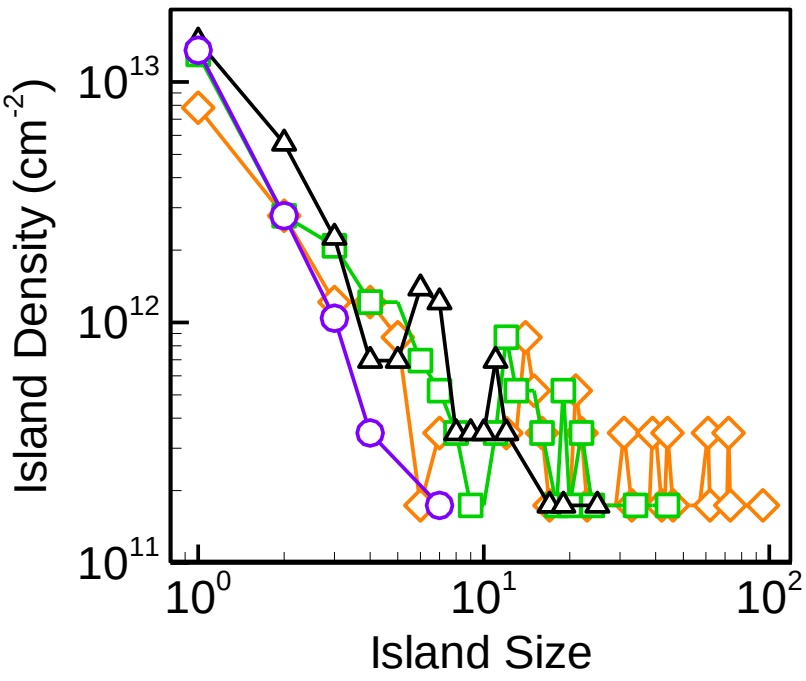

Figure 4.7. Island size distributions at various time points from direct MD simulation of Ge island nucleation on a-SiO_2 at 2100K with a deposition flux of 6.9×10^{23} atoms/cm^2s. Purple circles: 0.125 ns; black deltas: 0.625 ns; green squares: 1 ns; orange diamonds: 1.74 ns.

Recall the definition of moments in eq. (4.1), one can write the following set of linear equations in matrix form:

$$\begin{bmatrix} M_0 \\ M_1 \\ M_2 \\ M_3 \end{bmatrix} = \begin{bmatrix} 2^0 & 3^0 & \cdots & (i_{\max})^0 \\ 2^1 & 3^1 & \cdots & (i_{\max})^1 \\ 2^2 & 3^2 & \cdots & (i_{\max})^2 \\ 2^3 & 3^3 & \cdots & (i_{\max})^3 \end{bmatrix} \begin{bmatrix} n_2 \\ n_3 \\ \vdots \\ n_{i\max} \end{bmatrix}. \tag{4.2}$$

The unknown variables in eq. (4.2) are the density of clusters at each size, n_i, $i \in \{2, i_{\max}\}$, and the known variables are the moments $M_0 - M_3$ and i_{max}. This is an underspecified set of equations which can have an infinite number of solutions that may or may not be meaningful representations of full ISD. To overcome this problem, we divide the range $\{2, i_{max}\}$ into 4 intervals, R_a, R_b, R_c, R_d, where

$$\begin{aligned} R_a &= \{2, q_I\} \\ R_b &= \{q_I + 1, q_{II}\} \\ R_c &= \{q_{II} + 1, q_{III}\} \\ R_d &= \{q_{III} + 1, i_{\max}\} \end{aligned}, \tag{4.3}$$

$2 < q_I < q_{II} < q_{III} < i_{\max}$, and q_I, q_{II}, and q_{III} are island sizes. The average size in each interval is defined as *a*, *b*, *c*, *d*. The sum of cluster densities inside each respective interval is X_a, X_b, X_c, X_d. This formulation characterizes the ISD by 4 coarse bins, so eq. (4.2) can be re-written as

$$\begin{bmatrix} M_0 \\ M_1 \\ M_2 \\ M_3 \end{bmatrix} = \begin{bmatrix} a^0 & b^0 & c^0 & d^0 \\ a^1 & b^1 & c^1 & d^1 \\ a^2 & b^2 & c^2 & d^2 \\ a^3 & b^3 & c^3 & d^3 \end{bmatrix} \begin{bmatrix} X_a \\ X_b \\ X_c \\ X_d \end{bmatrix}, \tag{4.4}$$

which has one unique solution. Since most information of the ISDs is contained in the small size regime (Figure 4.7), the widths of the coarse bins are chosen to be non-uniform, with more emphasis on the lower sizes. Here, we chose the ratio $|R_a| : |R_b| : |R_c| : |R_d| = 1:2:3:4$ as the width of each bin. This assumption determines the values for *a*, *b*, *c*, *d*. Solving eq. (4.4) gives X_a, X_b, X_c, X_d, the sum of island densities inside each coarse bin. Because the island number density decreases with size in the full ISD, we assume the island densities inside each bin scales as i^{-1} to solve for the island number densities, n_i, at each size inside the bin.

Figure 4.8 are the ISDs computed using the above approach (referred to as "reduced ISDs") plotted against the full ISDs at 0.375 ns and 0.625 ns. The reduced ISDs show the same qualitative trends as the full ISDs by design, where the island number densities in the reduced ISDs are high at small sizes and drop rapidly as the island size increases. Note that n_1 is one of the coarse measures to be projected forward

in CPI and an input to the lifting operator, so it is set to the value from direct simulations in the current computation.

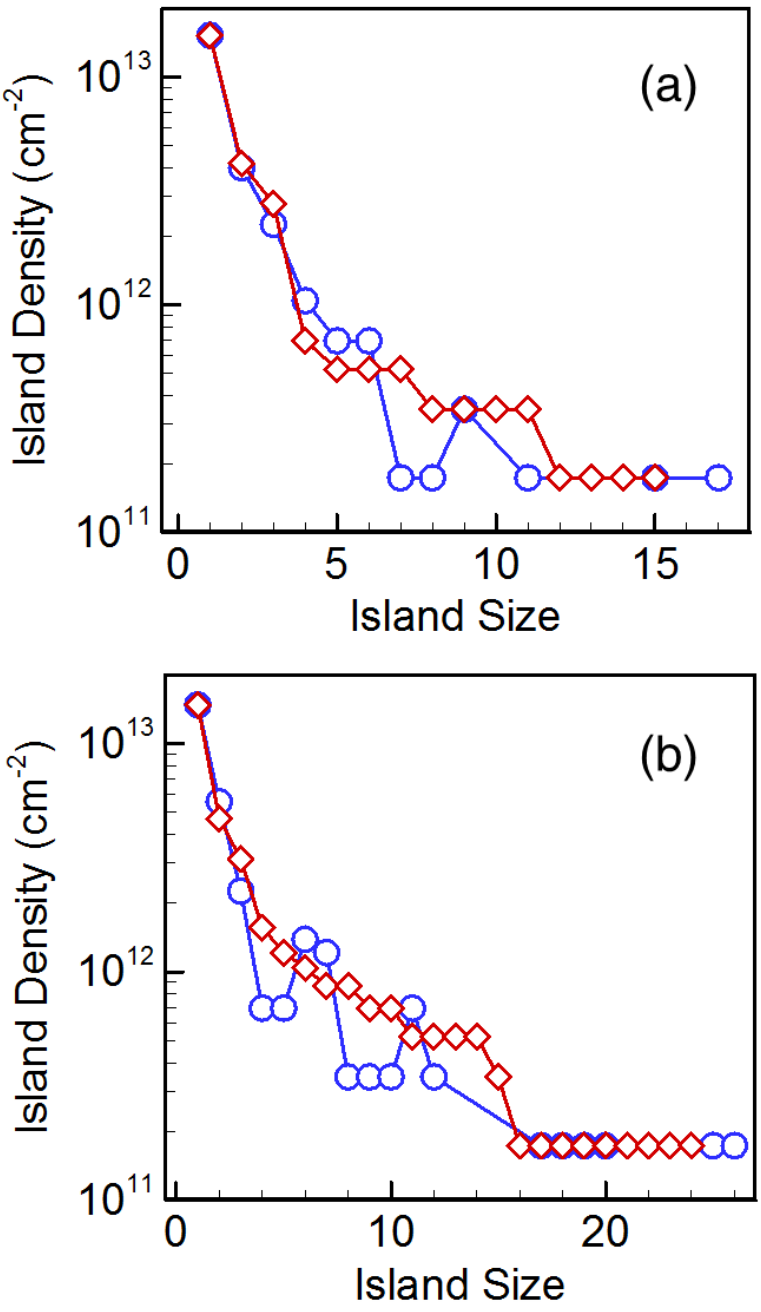

Figure 4.8. Full island size distribution from direct MD (blue circles) and reduced representations (red diamonds) computed from low-order moments of the island size distribution, as well as monomer number density and maximum island size at (a) 0.375 ns and (b) 0.625 ns.

The reduced ISDs shown in Figure 4.8 at time points 0.375 ns and 0.625 ns were used to construct microscopic configurations using the lifting operator presented in Section 4.2.3. Each simulation was performed three times with different random number seeds and the trajectories averaged to reduce statistical variations. The moment trajectories from the lifted systems are shown in Figure 4.9, plotted against the trajectories from direct simulations. Similar to the full ISD case (Figure 4.4), an initial healing period is observed due to lifting errors that are relaxed by the fast processes. The lifted systems exhibit the same coarse evolution as the direct simulations after healing, suggesting that the reduced ISDs are able to correctly reproduce the evolution of the slow manifold, without detailed information of the number density at each island size.

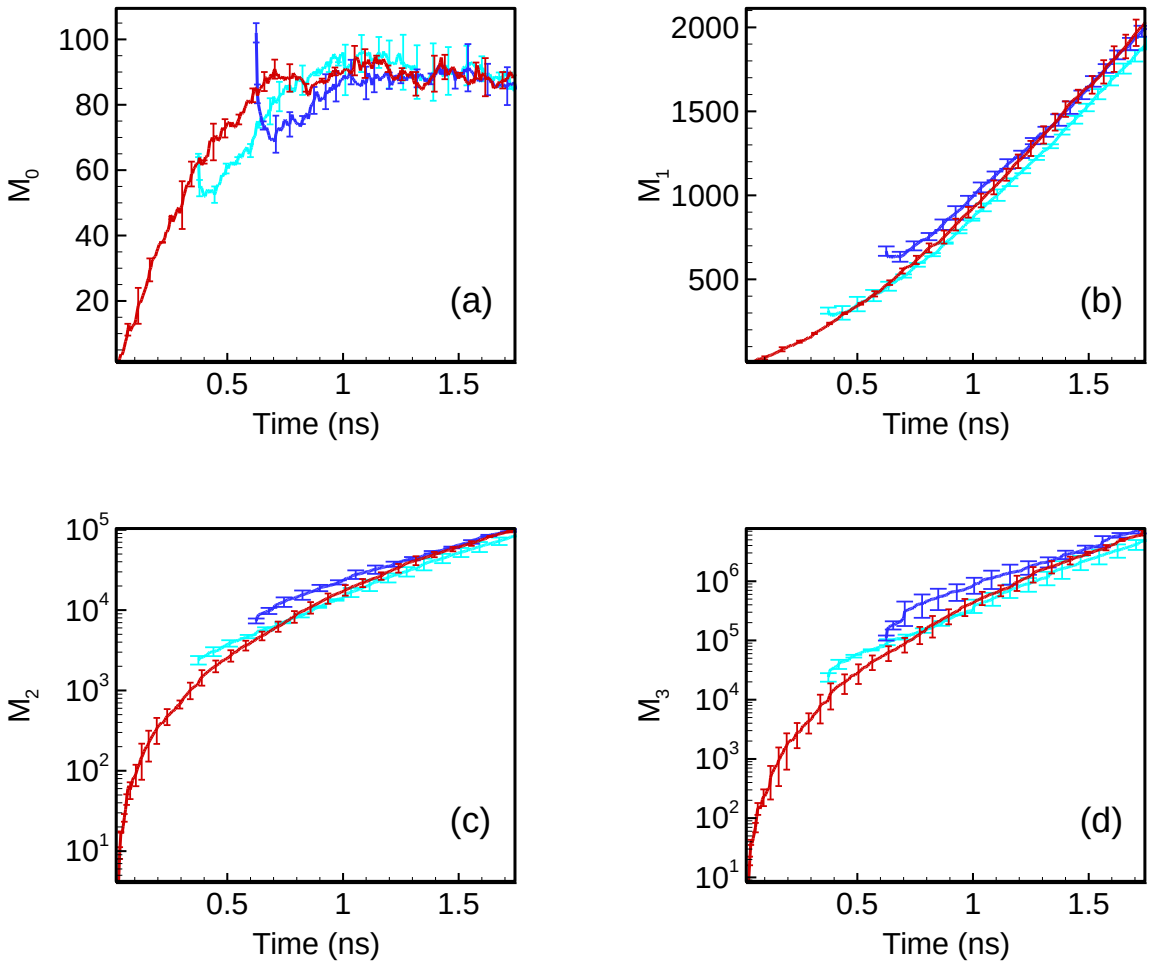

Figure 4.9. (a) – (d) 0^{th} to 3^{rd}-order moments of the island size distributions as a function of simulation time for reference MD (ref) and lifted systems based on reduced ISDs at 2100K and a deposition flux of 6.9×10^{23} atoms/cm^{2}s. Cyan—system lifted at 0.375 ns; blue—system lifted at 0.625 ns.

The percent difference in the low-order moment trajectories shown in Figure 4.4 and Figure 4.9 for the lifted systems based on the full ISD and the reduced ISD, respectively, are compared in Figure 4.10. The percent difference is computed with respect to the reference system, i.e.,

$$\%Differece = \frac{\left(v_L - v_{ref}\right)}{v_{ref}} \times 100\,, \tag{4.5}$$

where v_L and v_{ref} are values from the lifted and direct MD systems, respectively. For all the moments shown in Figure 4.10, the two types of lifted systems exhibit similar coarse evolutions that are within statistical scatter. Therefore one can perform gradient evaluation of the low-order moments based on the reduced ISDs, and the detailed information of the island number density at each size is not required for CPI.

Both lifted systems shown in Figure 4.10 tend to under-predict the values of M_1, M_2, and M_3 after healing. However, since the standard error ranges for the lifted system results are high (data not shown), the values of $M_1 - M_3$ agrees with direct simulation within its standard error range. Even though the statistics can be improved with increasing sample size, the agreement on the low-order moment evolutions between the lifted and the direct simulation systems studied in our work remains unchanged. Our analysis demonstrates that coarse projective integration based on a few measures, namely $M_0 - M_3$, n_1, and i_{max}, is feasible for modeling Ge island growth on a-SiO_2.

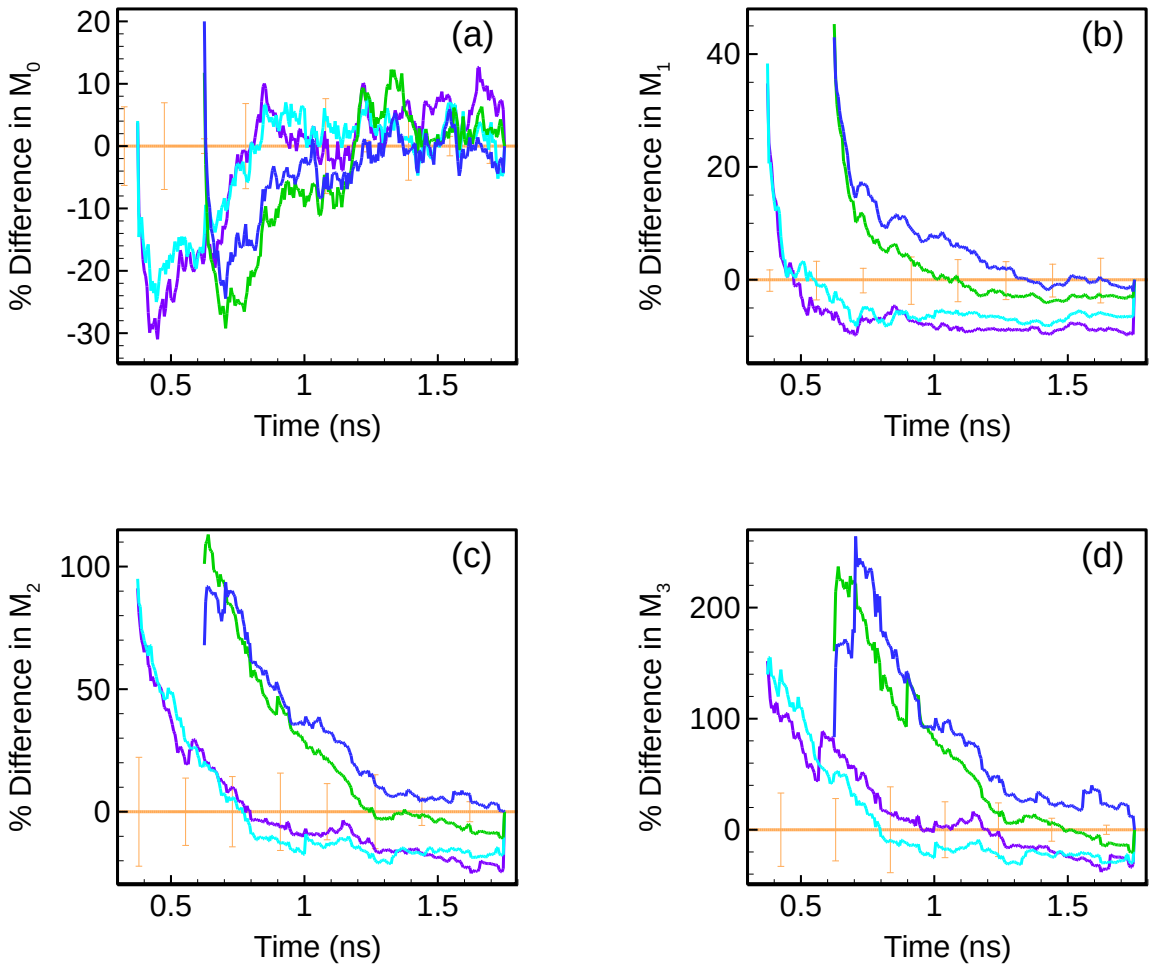

Figure 4.10. Percentage differences in (a) M_0, (b) M_1, (c) M_2, and (d) M_3 with respect to direct simulation results (orange line) for lifted systems based on full and reduced ISDs. Purple: lifted systems based on full ISD at 0.375 ns. Cyan: lifted systems based on reduced ISD at 0.375 ns. Green: lifted systems based on full ISD at 0.625 ns. Blue: lifted systems based on reduced ISD at 0.625 ns. The error bars on the orange line in each panel indicate the range of standard error from direct simulation results.

4.5 Conclusions

The simulation of deposition systems is difficult because the processes involved exhibit a wide range of timescales. While atomistic simulations using empirical interatomic potentials can provide accurate descriptions of the deposition system, it is limited to microscopic timescales. On the other hand, coarse projective integration (CPI) is a type of the equation-free modeling analysis that exploits the separation of timescales

present in many complex systems. The fundamental idea behind equation-free analysis was that many systems that were governed by fast, often stochastic, microprocesses, also exhibited a slowly-evolving manifold defined by some coarse variables. In CPI, short MD simulations are used to compute temporal gradients of the coarse variables at given points in time, which are in turn used to evolve differential equations in the coarse variables over time intervals that are large relative to the microprocesses, but small relative to the coarse variable timescales. It is a promising tool for modeling the deposition system using accurate atomistic simulations while bypassing the limitations on accessible length and time scales. In this chapter, we focused on developing coarse projective integration for deposition systems. Using the Ge on a-SiO_2 deposition system previously studied in Chapter 3 as our reference, our ultimate goal is to address some key issues in applying coarse projective integration to deposition systems, namely the lifting operator.

The lifting operator is a procedure to construct and initialize a detailed microscopic system based only on information of the coarse variables. The amorphous nature of small Ge islands and the highly-heterogeneous binding environment for Ge atoms and clusters presented by the a-SiO_2 surface create unique challenges in lifting. The crucial aspect of the lifting procedure is the ability to construct realistic amorphous Ge islands. The proposed lifting procedure used a collection of Ge island morphologies from previous direct deposition simulations, and place them on the clean a-SiO_2 surface to meet a given size distribution. The islands are stabilized on the surface via series of static relaxations along with short constant temperature NVT-MD anneals. Microscopic configurations were constructed using the lifting procedure based on full island size distributions (ISDs) from direct MD simulations. By using the low-order moments of the

ISD, monomer number density, and maximum island size as our coarse variables, we showed the coarse evolutions of the lifted systems were in agreement with direct MD simulations, thereby validating the proposed lifting scheme. Furthermore, the healing observed in the coarse evolutions of the lifted systems, during which the error introduced in lifting were relaxed by the fast processes, confirmed the presence of timescale separation in the Ge deposition system, justifying the use of CPI. Due to the stochasticity in the full ISDs, we also proposed a method to construct reduced ISDs from the coarse variables mentioned above. The coarse evolutions of the lifted system based on reduced ISDs were also shown to be in excellent agreement with direct simulation, rendering these coarse variables promising candidates to perform CPI.

Despite our study is based on the Ge on a-SiO_2 system, the lifting procedure, the reduced ISD representation, and the possible candidates of coarse variables presented here can be easily adapted for other deposition systems. Overall, our work demonstrated the use of the coarse time-stepper scheme to accurately model the evolution of deposition systems. By the addition of a macroscopic time integrator, the current study can be easily extended to perform coarse projective integration in deposition systems with the use of atomistic simulations.

Chapter 5. Thermodynamic and Morphological Analysis of Large Silicon Self-Interstitial Clusters

5.1 Introduction

Silicon self-interstitials and their aggregates play important roles at various stages of silicon crystal growth and processing. During melt-growth of silicon (via either the Czochralski or float-zone techniques), self-interstitials introduced at the melt-solid interface, as well as those generated in the crystal by Frenkel pair formation, may become supersaturated as the crystal cools. Although the extent of supersaturation depends strongly on the crystal growth conditions, any significant supersaturation will induce self-interstitial clustering. The highly deleterious nature of these self-interstitial clusters requires that most semiconductor silicon has been grown under conditions that are vacancy rich and where self-interstitial supersaturation is not present. However, modern crystals are increasingly grown under conditions of point defect neutrality, where self-interstitials and vacancies are present in near-equal levels, increasing the probability of self-interstitial supersaturation and clustering. In addition to crystal growth, the ion-implantation process, which is used to introduce dopants (e.g. boron or phosphorous) into wafers, also results in strong self-interstitial supersaturation and associated clustering [185, 186]. In addition to potentially directly impacting the crystalline quality of the material, clusters generated by ion-implantation strongly influence the diffusion behavior of implanted dopant atoms during subsequent annealing [187-194].

Predicting the impact of self-interstitial clusters in a particular scenario is best accomplished with a quantitative model for predicting the size and spatial distribution of clusters as a function of process parameters. Typical models are based on a continuum description of the various diffusion, reaction and aggregation processes among point

defects and impurity atoms, most often expressed in terms of systems of partial differential equations. Indeed, such "defect dynamics" models have proven exceptionally useful in a broad range of applications. Perhaps the most successful of these is the prediction of void (vacancy cluster) distributions in both crystal growth and wafer thermal annealing processes [55, 60, 195-198]. Somewhat less success has been realized with the much more complex, but technologically critical, case of oxygen precipitation [199-203].

The input parameters to defect dynamics models include transport (e.g., diffusion coefficients), structural (e.g., capture radii) and thermodynamic properties (formation free energies) for the various atomic species and their clusters. Some of these parameters, namely the diffusivities and formation thermodynamics of single self-interstitials and vacancies, have been studied extensively with both experimental and computational approaches, although even for these very basic properties some uncertainty still remains. Cluster properties are much less well characterized. Small defect clusters, which are critical during the defect nucleation process, are extremely difficult to study experimentally because of their transient nature, their small size, and their relatively low concentrations. Although atomistic simulations are ideal for investigating such small defect clusters, they become progressively more challenging to perform as the number of atoms, and the associated relaxation timescales, increases. These difficulties notwithstanding, the energetics of various vacancy and self-interstitial cluster structures have been computed with both empirical potential and quantum mechanical descriptions. Overall, there is good agreement between the various simulation approaches and the results of these calculations have been used to explain many experimental observations.

However, defect dynamics models require specification of finite temperature *free* energies, rather than energies, which are significantly more difficult to compute. The importance of entropic contributions to cluster thermodynamics was demonstrated previously for the case of vacancy aggregation [55, 60, 204]. Here, both vibrational and configurational entropy were shown to contribute at the elevated temperatures encountered in melt-growth of silicon boules. In particular, configurational entropy, which is often neglected, was found to be surprisingly high and led to substantial reduction of cluster free energies, along with qualitative impact on cluster morphology. Overall, inclusion of cluster entropy was shown to materially improve the predictive capability of defect dynamics models without the *ad hoc* parameter regression that is usually employed to match model predictions to experimental data.

The aim of this chapter is to extend the computational framework described in ref. [204] for vacancy clusters to also address self-interstitial clusters, which, unlike voids, exhibit complex morphological behavior. While the large vacancy aggregates observed experimentally tend to exhibit predominantly octahedral structures bounded by {111}-oriented planes and with 50-200 nm length scales [205, 206], self-interstitial clusters have been observed in a variety of different morphologies that depend sensitively on processing conditions such as thermal annealing time and temperature [188, 189, 191, 193, 207-217].

Detailed summaries of self-interstitial cluster morphologies observed in experiment may be found in prior literature (e.g., [215, 217-219]), and only a brief discussion is provided here. Most large self-interstitial clusters in silicon are planar, and can be classified according to their orientations – those that lie along {113} habit planes ("{113} defects"), and those on {111} planes ("{111} defects") [220-225]. {113}

defects are comprised of <110>-oriented di-interstitial chains aligned in the {113} habit plane [223, 226, 227]. These chains are surrounded on either side by five and seven-membered atom rings, as well as regular six-membered rings. Rod-like {113} defects generally consist of a few <110> chains, while planar ones include a larger number of <110> chains [223, 228]. Interestingly, the spacing between <110> chains is not regular, leading to variable self-interstitial density in {113} defects [228]. The notation /I/, /IO/, /IIO/, etc. represents the presence (I) and absence of (O) <110> chains along the {113} plane in a particular defect. Common {111}-oriented planar defects include the Frank partial (FDL) and the perfect dislocation loops (PDL) [207-209]. Both defects are surrounded by dislocation loops ([111]-oriented Burgers vector for FDLs and [110]-oriented for PDLs). FDLs also exhibit an extrinsic stacking-fault comprised of two additional (111) planes of atoms. {111} defects are the most energetically stable interstitial-related defects and are generally the only remaining species following extended annealing of post-implanted wafers [215]. A third type of {111} defect is also sometimes observed and is comprised of <110>-oriented interstitial chains surrounded by alternating five and eight-membered atomic rings [221, 222]. Finally, smaller clusters tend to exist as compact, three-dimensional entities, but except in the case of certain "magic" sizes (e.g., N_i = 4, 8 [229-231]), their precise structures are not well characterized.

The structures described above have been largely observed and studied in ion-implanted wafers. By contrast, the interstitial aggregates observed in as-grown interstitial-rich silicon crystals tend to be observed in two primary modes, traditionally referred to as "A" and "B" defects [232]. The smaller B defects, which are observed at lower self-interstitial concentrations, are thought to be globular structures similar to the

compact structures found in ion-implanted material [215]. The large A defects are networks of dislocation loops that can reaches sizes of 10s of microns. Presumably, the differences between clusters observed in ion-implantation and crystal growth are due to differences in the nucleation and growth conditions. The very high supersaturation attained in the ion-implantation/wafer annealing case leads to high nucleation rates and, coupled with self-interstitial outdiffusion to the wafer surface, more controlled growth conditions. In crystal growth, the self-interstitial clustering process leads to fewer nuclei that can grow to much larger (and morphologically complicated) sizes.

5.2 Theoretical Background of the Inherent Structure Landscape Analysis

The "conventional" strategy for computing defect formation free energies is to identify the minimum energy configuration and compute its formation energy and vibrational entropy. Configurational entropy is often neglected but may be included by estimating the symmetry degeneracy for the minimum energy configuration. The implicit assumption in this approach is that no other configurations of the defect exist sufficiently energetically close to the ground state to contribute significantly to the free energy. However, as shown previously [204] for vacancy clusters in silicon described by the Environment-Dependent Interatomic Potential (EDIP) [38], configurational entropy may be quite significant for defects at the high temperatures relevant to crystal growth and some wafer annealing processes. This configurational entropy is a consequence of a large number of mechanically stable, off-lattice configurations corresponding to local minima in the potential energy landscape (PEL).

Here, we use the same computational approach used in refs. [204, 219, 233, 234] to compute absolute self-interstitial cluster free energies as a function of size and

temperature. The approach is based on an inherent structure landscape (ISL) description [217, 235-242]. Inherent structures, as first introduced by Stillinger and Weber [235, 243], correspond to local minima in the 3N-dimensional potential energy (or enthalpy) landscape defined by the three-dimensional coordinates of an N-atom system [244]. Each local minimum is surrounded by a basin that defines the region of phase space from which a local minimum is always reached upon downhill energy minimization (e.g. steepest descent or conjugate-gradient) [236]. Under certain conditions, and most often in the solid state, the relevant phase space of the system is well approximated by the collection of basins surrounding inherent structures, i.e. the ISL becomes a good approximation to the PEL.

The ISL framework used in this work has been described in detail in refs. [204, 219, 233, 234] and only a brief development is given here. The PEL→ISL approximation essentially reduces the original potential energy landscape, $E\left(\mathbf{r}^N\right)$, into a collection of basins (inherent structures), α, each of which is identified by its minimum potential energy, E_α. For the configurational portion of the canonical partition function, the approximation is given by

$$Q = \int \exp\left(-\beta E(\mathbf{r}^N)\right) d\mathbf{r}^N \sim \int g\left(E_\alpha\right) \exp\left(-\beta E_\alpha\right) \exp\left(-\beta F_{vib}^{\alpha}\left(\beta\right)\right) dE_\alpha , \qquad (5.1)$$

where $g\left(E_\alpha\right)$ is the configurational density-of-states (DOS) for inherent structures with energies E_α and is independent of temperature, $\beta = 1/k_B T$. The vibrational free energy of a basin, $F_{vib} = -TS_{vib}(T)$, represents the (temperature dependent) number of vibrational "states" in each basin, i.e., $S_{vib} \equiv k \ln N_{vib}$. Note that in eq. (5.1) it is implicitly assumed that inherent structures with similar energies possess similar vibrational characteristics.

A (temperature dependent) modified configurational DOS that includes the vibrational states in each basin then may be defined as

$$G(\beta, E_\alpha) \equiv g(E_\alpha) \exp\left(-\beta F_{vib}^{\alpha}(\beta)\right). \tag{5.2}$$

Noting that the Helmholtz free energy is related to the total partition function, *Z*, as $F = -(1/\beta)\ln Z$, a free energy difference may be expressed using eq. (5.1)

$$\Delta F = -(1/\beta)\ln \int G(\Delta E) \exp\left(-\beta \Delta E\right) d(\Delta E), \tag{5.3}$$

where ΔE is defined relative to the perfect crystal reference state containing the same number of atoms, i.e., $\Delta E = E_\alpha - E_{ref}(N / N_{ref})$. In eq. (5.3), the modified DOS written in terms of the energy difference is independent of temperature

$$G(\Delta E) \equiv \frac{G(E_\alpha)}{G(E_{ref})} = \frac{g(E_\alpha)\exp\left(-\beta F_{vib}^{\alpha}(\beta)\right)}{g(E_{ref})\exp\left(-\beta F_{vib}^{ref}(\beta)\right)} = g(\Delta E)\exp\left(-\beta \Delta F_{vib}\right), \tag{5.4}$$

where $g(E_{ref}) = 1$ was applied in the second equality. The temperature independence of the last exponential term in eq. (5.4) may be demonstrated by considering the vibrational entropy of a given basin within the harmonic approximation, which is given by

$$S_{vib}(\beta) = k \ln\left(\prod_{q}^{3(N-1)} \left(\beta h \nu_q\right)\right), \tag{5.5}$$

where $\{\nu_q\}$ are the normal modes, and noting that the temperature dependence cancels in the expression

$$-\beta \Delta F_{vib} = \frac{1}{k_B}\Delta S_{vib} \equiv \frac{1}{k_B}\left(S_{vib}^{\alpha}(\beta) - S_{vib}^{ref}(\beta)\right). \tag{5.6}$$

5.3 Sampling of the Inherent Structure Landscape

The ISL for each self-interstitial cluster was sampled according to the following procedure. First, a perfect Si lattice was created and N_i self-interstitials were added at adjacent tetragonal sites to create a spherical cluster; the host system sizes used for the various clusters are summarized in Table 5.1. In each case, the system was equilibrated with NPT-ensemble MD for 1 ns in order to determine the average zero pressure volume, followed by a further 0.1 ns in the NVT ensemble. Following this equilibration phase, the system configuration was recorded every 0.2 ps and subjected to conjugate gradient energy minimization at constant volume in order to find the minimum energy of the current basin. The convergence criterion for the minimizations was set to $\|F\|_2 < 10^{-2}$, where $\|F\|_2$ is the 2-norm of the force vector. Note that the minimization procedure leads to the development of significant tensile stress which impacts the energy. Moreover, the precise amount of tension generated during minimization depends on the specific configuration. Formation energies for each inherent structure were computed by referencing the energy to a perfect crystal configuration at the same hydrostatic tension.

Table 5.1. Host system sizes employed for different cluster sizes (N_i).

Number of interstitials (N_i)	Host System Size
$N_i \leq 2$	512
$2 < N_i \leq 8$	1000
$8 < N_i \leq 13$	1728
$13 < N_i \leq 20$	2744
$20 < N_i \leq 35$	4096
$35 < N_i \leq 70$	5832
$N_i = 150$	13824

For each minimized configuration, the cluster configuration was assessed for intactness – only intact cluster configurations were included in the ensuing analysis and configurations that corresponded to broken up clusters were discarded. Intact clusters were identified by first tagging all atoms with energy values that differ by more than 1% from the atomic energy in a perfect lattice that was quenched at constant volume to 0K from the same temperature as the defect-containing simulation. Then, a Stillinger criterion [184] cutoff of 1.8 times the first nearest-neighbor distance in the perfect lattice (2.38Å) was used to determine whether all tagged atoms were connected or not. Note that an atomic displacement criterion may equivalently be used for the purpose of assessing cluster intactness. The atomic displacement criterion identifies all atoms that are displaced from their ideal lattice positions by more than a certain threshold using a perfect crystal reference lattice at the same total volume as the snapshot containing the cluster. As described later, the displacement criterion is used to generate snapshots of cluster configurations and also to probe the geometry of cluster capture zones in Section

5.8, but the atomic energy criterion is simpler to evaluate and provides an equally robust measure of cluster intactness.

All MD simulations and energy minimizations were based on the Erhart-Albe (EA) parameterization of the Tersoff potential[25] and performed using the LAMMPS simulation package. The EA potential represents an improved parametrization of the T3 Tersoff model and provides excellent prediction of elastic coefficients of the diamond phase and various metrics in the liquid. Our choice of potential is also motivated by further studies (not reported here) in which the impact of carbon on self-interstitial clusters is assessed, for which the EA potential has also proven well-suited. However, some limitations in its application to self-interstitial defects are apparent[25] – these are addressed in Section 5.7. Temperature and pressure were controlled with a Nose-Hoover thermostat and barostat, respectively. The MD time step was set to 1 fs in all cases.

A canonical ensemble MD (or Monte Carlo) simulation executed at a temperature T_{sim} samples a PEL so that the probability of being in a basin with minimum energy ΔE is

$$P(\Delta E, \beta_{sim}) \sim G(\Delta E)\exp(-\beta_{sim}\Delta E). \tag{5.7}$$

Probability distribution functions (PDFs) of basin minimum energies were constructed by histogramming the basin minimum energies into bins of width 0.2 eV. For each PDF, multiple MD simulations with different initialization seeds were used to collect O(10^4) IS samples. The temperature-independent modified DOS, $G(\Delta E)$, may then be determined from eq. (5.7) up to an unknown multiplicative constant that must be evaluated separately (see below). Note that at a given simulation temperature and for finite simulation length, a PDF is statistically converged across a finite range of basin

energies and the corresponding modified DOS is valid only over that energy range. For each cluster size, the ISL sampling MD simulations were repeated at multiple temperatures in order to generate a single DOS function that spans the entire energy range of interest. The temperature intervals were selected to provide sufficient overlap between the converged DOS segments, allowing them to be stitched together.

Evaluation of the unknown DOS constant in eq. (5.7) requires that the absolute value of $G(\Delta E)$ be independently specified at one value of ΔE. The lowest energy configuration of each size was used for this purpose because low-lying configurations are typically widely spaced apart and each energy bin usually contains a single configuration. In such a case, the configurational degeneracy of an energy bin is an O(1) number that has relatively little impact on the absolute free energy, even if it cannot be exactly evaluated. The product of this O(1) number and the vibrational degeneracy factor, $\exp(\Delta S_{vib} / k_B)$, then provides the absolute total degeneracy of the reference energy bin. The vibrational entropy for all configurations was computed within the harmonic approximation (eq. (5.5)).

5.4 Replica Exchange Sampling for Large Clusters

For $N_i \geq 30$, self-interstitial clusters exhibit complex morphological behavior in which clusters can assume macroscopically different morphologies, or phases, that are stable at different temperatures. The precise nature of these phases is discussed in detail in the following sections; briefly, planar structures that are relatively low in energy, are preferred at lower temperatures, while globular configurations are stabilized by entropy at higher temperatures. The transition between these distinct morphologies is apparently

difficult, i.e., subject to a significant free energy barrier (that is size dependent), and sampling across this transition in a statistically meaningful manner was found to be impossible in a single MD simulation at a fixed temperature. In fact, for the largest cluster sizes considered in this study, no transitions between the distinct morphological groups could be detected in any of the simulations. Thus, for the temperature ranges over which both morphologies coexist and contribute to the overall free energy, additional methods for enhanced sampling are required.

The replica exchange molecular dynamics (REMD) method [245] was used to sample the ISL at multiple temperatures within the coexistence temperature interval. In REMD, NR copies of the system (replicas) are evolved simultaneously across a range of temperatures, $T_1 < T_2 < ... < T_i < ... < T_{NR}$. The temperature range for each cluster size was selected so that the coexistence regime was contained between the lowest and highest temperatures; see Table 5.2. During the REMD simulation, the system configuration exchanges between adjacent replicas, i and j, are periodically attempted, and accepted with an Boltzmann-weighted probability

$$p = \min\left\{1, \exp\left[\left(\frac{1}{k_B T_j} - \frac{1}{k_B T_i}\right)\left(E_i - E_j\right)\right]\right\}. \tag{5.8}$$

For each cluster size, the system was first equilibrated at an intermediate temperature for 1 ns and then NR replicas of the equilibrated system were created. Exchanges of the configurations among adjacent replica pairs were attempted every 0.1 ps. Configurations from each replica were obtained every 2 ps and minimized in the same fashion as for the standard MD sampling cases.

Table 5.2. Number of replicas and temperature range used in REMD runs for clusters with $N_i \geq 30$.

Cluster size N_i	Number of replicas, NR	Temperature range
30	8	1800K – 1920k
50	8	1880K – 2000K
70	8	1940K – 2050K
150	12	2050K – 2200K

5.5 Small Cluster Probability Distribution Functions

The ISLs of very small self-interstitial clusters already have been studied in some detail using the EDIP potential [217, 219]. Here, we analyze the new EA potential results in the context of the former EDIP results. Like many other parameterizations of the Tersoff model, EA also significantly over-predicts the melting temperature of Si (T_m~2450K vs. 1685K); all reported temperatures in the following discussion are either actual simulation temperatures or dimensionless values scaled by the EA melting temperature. Shown in Figure 5.1 are distributions for three different clusters sizes (N_i = 2, 4, and 10), each collected at two temperatures, $T^* = 0.78$ and $T^* = 0.94$. The 4I cluster exhibits a sharp peak at 10.2 eV that corresponds to the well-known ground state that we have previously termed as the Humble/Arai configuration [217, 219] (Figure 5.1(b))). As described previously this structure is stabilized by large vibrational entropy and competes strongly with a distribution of higher energy configurations which collectively become more important at higher temperature. These results are quantitatively very similar to those obtained previously with the EDIP and Tersoff potentials [217, 219]. Here, and in all configurations shown in subsequent figures, the

atomic displacement criterion is employed to generate configurational snapshots. All atoms that are displaced from their equilibrium positions by more than 0.4 Å are tagged. Of these, the N_i most displaced atoms are arbitrarily assigned as self-interstitials (large red spheres) and the remainder are labelled by small green spheres.

The larger 10I cluster exhibits a broader distribution of energies which is bimodal at lower temperature and singly peaked at higher temperature. The high temperature distribution is peaked at configurations that are three-dimensional and highly disordered. The two peaks in the lower temperature distribution correspond to a bifurcation in the cluster morphology. The higher energy peak consists of three dimensional disordered cluster configurations, while the lower energy one represents configurationally well-defined precursors (Figure 5.1(c)) to various planar species at larger sizes [217, 219].

Qualitatively, the small cluster observations are consistent with our prior EDIP results, although the EDIP potential predicted a stronger skew towards the disordered configurations and only exhibited the disordered configurations at all temperatures considered [217, 219]; this is attributed to particularly high EDIP energy landscape roughness that corresponds to a large number of competing inherent structures. However, in refs. [217, 219] it was demonstrated that the application of tensile hydrostatic pressure to the system increased the importance of similar planar precursors, also leading to bimodal distributions similar to those observed in the present study and also with the "T3" parameterization of the Tersoff potential [14, 41]. The mechanism for this response to tension was shown to proceed via reduction of ISL roughness, i.e., a reduction in the number of mechanically stable, high energy configurations (and their collective configurational entropy). Although not shown here, the response of the EA

PEL to applied pressure is similar to that of EDIP (and T3 Tersoff) – hydrostatic tension reduces landscape roughness, while compression increases it.

In summary, the current EA results indicate that the EA PEL for small self-interstitial clusters is generally similar to those predicted by other empirical potentials for silicon such as T3 Tersoff, Stillinger-Weber, and EDIP but that some differences in the landscape roughness are apparent. Overall, the EDIP PEL appears to be especially rough relative to other potentials, favoring higher-energy three-dimensional amorphous configurations over the ground state.

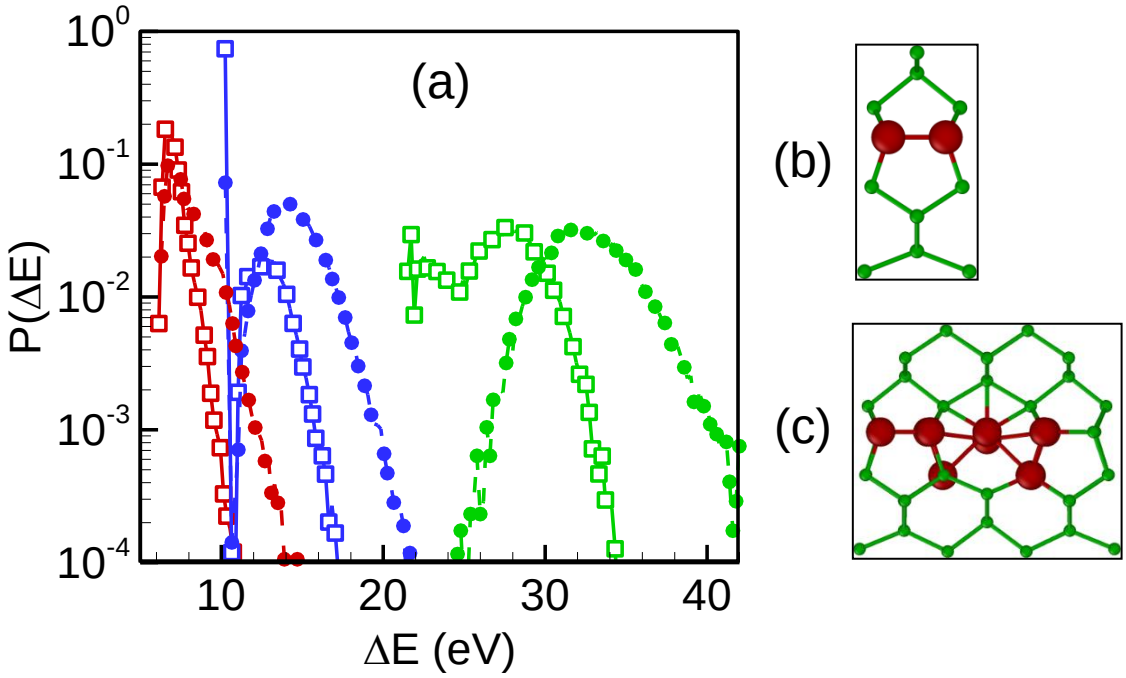

Figure 5.1. (a) PDFs for small clusters: red curves – 2I, blue curves – 4I, and green curves – 10I. For each case, open symbols correspond to T=1900K, solid symbols to T=2300K. (b) Ground state 4I configuration corresponding to Humble/Arai structure ($\Delta E = 10.2$ eV). (c) Ground state 10I configuration comprised of side-by-side Humble/Arai units surrounding an eight-membered ring ($\Delta E = 22.3$ eV). Large red spheres denote N_i most displaced atoms, small green spheres denote other atoms that are displaced by more than 0.4 A from their ideal positions.

5.6 Large Cluster Probability Distribution Functions

The inherent structure probability distributions for larger clusters are much broader than the small cluster ones and exhibit a clear separation between various types of planar configurations ("plates") and three-dimensional, amorphous configurations ("blobs"). These two morphological classes may be considered as distinct phases separated by a low probability region along the formation energy axis. This low-probability region in between the plate and blob phases corresponds to a free energy barrier (with height that is inversely related to the probability) for the transition between the two phases. As discussed in Section 5.4, replica-exchange MD (REMD) was required to sample the PDFs for these clusters across temperature ranges in which both morphological phases were relevant, i.e., near coexistence.

Shown in Figure 5.2 and Figure 5.3 are inherent structure PDFs for the 70I and 150I clusters, respectively, at 3 different temperatures, along with example configurations for each size. At the lowest temperature, the distributions are peaked at configurations that correspond to various planar configurations, while at higher temperatures, the 3-dimensional blob phase is dominant. The intermediate temperature windows, which for both clusters lie in the range over which REMD simulations were performed, show a very wide range of energy values in which both blob (Figure 5.2(d) and Figure 5.3(d)) and plate (Figure 5.2(b,c) and Figure 5.3 (b,c)) phases coexist. At the lowest temperature (1900K), the 70I cluster exhibits both Frank (FDL – Figure 5.2 (c)) and perfect (PDL – Figure 5.2(b)) dislocation loops with relative probabilities that depend on the temperature – the lower energy PDL becomes dominant as the temperature is lowered. The 150I cluster by contrast only shows PDL structures (Figure 5.3(b)) at the temperatures shown – the broad energy distribution exhibited by planar defects is related to the various ways

in which PDLs can become disorganized (Figure 5.3(c)). For all planar configurations the surrounding displacement field is three-dimensional and extends in the direction normal to the plane of the defect by an amount similar to the diameter of the loops resulting in an approximately spherical zone. This zone of elastic displacement may be correlated with the capture zone of the clusters which is discussed in more detail in Section 5.8.

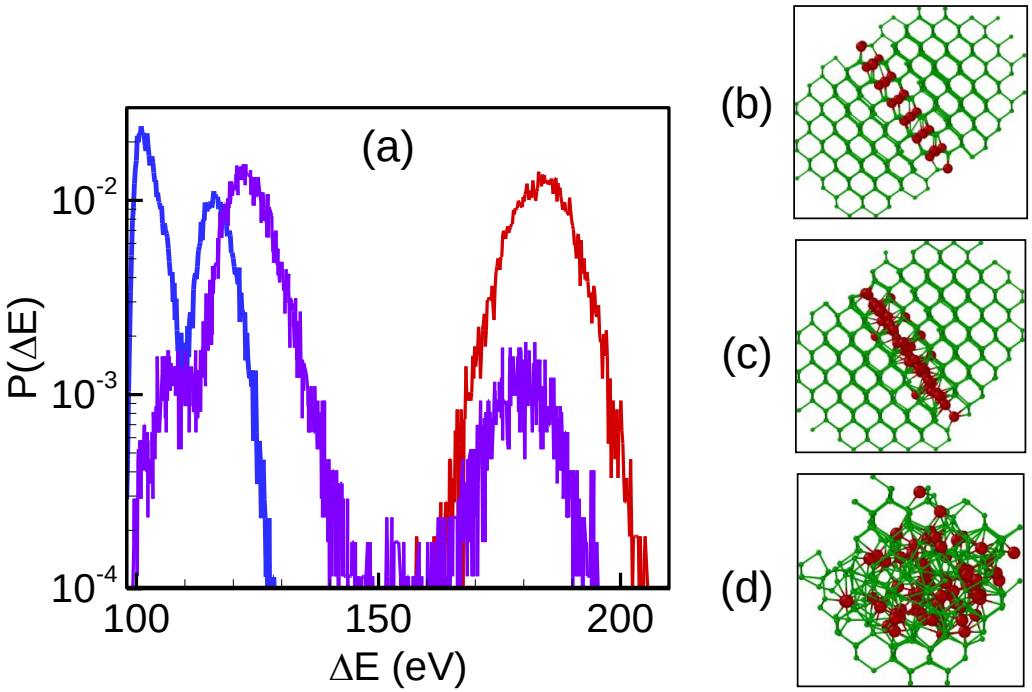

Figure 5.2. (a) 70I inherent structure PDF at 3 temperatures: blue – 1900K, purple – 2050K (from REMD simulation), and red – 2100K. (b) PDL configuration ($\Delta E = 97.4$ eV), (c) FDL configuration ($\Delta E = 120.4$ eV), and (d) blob configuration ($\Delta E = 179.5$ eV). Large red spheres denote N_i most displaced atoms; small green spheres denote other atoms that are displaced more than 0.4 Å from their ideal positions.

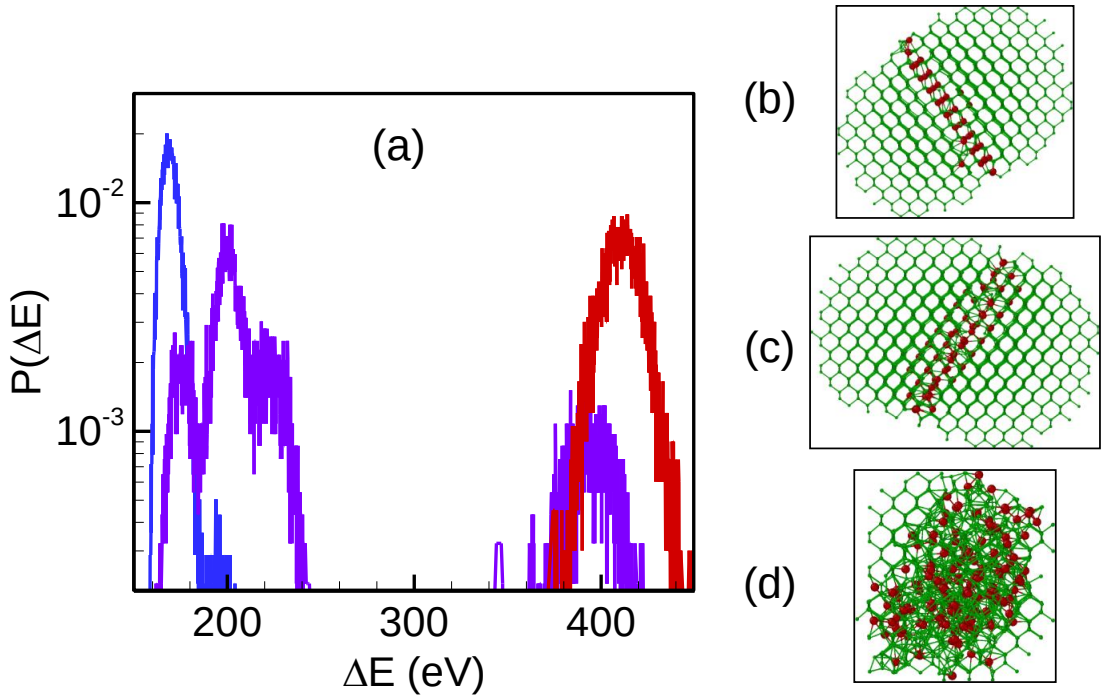

Figure 5.3. (a) 150I inherent structure PDF at 3 temperatures: blue – 2050K, purple – 2144K (from REMD simulation), and red – 2200K. (b) PDL configuration ($\Delta E = 167.9$ eV), (c) PDL configuration ($\Delta E = 197.1$ eV), and (d) blob configuration ($\Delta E = 480.7$ eV). Large red spheres denote N_i most displaced atoms; small green spheres denote other atoms that are displaced more than 0.4 Å from their ideal positions.

5.7 Absolute Density-of-States and Free Energies for Self-interstitial Cluster Inherent Structures

The probability distribution functions described in the preceding sections were used to compute absolute DOS using eq. (5.6) and vibrational entropy calculations for reference states at each size. The vibrational entropies of formation as a function of formation energy are shown in Figure 5.4 for the reference configuration at each cluster size. There is an approximately linear relationship between the formation vibrational entropy and formation energy across the entire size range. This trend is consistent with previous calculations of vibrational entropy as a function of formation energy across multiple configurations of a single cluster for both self-interstitial and vacancy species

[217, 219]. In other words, the linear increase of vibrational entropy with formation energy appears to hold across different cluster sizes of a given point defect species as well as different configurations of a given cluster type and size.

It is notable that the EA potential predicts small but *negative* vibrational entropies of formation for the monomer, dimer, and trimer self-interstitial reference configurations, which correspond to the lowest energy states found for each species. These configurations are comprised of N_i self-interstitials roughly positioned in neighboring tetrahedral sites. It is well established that both T3 Tersoff and EA (erroneously) predict that the tetrahedral configuration is the ground state for the single interstitial rather than the <110> dumbbell [25]. The negative vibrational entropy predicted for the tetrahedral self-interstitial can be interpreted in the context of additional local rigidity provided by the interstitial atom which sits in the middle of a large space within the tetrahedral lattice. The fact that negative vibrational entropies of formation are also predicted for dimers and trimers reflects the fact that these species also exhibit tetrahedral character that provides local rigidity. The predicted EA ground state structures correspond well to energetically low-lying (but not ground state) configurations identified by Ritchie et al. [246] using a combination of tight-binding and DFT. For example, the EA trimer ground state closely resembles the compact configuration identified in ref. [246] that is only 0.13 eV above the DFT ground state, while the EA dimer ground state is similar in nature to the I_2^b configuration in ref. [246] that was found to be 0.4 eV above the DFT energetic minimum configuration.

The significance of these deviations from the DFT results for very small clusters in the context of the present study is not immediately obvious. At first glance, it would

appear that such discrepancies could indicate that the EA (and T3 Tersoff) potentials are unsuitable for studies of self-interstitial clusters. However, it should be noted that clusters containing 4 or more self-interstitials are fundamentally different in nature. For example, the Humble structure that represents the ground state for the 4I cluster, represents a significant reconstruction, and is essentially unrelated to the structures identified for N_i = 1-3 as evidenced by its very large vibrational entropy of formation. This reconstruction is a key element in the formation of building block of larger planar structures such as the {113} defects. The fact the EA potential correctly predicts this structure and gives a good estimate for its formation energy suggests that the impact of the discrepancies identified for very small clusters might be limited. Similar arguments may be made for the FDL and PDL {111} defects, which are examples of yet another type of reconstruction are also correctly predicted by the EA potential.

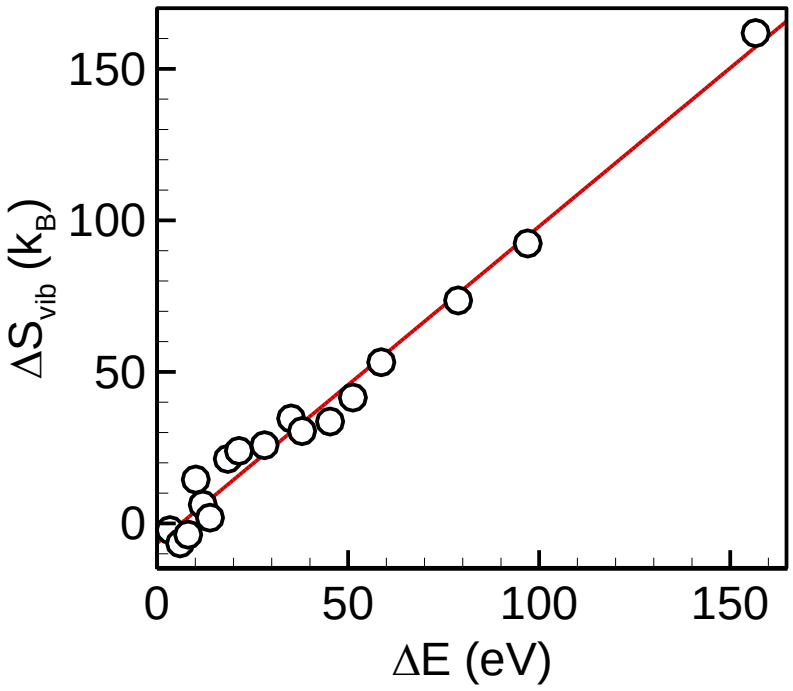

Figure 5.4. Self-interstitial cluster vibrational entropy of formation, eq. (6), as a function of formation energy. Red line is a linear fit.

Example absolute DOS curves for several different cluster sizes are shown in Figure 5.5, where it was assumed that the configurational degeneracy of the reference configuration was unity for all sizes. Recall that the actual configurational degeneracy of any *single* structure is expected to be O(1) (typically dictated by simple symmetry considerations), and the energy bins near the ground state configuration tend to contain very few distinct configurations due to the sparsity of inherent structures with very low energies. By using an energy bin with a single structure as a reference for computing an absolute DOS, and neglecting the degeneracy introduced by lattice symmetry, the free energy of formation for any given cluster size is expected to be overestimated by no more than 0.2-0.5 eV across the temperature range considered in this study. The curves shown in Figure 5.5 represent information obtained at multiple simulation temperatures and are themselves independent of temperature (within the harmonic approximation). The

energy ranges over which each curve is computed reflect the energies that were adequately sampled by the MD simulations at the temperatures considered in this study.

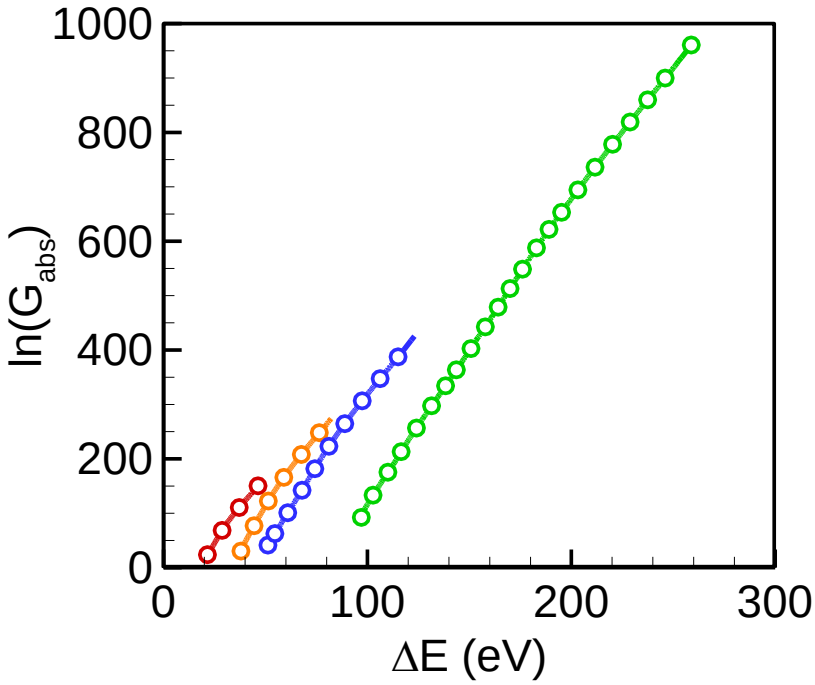

Figure 5.5. Absolute DOS curves for the various cluster sizes. Red – 10I; Orange – 20I; Blue – 30I; Green – 70I. Energy range for each cluster size represents the aggregate of configurations of that size sampled over all simulation temperatures.

The free energy per interstitial as a function of temperature and cluster size is shown in Figure 5.6(a). Generally, the free energy per interstitial decreases with both cluster size and temperature, although significant non-monotonicity exists for small clusters, which has been addressed in detail in prior studies and is not the focus of the present study. In particular, the 4I and 8I clusters exhibit known special stability ("magic sizes") due to particularly favorable configurations that are precursors to {311} and other types of planar defects [230]. The corresponding total formation entropy is shown in

Figure 5.6(b). The total entropy, which includes both vibrational and configurational components was defined as

$$\Delta S(T) = -\frac{1}{T}\left[\Delta F(T) - \int \Delta E \times P(\Delta E, T) d(\Delta E)\right], \tag{5.9}$$

where the integral term represents the weighted average of the cluster formation energy. A sudden increase in total entropy is observed for larger clusters (N_i > 25) above 2100K. The effect increases in strength as the cluster size increases due the increased entropy associated with larger amorphous configurations. The temperature dependence of the cluster entropy suggests that N_i ~ 25 represents a critical size, below which clusters are too small to assume a sufficient diversity of configurations to produce the entropic "explosion" observed for larger ones.

The impact of cluster size on the temperature dependence of cluster thermodynamics is more directly shown in Figure 5.7, which presents line plots for both the free energy and entropy of formation for the 10I and 150I clusters as a function of temperature. The 150I cluster exhibits a sharp increase in the formation entropy (dashed line with diamond symbols) and therefore also in the slope of the energy and free energy (dotted and solid lines, respectively) at around 2100K (~0.85 T_m) at which the configurational entropy contribution to the free energy becomes important. As will be demonstrated in Figure 5.8, this rapid increase in the cluster entropy corresponds to an order-disorder transition from structured, plate-like configurations to amorphous, blob-like configurations. Away from the transition region, the entropy is also observed to increase with temperature, although at a much slower rate. Here, the increase in entropy (both configurational and vibrational) with temperature may be attributed to a gradual

increase in the extent of “microscopic” disorder associated with either the plate or blob macro-configurations.

By contrast, the 10I cluster shows a much more gradual transition region that is spread out over several hundred K and lacks a well-defined morphological transition temperature. This may be interpreted as a confinement effect whereby the small size of the 10I cluster limits its ability to achieve low energy planar configurations, instead producing “precursor” configurations such as the ones shown in Figure 5.7. Transition from these planar precursor configurations to amorphous blob configurations with an increase in temperature is therefore more subtle for the 10I case, leading to more gradual changes in both the entropy and enthalpy. In other words, the reduced state space associated with sub-critical clusters restricts the order-disorder transition exhibited by super-critical clusters ($N_i > 25$).

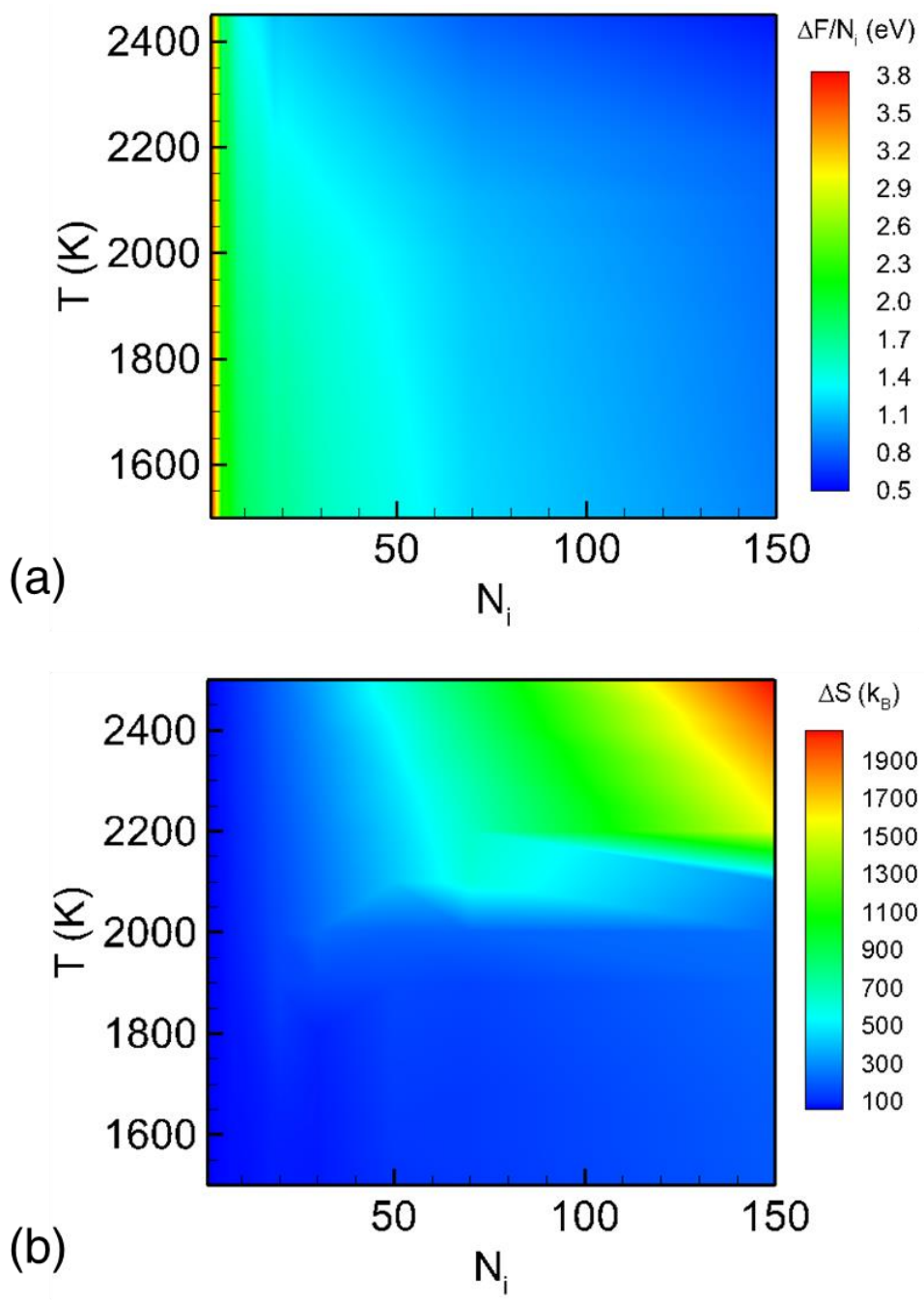

Figure 5.6. (a) Cluster formation free energy per interstitial as a function of temperature and size computed from absolute DOS curves (examples shown in Figure 5.5). (b) Formation entropy as a function of temperature and size computed using eq. (9).

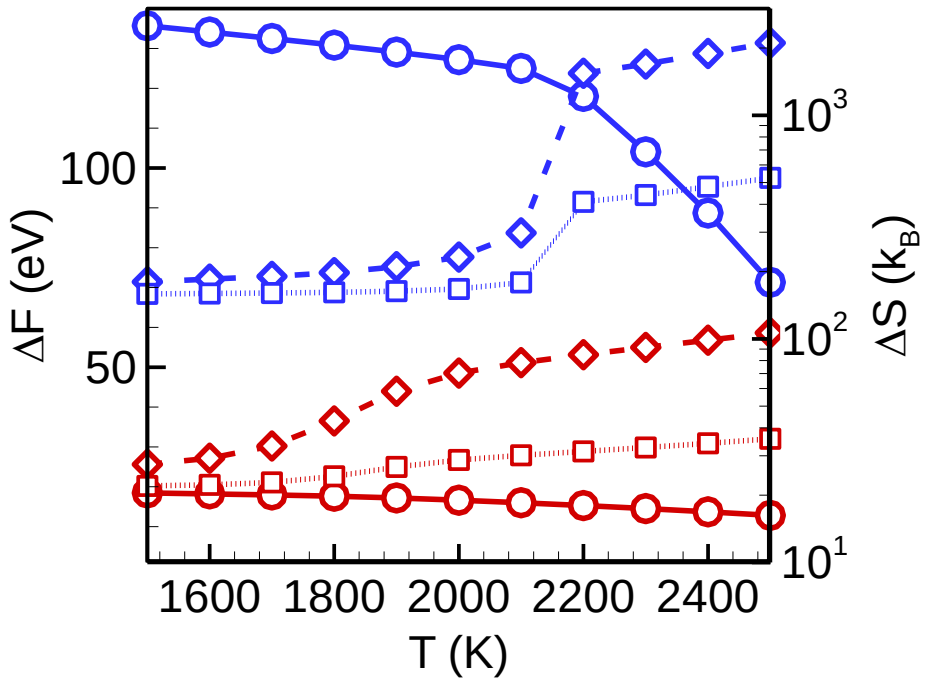

Figure 5.7. Formation free energy (solid lines and circles), formation enthalpy (dotted lines and squares), and formation entropy (dashed lines and diamonds) as a function of temperature for the 10I (red) and 150I (blue) clusters.

Shown in Figure 5.8 is the average morphological state of self-interstitial clusters as a function of temperature and cluster size. A continuous order parameter, $\langle\phi\rangle$, is defined by assigning a value of $\phi=1$ to all planar configurations and $\phi=0$ to amorphous ones and then computing a weighted average over all configurations using the inherent structure PDFs at each temperature and cluster size, i.e.,

$$\langle\phi\rangle(T)=\int\phi P(\Delta E,T)d(\Delta E). \tag{5.10}$$

Note that small clusters (N_i<~15) were defined as blobs in the absence of clear planar character; this assignment does not account for the fact that some of the small cluster configurations correspond to planar precursors and therefore the averaged morphological order parameter is not as meaningful in the small cluster size limit. As shown in Figure 5.8. Morphological order parameter, $\langle\phi\rangle$, as a function of temperature

and cluster size., the amorphous blob phase is dominant at high temperature (>~2100K) for all sizes, although larger clusters persist in planar configurations up to slightly higher temperatures. Comparison of the data in Figure 5.6(b) and Figure 5.8 confirms that the transition to the blob phase corresponds to a rapid increase in the configurational entropy.

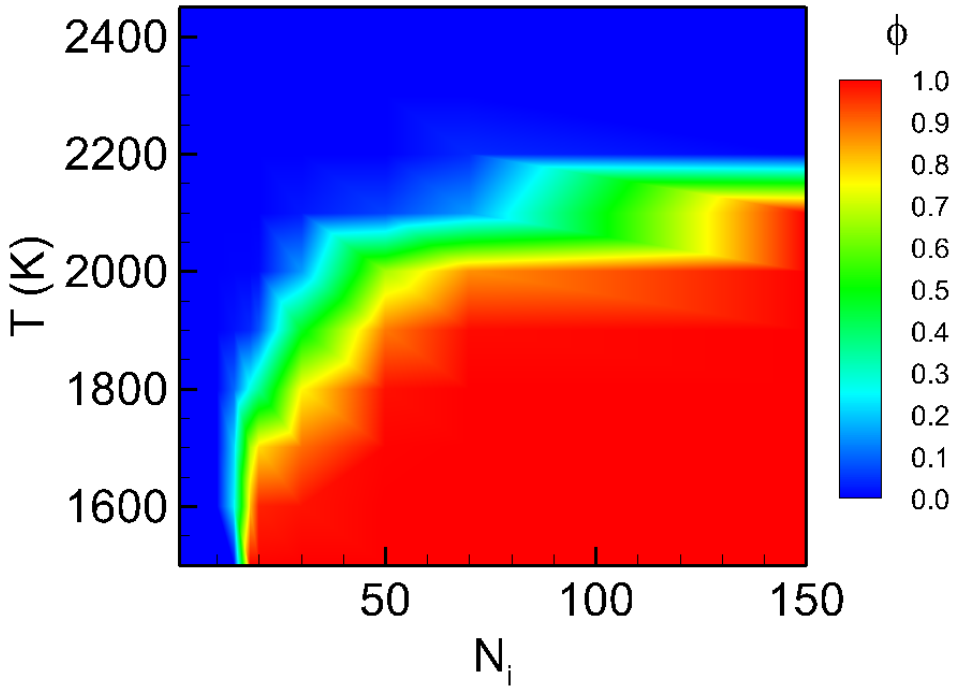

Figure 5.8. Morphological order parameter, $\langle \phi \rangle$, as a function of temperature and cluster size. A value of 1 corresponds to purely planar configurations, while a value of 0 represents blob configurations.

5.8 Capture Zones for Self-Interstitial Clusters

Cluster capture zones are defined as the volume surrounding a cluster in which a mobile entity, typically a single self-interstitial, "sees" the cluster and, assuming that the interaction is favorable, is captured by it. The precise definition of a cluster capture zone is difficult. Dynamical simulations in which single self-interstitials are released near the cluster and tracked require that the capture probability be sampled over many different

configurations and from many different approach directions. Moreover, it is often difficult to determine unambiguously whether a monomer was in fact directly captured or wandered around the simulation cell before finding the cluster. Here, we employed the displacement criterion described in Section 5.3 to define regions that are characterized by a threshold amount of elastic strain. The threshold displacement magnitude, β, was studied parametrically because the precise amount of lattice strain required for capture is not known *a priori*. Once all displaced atoms were tagged, their Voronoi volume, V_c, was computed using the LAMMPS software.

The planar configurations shown in Figure 5.2 and Figure 5.3 suggest that spherical capture zones may reasonably be assumed for both planar and blob configurations. In fact, there is experimental evidence that the coarsening dynamics of these defects are best described on the basis of spheres rather than two-dimensional objects [208]. Within the spherical assumption a capture radius, r_c, is given by

$$r_c(\beta) = \left(\frac{3}{4\pi} V_c(\beta) \right)^{1/3}. \tag{5.11}$$

Shown in Figure 5.9 is the capture radius as a function of the displacement threshold, β, for different individual morphologies of the 70I cluster. The capture radii of the FDL and PDL configurations, which are quite similar, are both always much higher than that of the blob configuration. The results in Figure 5.9 suggest that the capture radius changes significantly as clusters transition between planar and blob configurations, however, there is little sensitivity of the capture radii on configurational variations within a particular morphology, e.g., all FDL and PDL configurations are quite similar in capture zone size. Bearing this in mind, a configurationally-weighted capture radius as a function of cluster

size and temperature may be estimated by considering a few (~5) representative configurations of each morphology and applying the averaged morphological order parameter,

$$\langle r_c \rangle = \langle \phi \rangle r_c^{planar} + \left(1 - \langle \phi \rangle\right) r_c^{blob}, \tag{5.12}$$

where r_c^{planar} and r_c^{blob} are the average planar and blob capture radii, respectively. The results for $\beta = 0.4$ Å are shown in Figure 5.10 for all cluster sizes and temperatures considered in the present study. Although the configurationally-averaged capture radius for small clusters (N_i<50) is relatively insensitive to temperature, larger clusters exhibit a very sharp drop in capture radius at ~2100K as planar configurations transition to 3-dimensional ones. While the precise magnitude of this drop somewhat depends on the assumed atomic displacement threshold for capture, the transition temperature is entirely dictated by the morphological transition from plate to blob configurations.

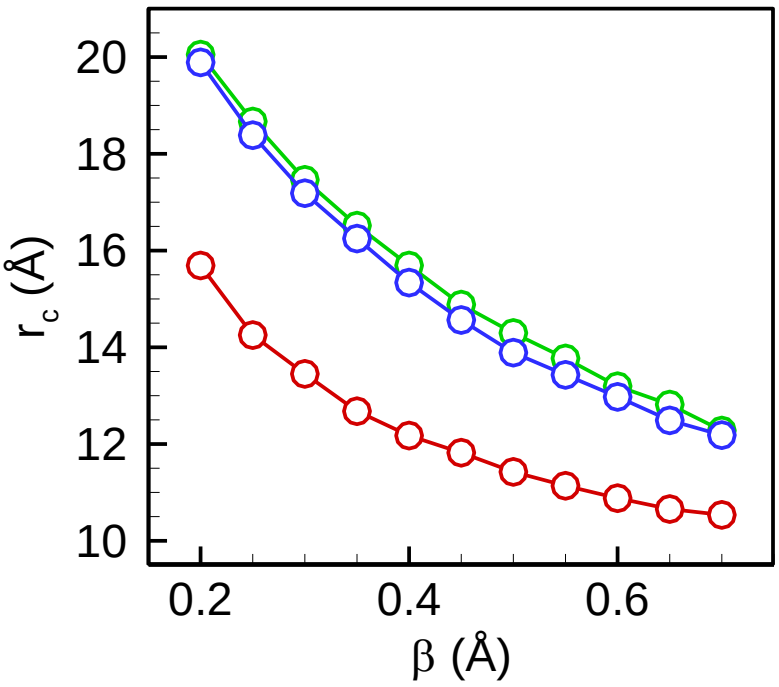

Figure 5.9. Capture radius, r_c, as a function of the displacement threshold, β, for individual 70I cluster configurations: green – FDL (ΔE = 125.06 eV), blue – PDL (ΔE = 106.31 eV), red – blob (ΔE = 226.10 eV).

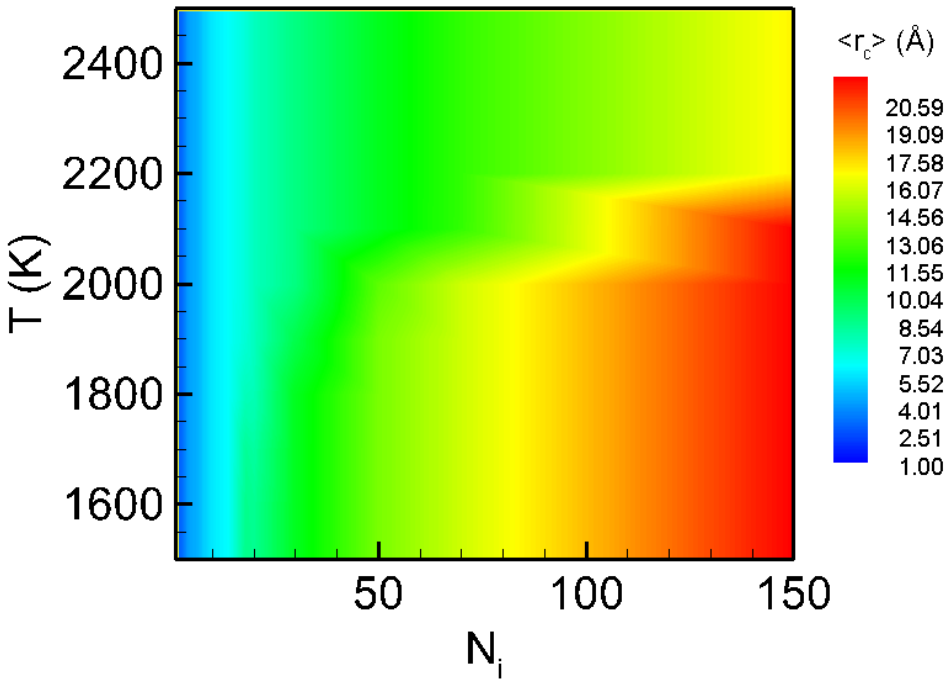

Figure 5.10. Cluster capture radius as a function of temperature for various sizes for $\beta = 0.4$.

5.9 Conclusions

The formation thermodynamics and capture zones of silicon self-interstitial clusters were studied computationally across a wide range of temperatures and cluster sizes. While the ground state thermodynamics of small interstitial clusters have been addressed computationally in previous studies, here we provide a comprehensive quantitative analysis of larger self-interstitial clusters across a wide range of sizes and temperatures. This information represents a critical input into rate equation-based models for predicting the size distribution and density of self-interstitial clusters resulting during silicon crystal growth or wafer annealing. To date, such models have been successfully applied to the quantitative prediction of vacancy cluster (void) size distributions but much less information is available for self-interstitial clusters.

The task of computing formation free energies and capture zones for silicon self-interstitials is substantially complicated by their rich morphological behavior. First, clusters above a critical size are able to assume multiple macroscopically distinct configurations – low formation energy configurations correspond to one of multiple types of {111}-oriented dislocation loops ("plates"), while high energy configurations are amorphous and roughly spherical ("blobs"). These two "macro-phases" of self-interstitial clusters are separated by a substantial free energy barrier that increases with cluster size and makes it practically impossible to sample across the transition for clusters containing more than about 30-40 interstitials. Secondly, each macro-phase is represented by an enormous number of microscopically distinct configurations, collectively representing significant configurational entropy. To address these challenges we employ a computational framework based on the sampling of inherent structures that we have previously successfully applied to vacancy clusters. We also apply the replica exchange technique to enhance configurational sampling across a wide range of cluster energies by exchanging configurations between multiple simultaneously running MD simulations, each being executed at a different temperature.

The resulting free energy and capture zone surfaces provide a quantitative and comprehensive view of interstitial cluster free energies as a function of temperature and cluster size. Most importantly the calculations span the transition between disordered, three-dimensional configurations that possess high energy and high entropy, and highly structured, planar dislocation loops that are generally lower in both energy and entropy. The ability to seamlessly bridge this transition effectively enables extrapolation of the computed data to cluster sizes and temperatures beyond the ranges computed in the

present work and should provide essential input to continuum rate equation models of silicon self-interstitial clustering.

Chapter 6. Conclusions and Future Work

6.1 A Tersoff-Based Empirical Interatomic Potential Model for Ge-Si-O Ternary System

An empirical potential model for the Ge-Si-O system based on the Tersoff framework was studied in detail to determine its suitability for the Ge-on-Si selective epitaxial growth (SEG). Two variants of the potential model were proposed that differ by the interaction cutoff function for the Si atoms. The results from these two variants were compared using a single free fitting parameter for Ge-O interaction strength. Both variants were able to describe at least semi-quantitatively a wide range of properties that are relevant to SEG, including structural properties of the bulk SiO_2, energetics of the Si-SiO_2 and Ge-SiO_2 interfaces, as well as Ge binding on the amorphous SiO_2 (a-SiO_2) surface.

Our study addressed a universal challenge for empirical potentials – namely that it is generally not possible to capture quantitatively all properties of interest, particularly in complex, multicomponent systems. That said, the large number of structural and thermodynamic properties considered in this work indicates that such a framework is sufficiently accurate for capturing many of the processes that are relevant to selective epitaxial growth of Ge on Si/SiO_2 substrates. The best overall representation of the properties was achieved for both potential variants when the fitting parameter was about 0.8, i.e., the Ge-O interaction strength is about 80% of the Si-O interaction.

The potential model characterized for the Si-Ge-O ternary system was used to simulate the nucleation of Ge islands on a-SiO_2 during Ge deposition at a wide range of fluxes and temperatures. In accord with prior experimental analysis, the deposition

physics was described well by the so-called extremely incomplete condensation regime whereby island growth proceeds by direct impingement from the vapor phase rather than diffusional transport on the surface. This behavior was explained by the highly heterogeneous binding environment to Ge atoms presented by the a-SiO_2 surface. A rate-equation based framework was used to identify the deposition regime under which the experiments were performed, and then to systematically steer the simulations towards it by altering the temperature and deposition flux. Once in the experimentally-relevant deposition regime, the rate equation framework was used again to identify quantities that allow for quantitative comparison with experiments, even though the simulation length, time, and temperature scales are all different than the experimental ones.

An important conclusion from our study was the ability to simulate atomic deposition, using straightforward, direct MD simulations, at experimentally meaningful conditions. The timescale restriction associated with MD simulations was well-established in the literature. However, we found that it was possible to reach a regime where key measures of the deposition process no longer depend on the flux, enabling us to make detailed, quantitative comparison to experimental measurements. Our model predicted various measures—namely the critical island size and quantitative temperature dependence—that are in excellent quantitative agreement with experiments. Our study provided strong evidence that realistic deposition rates did not necessarily have to be achieved in atomistic simulations in order to make quantitative predictions.

Overall, our study of the Tersoff-based empirical potential framework showed excellent quantitative agreement with experiments and *ab initio* calculations for many structural and energetic properties of the Ge-Si-O ternary system, as well as the deposition physics of Ge on a-SiO_2 surfaces. Our results were somewhat surprising given

the complexity of the ternary Ge-Si-O system with the omission of explicit charge modeling in considering interactions with oxygen. Collectively, our findings confirmed the Tersoff-based empirical potential was well-suited for the atomistic study of the Ge-on-Si SEG system. More generally, the overall success of the Tersoff framework in describing the ternary system studied here demonstrated the flexibility of (classical) bond-order potentials to capture complex interatomic interactions.

6.1.1 Island Coalescence and Origins of Stacking Fault Formation during SEG

The computational framework carefully validated in this thesis can be readily applied in the study of island coalescence during SEG. As mentioned in Ref. [13], the formation of stacking faults in the SEG film is suspected to take place during Ge island coalescence. Large-scale atomistic simulations of Ge island coalescence with the well-characterized empirical potential model will allow for direct connections to the experiments. An example system to model Ge island coalescence is shown in Figure 6.1, where two adjacent Ge islands are in registry with the underlying Si substrate through openings in the a-SiO_2 layer. The size of the Ge islands, the window spacing in the a-SiO_2 layer as well as the a-SiO_2 thickness shown in Figure 6.1 were constructed based on experimental measurements [11, 53] to closely resemble the SEG system. Our previous analysis on random nucleation of Ge islands on a-SiO_2 under Ge deposition can be used to determine the optimal deposition flux that minimizes secondary island nucleation in such systems. By varying quantities such as Si-Ge contact area and island aspect ratio, one can determine the effects of lattice mismatch strain and Ge island morphology on the coalescence behavior.

One possible bottleneck for the coalescence simulations is that the island growth may be too slow for MD and the simulation become too inefficient for island to grow into contact. One can initialize the system with larger islands to minimize inter-island spacing, however, the possibility of biasing the coalescence behavior with artificially initialized island morphology increases with initial island size. Other approaches to overcome this problem are the applications of accelerated simulation methods, such as coarse projective integration or kinetic Monte Carlo. These methods can be applied to speed up island growth and coalescence while maintaining realistic island morphologies. Such multiscale approaches may be further extended to model film formation from island coalescence. These studies can serve as a predictive tool for future improvements on the SEG of Ge-on-Si.

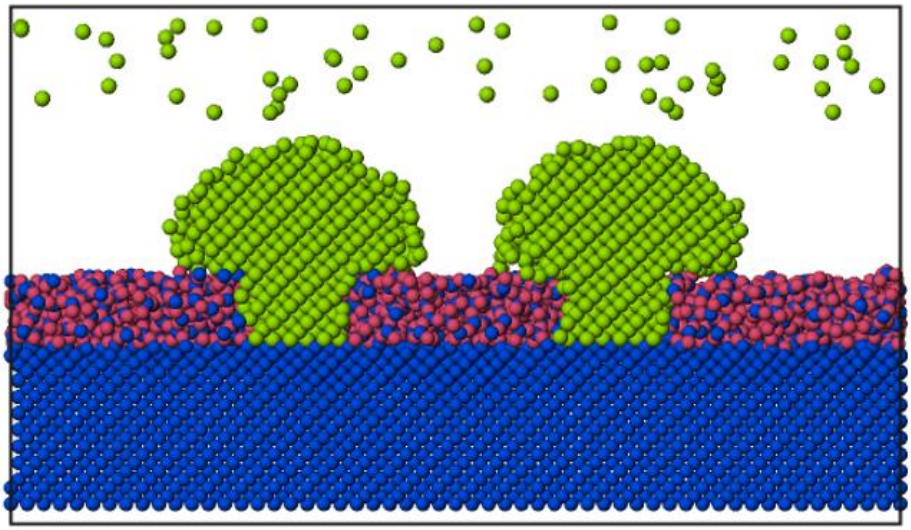

Figure 6.1. System setup for modeling Ge island coalescence during SEG. The Ge islands are in contact with the Si substrate through openings in the a-SiO_2 layer. Ge deposition is represented by Ge atoms in the vapor phase above the islands. Green atoms: Ge; red atoms: O; blue atoms: Si.

6.2 Multiscale Modeling of Ge Deposition on Amorphous SiO_2 by Coarse Projective Integration

The wide range of timescales for deposition processes that span orders-of-magnitude presented challenges when modeling the deposition system. Coarse projective integration (CPI), a multiscale modeling technique that exploits the separation of timescales commonly found in complex systems, was a promising approach to computationally study the deposition systems. The fundamental idea behind equation-free analysis was that many systems that were governed by fast, often stochastic, microprocesses, also exhibited a slowly-evolving manifold defined by some coarse variables. In CPI, short MD simulations would be used to compute temporal gradients of the coarse variables at given points in time, which would in turn be used to evolve differential equations in the coarse variables over time intervals that are large relative to the microprocesses, but small relative to the coarse variable timescales.

We investigated the application of coarse projective integration to the deposition and islanding of Ge on an a-SiO_2 surface. We focused on the major challenge in applying CPI to deposition in morphologically complex situations, namely the reconstruction of an atomistic configuration only from knowledge of coarse variables (a process called 'lifting'). With collected island configurations from previous deposition simulations of Ge on a-SiO_2 in Chapter 3, we proposed a lifting procedure based on a given island size distribution (ISD), in which island configurations were randomly chosen from the collection and placed at randomly selected positions on the surface. The islands were stabilized on the surface through sequence of short constant-temperature anneals in NVT-MD. The lifting procedure was tested by constructing atomic systems based on the ISD from direct simulations. Using the quantities such as low order moments of the ISD,

the monomer density, and maximum island size as the coarse variables, we demonstrated that the lifted systems exhibited the same coarse evolution as direct MD simulations, thereby validating the proposed lifting procedure. Moreover, a healing period at the initial stage of the coarse evolution was observed in the lifted systems, in which the errors in the reconstructed system introduced during lifting was relaxed by the fast-evolving processes. The healing behavior confirmed the presence of timescale separation, further justified the use of CPI for deposition of Ge on a-SiO_2 surfaces.

Furthermore, since the stochastic nature of the full ISD rendered it an unsuitable candidate for coarse variables in CPI, a reduced representation of the ISD (reduced ISD) was derived using the coarse variables mentioned above. The agreement on the coarse evolutions of the lifted systems based the reduced ISD and of direct MD simulations supported the formulation of the reduced ISDs presented in this work. Overall, our analysis addressed the key issues on applying CPI to the Ge-on-SiO_2 deposition system. More broadly, the lifting procedure, the reduced ISD representation, as well as the identified coarse variables presented in our work can be easily adapted for other deposition systems where CPI would be an extremely powerful computational tool.

6.2.1 Coarse Projective Integration for Deposition and Islanding of Ge on a-SiO_2

Our work so far addressed the primary challenges in applying CPI for deposition of Ge on a-SiO_2, namely the lifting procedure. Furthermore, the coarse variables and reduced ISD presented here already constitutes a coarse time-stepper scheme, where one can lift, evolve, and restrict based on the low-order moments of the ISD, the monomer number density, and maximum island size. The next step is to incorporate a numerical integration scheme to perform CPI on the Ge deposition system. Using the direct MD

results as the reference, the quality of the numerical integrator will be carefully tested before extending to timescales beyond the reach of MD.

6.3 Thermodynamic Analysis of Self-Interstitial Clusters in Silicon

A computational study of the formation thermodynamics and capture zones of Si self-interstitial clusters were performed across a wide range of temperature and cluster sizes. The rich morphological behavior of the self-interstitial clusters complicated the calculation of their free energies and capture zones. The difficulties were two-fold: first, for clusters greater than the critical size (~ 30-40 interstitials), there existed multiple macroscopically distinct configurations, separated by substantial free energy barrier that increased with cluster size. The two "macro-phases" were (1) three-dimensional amorphous, roughly spherical, clusters that were high in formation energies ("blobs") and (2) {111}-oriented dislocation loops with low formation energies ("plates"). Secondly, each of these macro-phases consisted of numerous microscopically distinct configurations, collectively representing significant configurational entropy. We addressed these challenges by applying a computational framework of inherent structure sampling in combination with the replica exchange molecular dynamics method for enhanced configurational sampling across a wide range of cluster energies.

The free energy and capture zone surfaces computed in this work as functions of temperature and cluster size spanned the transition between the two macro-phases—the disordered, three-dimensional configurations that were high in formation energies and entropies, and the highly-structured, planar dislocation loops that were lower in both formation energies and entropies. The transitions were seamlessly bridged in this work, thus enabled extrapolation of the computed results to cluster sizes and temperatures

beyond the range covered in the present work. Our results provided critical insight in the formation thermodynamics of self-interstitial clusters with significant contribution to the prediction of size distributions and density of self-interstitial clusters during silicon crystal growth or wafer annealing.

BIBLIOGRAPHY

1. Karam, N.H., et al., *Development and characterization of high-efficiency Ga0.5In0.5P/GaAs/Ge dual- and triple-junction solar cells.* Ieee Transactions on Electron Devices, 1999. **46**(10): p. 2116-2125.
2. Fichthorn, K.A. and M. Scheffler, *Island nucleation in thin-film epitaxy: A first-principles investigation.* Physical Review Letters, 2000. **84**(23): p. 5371-5374.
3. Andre, C.L., et al., *Investigations of high-performance GaAs solar cells grown on Ge-Si1-xGex-Si substrates.* Ieee Transactions on Electron Devices, 2005. **52**(6): p. 1055-1060.
4. King, R.R., et al., *40% efficient metamorphic GaInP/GaInAs/Ge multijunction solar cells.* Applied Physics Letters, 2007. **90**(18).
5. Kerestes, C., et al., *Fabrication and analysis of multijunction solar cells with a quantum dot (In)GaAs junction.* Progress in Photovoltaics, 2014. **22**(11): p. 1172-1179.
6. Ahn, D., et al., *High performance, waveguide integrated Ge photodetectors.* Optics Express, 2007. **15**(7): p. 3916-3921.
7. Michel, J., J.F. Liu, and L.C. Kimerling, *High-performance Ge-on-Si photodetectors.* Nature Photonics, 2010. **4**(8): p. 527-534.
8. Luryi, S. and E. Suhir, *New Approach to the High-Quality Epitaxial-Growth of Lattice-Mismatched Materials.* Applied Physics Letters, 1986. **49**(3): p. 140-142.
9. Langdo, T.A., et al., *High quality Ge on Si by epitaxial necking.* Applied Physics Letters, 2000. **76**(25): p. 3700-3702.
10. Li, Q.M., et al., *Selective growth of Ge on Si(100) through vias of SiO2 nanotemplate using solid source molecular beam epitaxy.* Applied Physics Letters, 2003. **83**(24): p. 5032-5034.
11. Li, Q.M., et al., *Heteroepitaxy of high-quality Ge on Si by nanoscale Ge seeds grown through a thin layer of SiO2.* Applied Physics Letters, 2004. **85**(11): p. 1928-1930.
12. Leonhardt, D. and S.M. Han, *Energetics of Ge nucleation on SiO2 and implications for selective epitaxial growth.* Surface Science, 2009. **603**(16): p. 2624-2629.
13. Leonhardt, D., S. Ghosh, and S.M. Han, *Origin and removal of stacking faults in Ge islands nucleated on Si within nanoscale openings in SiO2.* Journal of Applied Physics, 2011. **110**(7).
14. Tersoff, J., *Modeling Solid-State Chemistry - Interatomic Potentials for Multicomponent Systems.* Physical Review B, 1989. **39**(8): p. 5566-5568.
15. Lee, B.M., et al., *Generation of glass SiO2 structures by various cooling rates: A molecular-dynamics study.* Computational Materials Science, 2006. **37**(3): p. 203-208.
16. Baumann, F.H., et al., *Multiscale modeling of thin-film deposition: Applications to Si device processing.* Mrs Bulletin, 2001. **26**(3): p. 182-189.
17. Schulze, T.P., P. Smereka, and E. Weinan, *Coupling kinetic Monte-Carlo and continuum models with application to epitaxial growth.* Journal of Computational Physics, 2003. **189**(1): p. 197-211.

18. Schulze, T.P., *A hybrid scheme for simulating epitaxial growth.* Journal of Crystal Growth, 2004. **263**(1-4): p. 605-615.
19. Sun, Y., R. Caflisch, and B. Engquist, *A Multiscale Method for Epitaxial Growth.* Multiscale Modeling & Simulation, 2011. **9**(1): p. 335-354.
20. Fan, J.H., L. He, and R.J. Stewart, *Concurrent and Hierarchical Multiscale Analysis for Layer-Thickness Effects of Nanoscale Coatings on Interfacial Stress and Fracture Behavior.* Journal of Engineering Materials and Technology-Transactions of the Asme, 2012. **134**(3).
21. Kevrekidis, I.G., et al., *Equation-Free, Coarse-Grained Multiscale Computation: Enabling Microscopic Simulators to Perform System-Level Analysis.* Communications in Mathematical Sciences, 2003. **1**: p. 715-762.
22. Gear, C.W. and I.G. Kevrekidis, *Projective methods for stiff differential equations: Problems with gaps in their eigenvalue spectrum.* Siam Journal on Scientific Computing, 2003. **24**(4): p. 1091-1106.
23. Kevrekidis, I.G. and G. Samaey, *Equation-Free Multiscale Computation: Algorithms and Applications.* Annual Review of Physical Chemistry, 2009. **60**: p. 321-344.
24. Gear, C.W., et al., *Projecting to a slow manifold: Singularly perturbed systems and legacy codes.* Siam Journal on Applied Dynamical Systems, 2005. **4**(3): p. 711-732.
25. Erhart, P. and K. Albe, *Analytical potential for atomistic simulations of silicon, carbon, and silicon carbide.* Physical Review B, 2005. **71**(3).
26. Nielsen, S.O., et al., *Recent progress in adaptive multiscale molecular dynamics simulations of soft matter.* Physical Chemistry Chemical Physics, 2010. **12**(39): p. 12401-12414.
27. Yoon, B., et al., *Charging effects on bonding and catalyzed oxidation of CO on Au-8 clusters on MgO.* Science, 2005. **307**(5708): p. 403-407.
28. Diemand, J., et al., *Large scale molecular dynamics simulations of homogeneous nucleation.* Journal of Chemical Physics, 2013. **139**(7).
29. Gu, X.W., et al., *Size-Dependent Deformation of Nanocrystalline Pt Nanopillars.* Nano Letters, 2012. **12**(12): p. 6385-6392.
30. Paul, W. and G.D. Smith, *Structure and dynamics of amorphous polymers: computer simulations compared to experiment and theory.* Reports on Progress in Physics, 2004. **67**(7): p. 1117-1185.
31. Lim, W.K. and A.R. Denton, *Polymer crowding and shape distributions in polymer-nanoparticle mixtures.* Journal of Chemical Physics, 2014. **141**(11).
32. Venturoli, M., B. Smit, and M.M. Sperotto, *Simulation studies of protein-induced bilayer deformations, and lipid-induced protein tilting, on a mesoscopic model for lipid bilayers with embedded proteins.* Biophysical Journal, 2005. **88**(3): p. 1778-1798.
33. Monticelli, L., et al., *The MARTINI coarse-grained force field: Extension to proteins.* Journal of Chemical Theory and Computation, 2008. **4**(5): p. 819-834.
34. Henriques, J. and M. Skepo, *A coarse-grained model for flexible (phospho)proteins: Adsorption and bulk properties.* Food Hydrocolloids, 2015. **43**: p. 473-480.

35. Backofen, R., R. Bergamaschini, and A. Voigt, *The interplay of morphological and compositional evolution in crystal growth: a phase-field model.* Philosophical Magazine, 2014. **94**(19): p. 2162-2169.
36. Kuryliuk, V.V. and O.A. Korotchenkov, *Features of the stress-strain state of Si/SiO2/Ge heterostructures with germanium nanoislands of a limited density.* Semiconductors, 2013. **47**(8): p. 1031-1036.
37. Stillinger, F.H. and T.A. Weber, *Computer-Simulation of Local Order in Condensed Phases of Silicon.* Physical Review B, 1985. **31**(8): p. 5262-5271.
38. Bazant, M.Z., E. Kaxiras, and J.F. Justo, *Environment-dependent interatomic potential for bulk silicon.* Physical Review B, 1997. **56**(14): p. 8542-8552.
39. Lee, B.J., *A modified embedded atom method interatomic potential for silicon.* Calphad-Computer Coupling of Phase Diagrams and Thermochemistry, 2007. **31**(1): p. 95-104.
40. Tersoff, J., *New Empirical-Model for the Structural-Properties of Silicon.* Physical Review Letters, 1986. **56**(6): p. 632-635.
41. Tersoff, J., *Empirical Interatomic Potential for Silicon with Improved Elastic Properties.* Physical Review B, 1988. **38**(14): p. 9902-9905.
42. Lafontaine, H., et al., *Photoluminescence study of initial interdiffusion of SiGe/Si quantum wells grown by ultrahigh vacuum-chemical vapor deposition.* Applied Physics Letters, 1996. **69**(10): p. 1444-1446.
43. Shah, V.A., et al., *Reverse graded strain relaxed SiGe buffers for CMOS and optoelectronic integration.* Thin Solid Films, 2012. **520**(8): p. 3227-3231.
44. Currie, M.T., et al., *Controlling threading dislocation densities in Ge on Si using graded SiGe layers and chemical-mechanical polishing.* Applied Physics Letters, 1998. **72**(14): p. 1718-1720.
45. Luan, H.C., et al., *High-quality Ge epilayers on Si with low threading-dislocation densities.* Applied Physics Letters, 1999. **75**(19): p. 2909-2911.
46. Tweet, D.J., et al., *Characterization and reduction of twist in Ge on insulator produced by localized liquid phase epitaxy.* Applied Physics Letters, 2005. **87**(14).
47. Miyao, M., et al., *High-quality single-crystal Ge stripes on quartz substrate by rapid-melting-growth.* Applied Physics Letters, 2009. **95**(2).
48. Liu, Y.C., M.D. Deal, and J.D. Plummer, *High-quality single-crystal Ge on insulator by liquid-phase epitaxy on Si substrates.* Applied Physics Letters, 2004. **84**(14): p. 2563-2565.
49. Miyao, M., et al., *Giant Ge-on-Insulator Formation by Si-Ge Mixing-Triggered Liquid-Phase Epitaxy.* Applied Physics Express, 2009. **2**(4).
50. Bai, J., et al., *Study of the defect elimination mechanisms in aspect ratio trapping Ge growth.* Applied Physics Letters, 2007. **90**(10).
51. Luryi, S., A. Kastalsky, and J.C. Bean, *New Infrared Detector on a Silicon Chip.* Ieee Transactions on Electron Devices, 1984. **31**(9): p. 1135-1139.
52. Leonhardt, D. and S.M. Han, *Dislocation reduction in heteroepitaxial Ge on Si using SiO2 lined etch pits and epitaxial lateral overgrowth.* Applied Physics Letters, 2011. **99**(11).
53. Li, Q.M., et al., *Probing interactions of Ge with chemical and thermal SiO2 to understand selective growth of Ge on Si during molecular beam epitaxy.* Journal of Physical Chemistry C, 2007. **111**(2): p. 779-786.

54. Kapur, S.S., M. Prasad, and T. Sinno, *Carbon-mediated aggregation of self-interstitials in silicon: A large-scale molecular dynamics study.* Physical Review B, 2004. **69**(15).
55. Sinno, T., *A bottom-up multiscale view of point-defect aggregation in silicon.* Journal of Crystal Growth, 2007. **303**(1): p. 5-11.
56. Nieves, A.M., V. Vitek, and T. Sinno, *Monte Carlo analysis of stress-directed phase segregation in binary thin film alloys under nonisothermal annealing.* Applied Physics Letters, 2008. **93**(19).
57. Nieves, A.M., V. Vitek, and T. Sinno, *Atomistic analysis of phase segregation patterning in binary thin films using applied mechanical fields.* Journal of Applied Physics, 2010. **107**(5).
58. Sinno, T. and M. Prasad, *Internally consistent verification of mean-field models for aggregation using large-scale molecular dynamics.* Molecular Physics, 2004. **102**(4): p. 395-403.
59. Prasad, M. and T. Sinno, *Internally consistent approach for modeling solid-state aggregation. I. Atomistic calculations of vacancy clustering in silicon.* Physical Review B, 2003. **68**(4): p. 45206 1-12.
60. Frewen, T.A., et al., *A microscopically accurate continuum model for void formation during semiconductor silicon processing.* Journal of Crystal Growth, 2005. **279**(3-4): p. 258-271.
61. Munetoh, S., et al., *Interatomic potential for Si-O systems using Tersoff parameterization.* Computational Materials Science, 2007. **39**(2): p. 334-339.
62. Lee, B.M., T. Motooka, and S. Munetoh, *Molecular-dynamics simulations of nucleation and crystallization processes of laser crystallized poly-Si.* Journal of Physics-Condensed Matter, 2008. **20**(5).
63. Okada, Y. and Y. Tokumaru, *Precise Determination of Lattice-Parameter and Thermal-Expansion Coefficient of Silicon between 300-K and 1500-K.* Journal of Applied Physics, 1984. **56**(2): p. 314-320.
64. Plimpton, S., *Fast Parallel Algorithms for Short-Range Molecular-Dynamics.* Journal of Computational Physics, 1995. **117**(1): p. 1-19.
65. Shinoda, W., M. Shiga, and M. Mikami, *Rapid estimation of elastic constants by molecular dynamics simulation under constant stress.* Physical Review B, 2004. **69**(13).
66. Vollmayr, K., W. Kob, and K. Binder, *Cooling-rate effects in amorphous silica: A computer-simulation study.* Physical Review B, 1996. **54**(22): p. 15808-15827.
67. Bruckner, R., *Properties and structure of vitreous silica. I.* Journal of Non-Crystalline Solids, 1970. **5**(2): p. 123-175.
68. Sarnthein, J., A. Pasquarello, and R. Car, *Model of Vitreous Sio2 Generated by an Ab-Initio Molecular-Dynamics Quench from the Melt.* Physical Review B, 1995. **52**(17): p. 12690-12695.
69. Malfait, W.J., W.E. Halter, and R. Verel, *Si-29 NMR spectroscopy of silica glass: T-1 relaxation and constraints on the Si-O-Si bond angle distribution.* Chemical Geology, 2008. **256**(3-4): p. 269-277.
70. Mizele, J., J.L. Dandurand, and J. Schott, *Determination of the Surface-Energy of Amorphous Silica from Solubility Measurements in Micropores.* Surface Science, 1985. **162**(1-3): p. 830-837.

71. Djurabekova, F. and K. Nordlund, *Atomistic simulation of the interface structure of Si nanocrystals embedded in amorphous silica.* Physical Review B, 2008. **77**(11).
72. Kroll, P. and H.J. Schulte, *Shell-like structure of valence band orbitals of silicon nanocrystals in silica glass.* Physica Status Solidi B-Basic Solid State Physics, 2006. **243**(6): p. R47-R49.
73. Du, J.C. and P. Kroll, *Electronic structure and interfacial properties of Ge nanoclusters embedded in amorphous silica.* Journal of Non-Crystalline Solids, 2010. **356**(44-49): p. 2448-2453.
74. Kaiser, N., et al., *Wetting angle and surface tension of germanium melts on different substrate materials.* Journal of Crystal Growth, 2001. **231**(4): p. 448-457.
75. Bakaev, V.A. and W.A. Steele, *Grand Canonical Ensemble Computer-Simulation of Adsorption of Argon on a Heterogeneous Surface.* Langmuir, 1992. **8**(1): p. 148-154.
76. Bakaev, V.A., et al., *Adsorption of CO2 and Ar on glass surfaces. Computer simulation and experimental study.* Journal of Chemical Physics, 1999. **111**(21): p. 9813-9821.
77. Frenkel, D. and B. Smit, *Understanding molecular simulation : from algorithms to applications*. 2nd ed. Computational science ; v. 1. 2002, San Diego, Calif.: Academic Press. xxii, 638 p.
78. Sing, K.S.W., et al., *Reporting Physisorption Data for Gas Solid Systems with Special Reference to the Determination of Surface-Area and Porosity (Recommendations 1984).* Pure and Applied Chemistry, 1985. **57**(4): p. 603-619.
79. Myers, A.L., *Thermodynamics of adsorption in porous materials.* Aiche Journal, 2002. **48**(1): p. 145-160.
80. Wakayama, Y., T. Tagami, and S. Tanaka, *Three-dimensional islands of Si and Ce formed on SiO2 through crystallization and agglomeration from amorphous thin films.* Thin Solid Films, 1999. **350**(1-2): p. 300-307.
81. Brunco, D.P., et al., *Germanium MOSFET devices: Advances in materials understanding, process development, and electrical performance.* Journal of the Electrochemical Society, 2008. **155**(7): p. H552-H561.
82. Kamata, Y., *High-k/Ge MOSFETs for future nanoelectronics.* Materials Today, 2008. **11**(1-2): p. 30-38.
83. Holman, Z.C., C.Y. Liu, and U.R. Kortshagen, *Germanium and Silicon Nanocrystal Thin-Film Field-Effect Transistors from Solution.* Nano Letters, 2010. **10**(7): p. 2661-2666.
84. Hosoi, T., et al., *Mobility characterization of Ge-on-insulator metal-oxide-semiconductor field-effect transistors with striped Ge channels fabricated by lateral liquid-phase epitaxy.* Applied Physics Letters, 2014. **105**(17).
85. People, R. and J.C. Bean, *Calculation of Critical Layer Thickness Versus Lattice Mismatch for Gexsi1-X/Si Strained-Layer Heterostructures.* Applied Physics Letters, 1985. **47**(3): p. 322-324.
86. Young, W.M. and E.W. Elcock, *Monte Carlo Studies of Vacancy Migration in Binary Ordered Alloys - I.* Proceedings of the Physical Society of London, 1966. **89**(565P): p. 735-&.

87. Battaile, C.C., *The kinetic Monte Carlo method: Foundation, implementation, and application.* Computer Methods in Applied Mechanics and Engineering, 2008. **197**(41-42): p. 3386-3398.
88. Voter, A.F., *Introduction to the Kinetic Monte Carlo Method*, in *Radiation effects in solids* K.E. Sickafus, E.A. Kotomin, and B.P. Uberuaga, Editors. 2007, Springer: Dordrecht, Netherlands. p. 1-23.
89. Bortz, A.B., M.H. Kalos, and J.L. Lebowitz, *New Algorithm for Monte-Carlo Simulation of Ising Spin Systems.* Journal of Computational Physics, 1975. **17**(1): p. 10-18.
90. Fichthorn, K.A. and W.H. Weinberg, *Theoretical Foundations of Dynamic Monte-Carlo Simulations.* Journal of Chemical Physics, 1991. **95**(2): p. 1090-1096.
91. Dai, J.G., et al., *On-lattice kinetic Monte Carlo simulations of point defect aggregation in entropically influenced crystalline systems.* Physical Review B, 2005. **72**(13).
92. Dai, J., W.D. Seider, and T. Sinno, *Lattice kinetic Monte Carlo simulations of defect evolution in crystals at elevated temperature.* Molecular Simulation, 2006. **32**(3-4): p. 305-314.
93. Dai, J., W.D. Seider, and T. Sinno, *A lattice kinetic Monte Carlo study of void morphological evolution during silicon crystal growth.* Molecular Simulation, 2007. **33**(9-10): p. 733-745.
94. Dai, J.G., W.D. Seider, and T. Sinno, *Coarse-grained lattice kinetic Monte Carlo simulation of systems of strongly interacting particles.* Journal of Chemical Physics, 2008. **128**(19).
95. Bales, G.S. and D.C. Chrzan, *Dynamics of Irreversible Island Growth during Submonolayer Epitaxy.* Physical Review B, 1994. **50**(9): p. 6057-6067.
96. Ratsch, C., et al., *Submonolayer Epitaxy without a Critical Nucleus (Vol 329, Pg L599, 1995).* Surface Science, 1995. **338**(1-3): p. L889-L890.
97. Battaile, C.C., D.J. Srolovitz, and J.E. Butler, *A kinetic Monte Carlo method for the atomic-scale simulation of chemical vapor deposition: Application to diamond.* Journal of Applied Physics, 1997. **82**(12): p. 6293-6300.
98. Mottet, C., et al., *A Monte Carlo simulation of submonolayer homoepitaxial growth on Ag(110) and Cu(110).* Surface Science, 1998. **417**(2-3): p. 220-237.
99. Evans, J.W., P.A. Thiel, and M.C. Bartelt, *Morphological evolution during epitaxial thin film growth: Formation of 2D islands and 3D mounds.* Surface Science Reports, 2006. **61**(1-2): p. 1-128.
100. Zhu, Y.G. and X. Pan, *Kinetic Monte Carlo simulation of 3-D growth of NiTi alloy thin films.* Applied Surface Science, 2014. **321**: p. 24-29.
101. Voter, A.F., F. Montalenti, and T.C. Germann, *Extending the time scale in atomistic simulation of materials.* Annual Review of Materials Research, 2002. **32**: p. 321-346.
102. Henkelman, G. and H. Jonsson, *Long time scale kinetic Monte Carlo simulations without lattice approximation and predefined event table.* Journal of Chemical Physics, 2001. **115**(21): p. 9657-9666.
103. El-Mellouhi, F., N. Mousseau, and L.J. Lewis, *Kinetic activation-relaxation technique: An off-lattice self-learning kinetic Monte Carlo algorithm.* Physical Review B, 2008. **78**(15).

104. Xu, H.X., Y.N. Osetsky, and R.E. Stoller, *Self-evolving atomistic kinetic Monte Carlo: fundamentals and applications.* Journal of Physics-Condensed Matter, 2012. **24**(37).
105. Sorensen, M.R. and A.F. Voter, *Temperature-accelerated dynamics for simulation of infrequent events.* Journal of Chemical Physics, 2000. **112**(21): p. 9599-9606.
106. Voter, A.F., *Hyperdynamics: Accelerated molecular dynamics of infrequent events.* Physical Review Letters, 1997. **78**(20): p. 3908-3911.
107. Montalenti, F., M.R. Sorensen, and A.R. Voter, *Closing the gap between experiment and theory: Crystal growth by temperature accelerated dynamics.* Physical Review Letters, 2001. **87**(12).
108. Miron, R.A. and K.A. Fichthorn, *Multiple-time scale accelerated molecular dynamics: Addressing the small-barrier problem.* Physical Review Letters, 2004. **93**(12).
109. Venables, J.A., *Rate Equation Approaches to Thin-Film Nucleation Kinetics.* Philosophical Magazine, 1973. **27**(3): p. 697-738.
110. Venables, J.A., G.D.T. Spiller, and M. Hanbucken, *Nucleation and Growth of Thin-Films.* Reports on Progress in Physics, 1984. **47**(4): p. 399-459.
111. Chuang, C.Y., et al., *Atomistic analysis of Ge on amorphous SiO2 using an empirical interatomic potential.* Surface Science, 2013. **609**: p. 221-229.
112. Zinsmeis.G, *Theory of Thin Film Condensation .B. Solution of Simplified Condensation Equation.* Thin Solid Films, 1968. **2**(5-6): p. 497-&.
113. Walton, D., *Nucleation of Vapor Deposits.* Journal of Chemical Physics, 1962. **37**(10): p. 2182-&.
114. Stowell, M.J. and Hutchins.Te, *Nucleation Kinetics in Thin Film Growth .2. Analytical Evaluation of Nucleation and Growth Behaviour.* Thin Solid Films, 1971. **8**(1): p. 41-&.
115. Frankl, D.R. and J.A. Venables, *Nucleation on Substrates from Vapour Phase.* Advances in Physics, 1970. **19**(80): p. 409-&.
116. Amar, J.G. and F. Family, *Critical Cluster-Size - Island Morphology and Size Distribution in Submonolayer Epitaxial-Growth (Vol 74, Pg 2066, 1995).* Physical Review Letters, 1995. **75**(10): p. 2069-2069.
117. Bartelt, M.C. and J.W. Evans, *Exact island-size distributions for submonolayer deposition: Influence of correlations between island size and separation.* Physical Review B, 1996. **54**(24): p. 17359-17362.
118. Vvedensky, D.D., *Scaling functions for island-size distributions.* Physical Review B, 2000. **62**(23): p. 15435-15438.
119. Dubrovskii, V.G. and N.V. Sibirev, *Size distributions, scaling properties, and Bartelt-Evans singularities in irreversible growth with size-dependent capture coefficients.* Physical Review B, 2014. **89**(5).
120. Evans, J.W. and M.C. Bartelt, *Nucleation, adatom capture, and island size distributions: Unified scaling analysis for submonolayer deposition.* Physical Review B, 2001. **63**(23).
121. Robbie, D.A. and P.A. Mulheran, *Impact of monomer evaporation on the statistics of island arrays formed in thin film deposition simulations.* Philosophical Magazine B-Physics of Condensed Matter Statistical Mechanics Electronic Optical and Magnetic Properties, 2000. **80**(7): p. 1299-1309.

122. Pimpinelli, A. and T.L. Einstein, *Capture-zone scaling in island nucleation: Universal fluctuation behavior.* Physical Review Letters, 2007. **99**(22).
123. Pimpinelli, A., L. Tumbek, and A. Winkler, *Scaling and Exponent Equalities in Island Nucleation: Novel Results and Application to Organic Films.* Journal of Physical Chemistry Letters, 2014. **5**(6): p. 995-998.
124. Muller, B., et al., *Initial stages of Cu epitaxy on Ni(100): Postnucleation and a well-defined transition in critical island size.* Physical Review B, 1996. **54**(24): p. 17858-17865.
125. Bardotti, L., et al., *High-resolution LEED profile analysis and diffusion barrier estimation for submonolayer homoepitaxy of Ag/Ag(100).* Physical Review B, 1998. **57**(19): p. 12544-12549.
126. Matetskiy, A.V., et al., *Peculiar diffusion of C-60 on In-adsorbed Si(111)root 3 x root 3-Au surface.* Surface Science, 2013. **616**: p. 44-50.
127. Graziosi, P., et al., *Pentacene thin films on ferromagnetic oxide: Growth mechanism and spintronic devices.* Applied Physics Letters, 2014. **105**(2).
128. Stukowski, A., *Visualization and analysis of atomistic simulation data with OVITO-the Open Visualization Tool.* Modelling and Simulation in Materials Science and Engineering, 2010. **18**(1).
129. Jensen, P., et al., *Growth of three-dimensional structures by atomic deposition on surfaces containing defects: simulations and theory.* Surface Science, 1998. **412-13**: p. 458-476.
130. Venables, J., *Introduction to surface and thin film processes*. 2000, Cambrige, UK ; New York: Cambridge University Press. xvi, 372 p.
131. Karakasidis, T.E. and C.A. Charitidis, *Multiscale modeling in nanomaterials science.* Materials Science & Engineering C-Biomimetic and Supramolecular Systems, 2007. **27**(5-8): p. 1082-1089.
132. Brunhes, T., et al., *Electroluminescence of Ge/Si self-assembled quantum dots grown by chemical vapor deposition.* Applied Physics Letters, 2000. **77**(12): p. 1822-1824.
133. Nomura, K., et al., *Thin-film transistor fabricated in single-crystalline transparent oxide semiconductor.* Science, 2003. **300**(5623): p. 1269-1272.
134. Ryu, Y.R., T.S. Lee, and H.W. White, *Properties of arsenic-doped p-type ZnO grown by hybrid beam deposition.* Applied Physics Letters, 2003. **83**(1): p. 87-89.
135. Ohta, H. and H. Hosono, *Transparent oxide optoelectronics.* Materials Today, 2004. **7**(6): p. 42-51.
136. Senthilkumar, V., et al., *Direct vapor phase growth process and robust photo-luminescence properties of large area MoS2 layers.* Nano Research, 2014. **7**(12): p. 1759-1768.
137. Nakamura, S., *InGaN-based violet laser diodes.* Semiconductor Science and Technology, 1999. **14**(6): p. R27-R40.
138. Zhang, J.J., et al., *Evolution of epitaxial semiconductor nanodots and nanowires from supersaturated wetting layers.* Chemical Society Reviews, 2015. **44**(1): p. 26-39.
139. Aqua, J.N., et al., *Growth and self-organization of SiGe nanostructures.* Physics Reports-Review Section of Physics Letters, 2013. **522**(2): p. 59-189.
140. Ma, Y.J., et al., *Ordering of low-density Ge quantum dot on patterned Si substrate.* Journal of Physics D-Applied Physics, 2014. **47**(48).

141. Shchukin, V.A. and D. Bimberg, *Spontaneous ordering of nanostructures on crystal surfaces.* Reviews of Modern Physics, 1999. **71**(4): p. 1125-1171.
142. Ledentsov, N.N., et al., *Quantum dot heterostructures: fabrication, properties, lasers (Review).* Semiconductors, 1998. **32**(4): p. 343-365.
143. Davis, R.F., et al., *Thin-Film Deposition and Microelectronic and Optoelectronic Device Fabrication and Characterization in Monocrystalline Alpha and Beta Silicon-Carbide.* Proceedings of the Ieee, 1991. **79**(5): p. 677-701.
144. Kasper, E. and K. Lyutovich, *Strain adjustment with thin virtual substrates.* Solid-State Electronics, 2004. **48**(8): p. 1257-1263.
145. Pchelyakov, O.P., et al., *Surface processes and phase diagrams in MBE growth of Si/Ge heterostructure.* Thin Solid Films, 1997. **306**(2): p. 299-306.
146. Gouder, S., et al., *Investigation of microstructure and morphology for the Ge on porous silicon/Si substrate hetero-structure obtained by molecular beam epitaxy.* Thin Solid Films, 2014. **550**: p. 233-238.
147. Yoffe, A.D., *Semiconductor quantum dots and related systems: electronic, optical, luminescence and related properties of low dimensional systems.* Advances in Physics, 2001. **50**(1): p. 1-208.
148. Zhou, H., et al., *Evolution of Wurtzite ZnO Films on Cubic MgO (001) Substrates: A Structural, Optical, and Electronic Investigation of the Misfit Structures.* Acs Applied Materials & Interfaces, 2014. **6**(16): p. 13823-13832.
149. Forrest, S.R., *Ultrathin organic films grown by organic molecular beam deposition and related techniques.* Chemical Reviews, 1997. **97**(6): p. 1793-1896.
150. Levine, B.F., *Quantum-Well Infrared Photodetectors.* Journal of Applied Physics, 1993. **74**(8): p. R1-R81.
151. Nakamura, S., et al., *InGaN-based multi-quantum-well-structure laser diodes.* Japanese Journal of Applied Physics Part 2-Letters, 1996. **35**(1B): p. L74-L76.
152. Jain, S.C., et al., *III-nitrides: Growth, characterization, and properties.* Journal of Applied Physics, 2000. **87**(3): p. 965-1006.
153. Schubert, M.F., et al., *Polarization-matched GaInN/AlGaInN multi-quantum-well light-emitting diodes with reduced efficiency droop.* Applied Physics Letters, 2008. **93**(4).
154. Kong, Y.C., et al., *Ultraviolet-emitting ZnO nanowires synthesized by a physical vapor deposition approach.* Applied Physics Letters, 2001. **78**(4): p. 407-409.
155. Lauhon, L.J., et al., *Epitaxial core-shell and core-multishell nanowire heterostructures.* Nature, 2002. **420**(6911): p. 57-61.
156. Goldberger, J., et al., *Single-crystal gallium nitride nanotubes.* Nature, 2003. **422**(6932): p. 599-602.
157. Hu, Z.Z., et al., *Phase-field modeling of epitaxial growth: Applications to step trains and island dynamics.* Physica D-Nonlinear Phenomena, 2012. **241**(2): p. 77-94.
158. Caflisch, R.E., et al., *Island dynamics and the level set method for epitaxial growth.* Applied Mathematics Letters, 1999. **12**(4): p. 13-22.
159. Xu, C.J. and T. Tang, *Stability analysis of large time-stepping methods for epitaxial growth models.* Siam Journal on Numerical Analysis, 2006. **44**(4): p. 1759-1779.
160. Tu, Y.H. and J. Tersoff, *Coarsening, mixing, and motion: The complex evolution of epitaxial islands.* Physical Review Letters, 2007. **98**(9).

161. Geneste, G., et al., *Competing mechanisms in the atomic diffusion of a MgO admolecule on the MgO(001) surface.* Journal of Physics-Condensed Matter, 2009. **21**(31).
162. Antoshchenkova, E., et al., *Kinetic Monte-Carlo simulation of the homoepitaxial growth of MgO{001} thin films by molecular deposition.* Surface Science, 2012. **606**(5-6): p. 605-614.
163. Taioli, S., *Computational study of graphene growth on copper by first-principles and kinetic Monte Carlo calculations.* Journal of Molecular Modeling, 2014. **20**(7).
164. Biswas, R., G.S. Grest, and C.M. Soukoulis, *Molecular-Dynamics Simulation of Cluster and Atom Deposition on Silicon(111).* Physical Review B, 1988. **38**(12): p. 8154-8162.
165. Matsukuma, M. and S. Hamaguchi, *Molecular dynamics simulation of microcrystalline Si deposition processes by silane plasmas.* Thin Solid Films, 2008. **516**(11): p. 3443-3448.
166. Ratsch, C. and J.A. Venables, *Nucleation theory and the early stages of thin film growth.* Journal of Vacuum Science & Technology A, 2003. **21**(5): p. S96-S109.
167. Cox, E., et al., *Temperature dependence of island growth shapes during submonolayer deposition of Ag on Ag(111).* Physical Review B, 2005. **71**(11).
168. Moskovkin, P. and S. Lucas, *Computer simulations of the early-stage growth of Ge clusters at elevated temperatures on patterned Si substrate using the kinetic Monte Carlo method.* Thin Solid Films, 2013. **536**: p. 313-317.
169. Gonzalez-Gonzalez, A., C. Polop, and E. Vasco, *Postcoalescence Evolution of Growth Stress in Polycrystalline Films.* Physical Review Letters, 2013. **110**(5).
170. Eggleston, J.J. and P.W. Voorhees, *Ordered growth of nanocrystals via a morphological instability.* Applied Physics Letters, 2002. **80**(2): p. 306-308.
171. Niu, X., et al., *Level set simulation of directed self-assembly during epitaxial growth.* Physical Review B, 2006. **74**(19).
172. Papac, J., et al., *Island-dynamics model for mound formation: Effect of a step-edge barrier.* Physical Review E, 2014. **90**(2).
173. Tsalikis, D.G., et al., *A hybrid kinetic Monte Carlo method for simulating silicon films grown by plasma-enhanced chemical vapor deposition.* Journal of Chemical Physics, 2013. **139**(20).
174. Masin, M., et al., *Multiscale modeling of submonolayer growth for Fe/Mo (110).* European Physical Journal B, 2013. **86**(8).
175. Ng, T.Y., V. Pandurangan, and H. Li, *Multiscale modeling of nanoindentation in copper thin films via the concurrent coupling of the meshless Hermite-Cloud method with molecular dynamics.* Applied Surface Science, 2011. **257**(24): p. 10613-10620.
176. Zoontjens, P., T.P. Schulze, and S.C. Hendy, *Hybrid method for modeling epitaxial growth: Kinetic Monte Carlo plus molecular dynamics.* Physical Review B, 2007. **76**(24).
177. Kevrekidis, I.G., C.W. Gear, and G. Hummer, *Equation-free: The computer-aided analysis of comptex multiscale systems.* Aiche Journal, 2004. **50**(7): p. 1346-1355.
178. Kavousanakis, M.E., et al., *Projective and coarse projective integration for problems with continuous symmetries.* Journal of Computational Physics, 2007. **225**(1): p. 382-407.

179. Wagner, G.J., X.W. Zhou, and S.J. Plimpton, *Equation-Free Accelerated Simulations of the Morphological Relaxation of Crystal Surfaces.* International Journal for Multiscale Computational Engineering, 2010. **8**(4): p. 423-439.
180. Matthew, O.W., J.L. Proctor, and J.N. Kutz, *Modeling disease transmission near eradication: An equation free approach.* Physica D-Nonlinear Phenomena, 2015. **290**: p. 44-56.
181. Papavasiliou, A. and I.G. Kevrekidis, *Variance reduction for the equation-free simulation of multiscale stochastic systems.* Multiscale Modeling & Simulation, 2007. **6**(1): p. 70-89.
182. Givon, D. and I.G. Kevrekidis, *Multiscale Integration Schemes for Jump-Diffusion Systems.* Multiscale Modeling & Simulation, 2008. **7**(2): p. 495-516.
183. Varshney, A. and A. Armaou, *Identification of macroscopic variables for low-order modeling of thin-film growth.* Industrial & Engineering Chemistry Research, 2006. **45**(25): p. 8290-8298.
184. Stillinger, F.H., *Rigorous Basis of Frenkel-Band Theory of Association Equilibrium.* Journal of Chemical Physics, 1963. **38**(7): p. 1486-&.
185. Tan, T.Y., H. Foll, and W. Krakow, *Detection of Extended Interstitial Chains in Ion-Damaged Silicon.* Applied Physics Letters, 1980. **37**(12): p. 1102-1104.
186. Jones, K.S., S. Prussin, and E.R. Weber, *A Systematic Analysis of Defects in Ion-Implanted Silicon.* Applied Physics a-Materials Science & Processing, 1988. **45**(1): p. 1-34.
187. Claverie, A., et al., *On the Relation between Dopant Anomalous Diffusion in Si and End-of-Range Defects.* Nuclear Instruments & Methods in Physics Research Section B-Beam Interactions with Materials and Atoms, 1995. **96**(1-2): p. 202-209.
188. Stolk, P.A., et al., *Physical mechanisms of transient enhanced dopant diffusion in ion-implanted silicon.* Journal of Applied Physics, 1997. **81**(9): p. 6031-6050.
189. Jones, K.S., et al., *Studies of the interactions between (311) defects and type I and II dislocation loops in Si+ implanted silicon.* Nuclear Instruments & Methods in Physics Research Section B-Beam Interactions with Materials and Atoms, 1995. **106**(1-4): p. 227-232.
190. Cowern, N.E.B., H.F.F. Jos, and K.T.F. Janssen, *Role of Point-Defects in the Transient Diffusion and Clustering of Implanted Boron in Silicon.* Materials Science and Engineering B-Solid State Materials for Advanced Technology, 1989. **4**(1-4): p. 101-105.
191. Eaglesham, D.J., et al., *Implantation and Transient B-Diffusion in Si - the Source of the Interstitials.* Applied Physics Letters, 1994. **65**(18): p. 2305-2307.
192. Colombeau, B., et al., *Atomistic simulations of extrinsic defects evolution and transient enhanced diffusion in silicon.* Applied Physics Letters, 2001. **78**(7): p. 940-942.
193. Zhang, L.H., et al., *Transient Enhanced Diffusion without (311)-Defects in Low-Energy B+-Implanted Silicon.* Applied Physics Letters, 1995. **67**(14): p. 2025-2027.
194. Caturla, M.J., M.D. Johnson, and T.D. de la Rubia, *The fraction of substitutional boron in silicon during ion implantation and thermal annealing.* Applied Physics Letters, 1998. **72**(21): p. 2736-2738.

195. Sinno, T. and R.A. Brown, *Modeling microdefect formation in Czochralski silicon.* Journal of the Electrochemical Society, 1999. **146**(6): p. 2300-2312.
196. Frewen, T.A. and T. Sinno, *Vacancy self-trapping during rapid thermal annealing of silicon wafers.* Applied Physics Letters, 2006. **89**(19): p. 191903.
197. Voronkov, V.V. and R. Falster, *Vacancy-type microdefect formation in Czochralski silicon.* Journal of Crystal Growth, 1998. **194**(1): p. 76-88.
198. Nakamura, K., Saishoji, T., Tomioka, J., Katayama, T. *The Dissolution Behavior of the Void Defects by Hydrogen Annealing in Czochralski-Grown Silicon Crystal s*. in *Proceedings of the Third International Symposium on Defects In Silicon*. 1999. The Electreochemical Society.
199. Sueoka, K., N. Ikeda, and T. Yamamoto, *Morphology and Size Distribution of Oxide Precipitates in as-Grown Czochralski Silicon-Crystals.* Applied Physics Letters, 1994. **65**(13): p. 1686-1688.
200. Sueoka, K., et al., *Computer simulation for morphology, size, and density of oxide precipitates in CZ silicon.* Journal of the Electrochemical Society, 2003. **150**(8): p. G469-G475.
201. Voronkov, V.V. and R. Falster, *Effect of vacancies on nucleation of oxide precipitates in silicon.* Materials Science in Semiconductor Processing, 2002. **5**(4-5): p. 387-390.
202. Akatsuka, M., et al., *Effect of rapid thermal annealing on oxygen precipitation behavior in silicon wafers.* Japanese Journal of Applied Physics Part 1-Regular Papers Short Notes & Review Papers, 2001. **40**(5A): p. 3055-3062.
203. Vanhellemont, J., O. De Gryse, and P. Clauws, *Critical precipitate size revisited and implications for oxygen precipitation in silicon.* Applied Physics Letters, 2005. **86**(22): p. -.
204. Kapur, S.S., et al., *Role of configurational entropy in the thermodynamics of clusters of point defects in crystalline solids.* Physical Review B, 2005. **72**(1): p. -.
205. Itsumi, M., et al., *The Composition of Octahedron Structures That Act as an Origin of Defects in Thermal Sio2 on Czochralski Silicon.* Journal of Applied Physics, 1995. **78**(10): p. 5984-5988.
206. Prasad, M. and T. Sinno, *Atomistic-to-continuum description of vacancy cluster properties in crystalline silicon.* Applied Physics Letters, 2002. **80**(11): p. 1951-1953.
207. Pan, G.Z. and K.N. Tu, *Transmission electron microscopy on {113} rodlike defects and {111} dislocation loops in silicon-implanted silicon.* Journal of Applied Physics, 1997. **82**(2): p. 601-608.
208. Pan, G.Z., K.N. Tu, and A. Prussin, *Size-distribution and annealing behavior of end-of-range dislocation loops in silicon-implanted silicon.* Journal of Applied Physics, 1997. **81**(1): p. 78-84.
209. Pan, G.Z., K.N. Tu, and S. Prussin, *Microstructural evolution of {113} rodlike defects and {111} dislocation loops in silicon-implanted silicon.* Applied Physics Letters, 1997. **71**(5): p. 659-661.
210. Liu, J., M.E. Law, and K.S. Jones, *Evolution of Dislocation Loops in Silicon in an Inert Ambient .1.* Solid-State Electronics, 1995. **38**(7): p. 1305-1312.
211. Liu, J., et al., *The effect of boron implant energy on transient enhanced diffusion in silicon.* Journal of Applied Physics, 1997. **81**(4): p. 1656-1660.

212. Haynes, T.E., et al., *Interactions of ion-implantation-induced interstitials with boron at high concentrations in silicon.* Applied Physics Letters, 1996. **69**(10): p. 1376-1378.
213. Claverie, A., et al., *Nucleation, growth and dissolution of extended defects in implanted Si: impact on dopant diffusion.* Nuclear Instruments & Methods in Physics Research Section B-Beam Interactions with Materials and Atoms, 1999. **147**(1-4): p. 1-12.
214. Claverie, A., et al., *Modeling of the Ostwald ripening of extrinsic defects and transient enhanced diffusion in silicon.* Nuclear Instruments & Methods in Physics Research Section B-Beam Interactions with Materials and Atoms, 2002. **186**: p. 281-286.
215. Claverie, A., et al., *Extended defects in shallow implants.* Applied Physics a-Materials Science & Processing, 2003. **76**(7): p. 1025-1033.
216. Kapur, S.S. and T. Sinno, *Detailed microscopic analysis of self-interstitial aggregation in silicon. I. Direct molecular dynamics simulations of aggregation.* Physical Review B, 2010. **82**(4): p. -.
217. Kapur, S.S., A.M. Nieves, and T. Sinno, *Detailed microscopic analysis of self-interstitial aggregation in silicon. II. Thermodynamic analysis of single clusters.* Physical Review B, 2010. **82**(4): p. -.
218. Cristiano, F., et al., *Ion beam induced defects in crystalline silicon.* Nuclear Instruments & Methods in Physics Research Section B-Beam Interactions with Materials and Atoms, 2004. **216**: p. 46-56.
219. Kapur, S.S., A.M. Nieves, and T. Sinno, *Detailed microscopic analysis of self-interstitial aggregation in silicon. II. Thermodynamic analysis of single clusters.* Physical Review B, 2010. **82**(4).
220. Chou, C.T., et al., *{111} defects in 1-MeV-silicon-ion-implanted silicon.* Physical Review B, 1995. **52**(24): p. 17223-17230.
221. Fedina, L., et al., *On the mechanism of {111}-defect formation in silicon studied by in situ electron irradiation in a high resolution electron microscope.* Philosophical Magazine a-Physics of Condensed Matter Structure Defects and Mechanical Properties, 1998. **77**(2): p. 423-435.
222. Fedina, L., et al., *Extended defects formation in Si crystals by clustering of intrinsic point defects studied by in-situ electron irradiation in an HREM.* Physica Status Solidi a-Applied Research, 1999. **171**(1): p. 147-157.
223. Goss, J.P., et al., *Planar interstitial aggregates in Si.* Journal of Physics-Condensed Matter, 2002. **14**(48): p. 12843-12853.
224. Boninelli, S., et al., *Evidences of an intermediate rodlike defect during the transformation of {113} defects into dislocation loops.* Applied Physics Letters, 2006. **89**(16): p. 161904.
225. Boninelli, S., et al., *Transformation of {113} defects into dislocation loops mediated by the {111} rod-like defects.* Nuclear Instruments & Methods in Physics Research Section B-Beam Interactions with Materials and Atoms, 2006. **253**(1-2): p. 80-84.
226. Takeda, S., *An Atomic Model of Electron-Irradiation-Induced Defects on (113) in Si.* Japanese Journal of Applied Physics Part 2-Letters, 1991. **30**(4A): p. L639-L642.

227. Kohyama, M. and S. Takeda, *Atomic-Structure and Energy of the (113) Planar Interstitial Defects in Si.* Physical Review B, 1992. **46**(19): p. 12305-12315.
228. Kim, J., et al., *Stability of Si-interstitial defects: From point to extended defects.* Physical Review Letters, 2000. **84**(3): p. 503-506.
229. Lee, S. and G.S. Hwang, *Structure and stability of small compact self-interstitial clusters in crystalline silicon.* Physical Review B, 2008. **77**(8): p. 085210.
230. Kapur, S.S. and T. Sinno, *Entropic origins of stability in silicon interstitial clusters.* Applied Physics Letters, 2008. **93**(22): p. 221911.
231. Cowern, N.E.B., et al., *Energetics of self-interstitial clusters in Si.* Physical Review Letters, 1999. **82**(22): p. 4460-4463.
232. De Kock, A. and W. Van de Wijgert, *The effect of doping on the formation of swirl defects in dislocation-free czochralski-grown silicon crystals.* Journal of Crystal Growth, 1980. **49**(4): p. 718-734.
233. Nieves, A.M. and T. Sinno, *An enthalpy landscape view of homogeneous melting in crystals.* Journal of Chemical Physics, 2011. **135**(7).
234. Nieves, A.M., C.Y. Chuang, and T. Sinno, *Inherent structure analysis of defect thermodynamics and melting in silicon.* Molecular Simulation, 2012. **38**(8-9): p. 659-670.
235. Stillinger, F.H. and T.A. Weber, *Point-Defects in Bcc Crystals - Structures, Transition Kinetics, and Melting Implications.* Journal of Chemical Physics, 1984. **81**(11): p. 5095-5103.
236. Bogdan, T.V., D.J. Wales, and F. Calvo, *Equilibrium thermodynamics from basin-sampling.* Journal of Chemical Physics, 2006. **124**(4): p. -.
237. Calvo, F., J.P.K. Doye, and D.J. Wales, *Collapse of Lennard-Jones homopolymers: Size effects and energy landscapes.* Journal of Chemical Physics, 2002. **116**(6): p. 2642-2649.
238. Farrell, J.D., et al., *Energy landscapes, structural topologies and rearrangement mechanisms in clusters of dipolar particles.* Soft Matter, 2013. **9**(22): p. 5407-5416.
239. Sciortino, F., W. Kob, and P. Tartaglia, *Inherent structure entropy of supercooled liquids.* Physical Review Letters, 1999. **83**(16): p. 3214-3217.
240. Debenedetti, P.G. and F.H. Stillinger, *Supercooled liquids and the glass transition.* Nature, 2001. **410**(6825): p. 259-267.
241. Buchner, S. and A. Heuer, *Potential energy landscape of a model glass former: Thermodynamics, anharmonicities, and finite size effects.* Physical Review E, 1999. **60**(6): p. 6507-6518.
242. Nakagawa, N. and M. Peyrard, *The inherent structure landscape of a protein.* Proceedings of the National Academy of Sciences of the United States of America, 2006. **103**(14): p. 5279-5284.
243. Stillinger, F.H. and T.A. Weber, *Hidden Structure in Liquids.* Physical Review A, 1982. **25**(2): p. 978-989.
244. Wales, D.J., *The energy landscape as a unifying theme in molecular science.* Philosophical Transactions of the Royal Society of London Series a-Mathematical Physical and Engineering Sciences, 2005. **363**(1827): p. 357-375.
245. Sugita, Y. and Y. Okamoto, *Replica-exchange molecular dynamics method for protein folding.* Chemical Physics Letters, 1999. **314**(1): p. 141-151.

246. Richie, D.A., et al., *Complexity of small silicon self-interstitial defects.* Physical Review Letters, 2004. **92**(4): p. -.